
Unterschrift



DIPLOMARBEIT

Light Yield and Quenching Factor Simulations based on Birks' Law for a CRESST-like CaWO_4 Crystal

ausgeführt am

Institut für Hochenergiephysik
der Österreichischen Akademie der Wissenschaften

Institute for High Energy Physics
of the Austrian Academy of Sciences

unter der Anleitung von

Univ. Ass. Dipl.-Phys. Dr. Holger Kluck,
Univ. Prof. Dipl.-Phys. Dr. Jochen Schieck

durch

Alexander Fuß, BSc

Saarplatz 19/1/3

A-1190 Wien

alexander.fuss@gmx.at

Contents

1. Introduction	5
2. Dark Matter	7
2.1. Indications of Dark Matter	7
2.2. Standard Cosmology - Λ CDM Model	9
2.3. Cold Dark Matter Particle Candidates	10
2.4. Direct Dark Matter Detection	12
3. CRESST Experiment	15
3.1. Detector Modules – Two-Channel Detection	15
3.2. Scintillation Light Production in CaWO_4	16
3.2.1. Microscopic Model	16
3.2.2. Birks' Model	18
3.2.3. Scintillation Light Quenching	19
4. Energy Loss Processes of Particles traversing CaWO_4	23
4.1. Types of Energy Loss Processes	23
4.2. Energy Loss of different Particles	24
4.2.1. Electrons	25
4.2.2. Gammas	26
4.2.3. Ions	26
5. Simulation and Analysis Technique	31
5.1. Overview of the Methodology	31
5.2. Geometry and Particles used in the Simulations	32
5.3. Particle Cascade identification and allocation	33
5.4. Light Yield Computation	35
5.5. Normalization to 122 keV Gamma Events	35
5.6. Quenching Factor Calculation	36
6. Reference Values for our simulated Results	37
6.1. Birks' parameters	37
6.2. Quenching Factor Data	39

7. Simulation Models and Results	43
7.1. Baseline Physics Implementation in Geant4	43
7.2. Gamma Calibration Simulation	47
7.3. Standard Geant4 Settings	49
7.4. Standard Geant4 with Step Limitation	55
7.5. SRIM Stopping Powers and Step Limit	59
7.6. G4ScreenedNuclearRecoil Class	64
7.7. Modification of G4ScreenedNuclearRecoil	68
7.8. Effect of Energy Loss Fluctuations	72
8. Summary and Conclusion	81
A. Simulation and Analysis Software and Scripts	83
A.1. Geant4	83
A.1.1. UI/Macro Files	84
A.1.2. Stepping Performance	85
A.2. Root	86
A.2.1. Root Analysis Script	87
B. New and Adapted Geant4 Classes	99
C. Brief Analysis of Coherent Photon Scattering in CaWO_4	105
Bibliography	109

Chapter 1.

Introduction

More than 80 years ago, observations of galaxy clusters for the first time showed, that the gravitational force on large scales is much higher than the amount of visible matter could account for. According to our standard cosmological model, a form of non-luminous matter, called dark matter, therefore has to make up more than 80% of all the matter in the universe. Among various theories trying to explain this phenomenon, not-yet observed cold dark matter particles are most prominent. Many experiments have been searching for such a particle. However, up to now, none of the candidates and theories could be brought to proof. Hence, the nature of dark matter still remains one of the major unsolved issues in modern cosmology and particle physics.

Direct searches for dark matter are based on attempting to observe scattering of a dark matter particle off a nucleus in the detector. This process has a very low cross section compared to the various background events in the same energy region. Thus, a shielding that minimizes the background as well as a precise knowledge and understanding of the residual background are needed.

The CRESST (Cryogenic Rare Event Search with Superconducting Thermometers) experiment is one of these direct detection experiments, having a leading role in the search for low-mass dark matter. In the underground laboratory in Gran Sasso, CaWO_4 detectors are operated with a two-channel read-out, detecting the phonon signal (energy deposited in the target crystal) as well as the light signal (scintillation photons created as a result of the energy deposition). The relation between the light and phonon signal is called 'light yield' (LY). This quantity alters for different particles hitting the crystal, being indirectly proportional to the ionization strength of the particle. A further quantity called 'quenching factor' (QF) is attained by normalizing the LY of a certain particle to the one of γ -particles depositing the same amount of energy in the crystal. QFs are characteristic for a certain crystal and can be used to distinguish between different detected particles. The precise identification of nuclear recoils is crucial for the possibility of detecting dark matter. So far, the parametrization of the respective QFs is done via a completely empirical fit using 9 free parameters.

Within this thesis, however, a semi-empirical approach is tested, which could reduce the amount of free parameters to 2 in the ideal case. For this purpose, a simulation framework accompanying the experiment, based on the Monte Carlo (MC) code Geant4, is used. This framework enables a comparison of experimental results to simulations and can lead to a better understanding of the experimentally observed data.

The model developed in this work for describing the QFs is based on Birks' law with its two parameters A and kB . If good precision is attained, these two parameters alone could be sufficient to not only describe but also predict QFs of different particles for any detector module, solely based on calibration data obtained with γ -sources. In the course of this work, we therefore made adaptations to the simulation code and compared different ion stopping power data (ICRU and SRIM) and simulation classes responsible for the particles' energy loss processes.

Chapter 2.

Dark Matter

Dark matter is a form of non-luminous matter, which we can, as of today, only observe indirectly through its gravitational effects on surrounding matter. For this reason, there are many unknown parameters, keeping the door open for a lot of different theories trying to describe the observed effects. Some of them state, that there is not even a need for a new particle, but that the laws of gravitation could be modulated. These theories are grouped under various headings like 'MOND' (Modified Newtonian Dynamics) or 'emergent gravity'. The most generally agreed models, however, leave us with non-baryonic, non-luminous particle dark matter that only interacts very weakly with standard model particles.

2.1. Indications of Dark Matter

The nature of dark matter is yet to be found in an experiment. As of today, we do not know which mass a dark matter particle might have and we do not even hold direct observational evidence for the existence of a dark matter particle. However, there are various effects that let us indirectly observe dark matter, which are listed in the following:

Galaxies in galaxy clusters - The velocity of galaxies in the cluster is higher than would be allowed to hold the cluster together, if the gravitational force only arose from the amount of luminous matter. This was first observed by Fritz Zwicky in the 1930s [1], who postulated an invisible form of matter accounting for the missing gravitational force.

Spiral galaxies - The argument in this case is very similar to the one concerning galaxies in galaxy clusters. Stars in spiral galaxies rotate with approximately the same velocity, independent of their distance to the galactic center (first measurements by Vera Rubin in the late 1960s [2]) while the distribution would be expected to follow $v(r) \propto 1/\sqrt{r}$ if only visible matter would be present.

Gravitational lensing - Light coming from distant galaxies is bent by galaxy clusters along its path. Observing this effect makes it possible to deduce the amount of mass in the clusters [3]. A very neat example of indirect evidence for dark matter comes from the gravitational lensing studies of the Bullet Cluster, which is composed of two clusters that have once collided. As dark matter does only interact very weakly, it is not slowed down substantially whereas the ordinary matter is. Weak gravitational lensing showed that a lot of mass is situated outside the center of the visible system, which yields that through the collision, dark matter and normal matter have been separated [4].

Cosmic microwave background (CMB) - Anisotropies in the CMB spectrum can be described with a power spectrum. The different peaks in this spectrum indicate the effects of normal and dark matter. The WMAP [5] and Planck [6] Collaborations constrain the different contributions to the total energy density of the universe based on the Standard Cosmological Model (cf. section 2.2) and the Friedmann equations. The percentage of dark matter is approximately five times larger than the percentage of ordinary matter.

Structure formation - A bottom up model for structure formation in our universe needs non-baryonic cold dark matter that has decoupled from the baryon-photon-plasma much earlier than the baryonic matter has decoupled from the photons. Otherwise, for example with velocities of hot dark matter, the large-scale structure of the universe could not be explained [7].

Candidate Theories

The distinct observations give various hints about certain properties and the amount of dark matter in the universe. However, a lot of theories have been developed, all trying to describe the observed effects with different approaches. The possible candidates for the composition of dark matter are listed in the following:

- One of the early theories proposed that dark matter may consist of heavy, non-luminous ordinary matter objects, such as black holes, neutron stars or brown dwarfs. Together, these candidate objects are known as MACHOs (Massive Compact Halo Objects). However, this theory has been excluded, because the contribution of the observed amount of MACHOs to dark matter could only be very small [8, 9].
- A further approach states that we might not even need an additional particle or additional mass but rather a modification of the laws of gravitation. The first model in this context was the so called MOND (Modified Newtonian Dynamics) [10]. Many different ever more complex models followed, as the initial one had to be extended to adapt to all observations. Especially, it

still has problems describing galaxy clusters. Thus, today, the community believing in this theory is rather weak.

- The last and very likely most important model, that is mentioned here, is describing dark matter through non-baryonic, non-standard model particles [11–14]. These could be hot, warm or cold dark matter particles referring to their velocity. As stated in the list of indications for dark matter, however, structure formation of galaxies and galaxy clusters yields cold dark matter - meaning that its particles move slowly with respect to the speed of light - as the most suitable candidate.

In this thesis as well as in the CRESST direct dark matter search, we focus on cold dark matter, the most widely accepted theory, being part of the standard model of cosmology.

2.2. Standard Cosmology - Λ CDM Model

The Λ CDM Model is the standard model of cosmology, as it is well in conformity with the main properties of our universe. It explains the observed cosmic microwave background (CMB), the accelerated expansion of the universe and various other observations like the abundances of elements and large-scale structures in the distribution of galaxies.

This model describes a universe that contains a cosmological constant (Λ) and cold dark matter (CDM) and is based on the cosmological principle, i.e. the large-scale isotropy and homogeneity of our universe, which in other words means that on large enough scale our universe looks the same no matter where you are and in which direction you point. The model includes a "Big Bang", implying that the universe originated from an initial singularity from which space-time started expanding followed by an inflationary phase. The evolution of the universe is described via the Friedmann equations

$$H^2 = \left(\frac{\dot{a}}{a}\right)^2 = \frac{8\pi G}{3}\rho - \frac{k}{a^2} + \frac{\Lambda}{3} \quad , \quad (2.1)$$

$$\frac{\ddot{a}}{a} = \frac{\Lambda}{3} - \frac{4\pi G}{3}(\rho + 3p) \quad , \quad (2.2)$$

which are derived from Einstein's field equations of gravitation using the Friedmann-Lemaître-Robertson-Walker metric. H is the Hubble parameter, a the scale factor, G the gravitational constant, ρ the mass density, k the spatial curvature and Λ the cosmological constant which is the driving force for the accelerated expansion of the universe.

The spatial curvature is set to zero as our universe is (at least to a good approximation) flat. Furthermore, the critical density ρ_c is defined by setting Λ to zero,

$$\rho_c = \frac{3H^2}{8\pi G} \quad . \quad (2.3)$$

The normalized energy density,

$$\Omega = \sum_i \Omega_i = \sum_i \frac{\rho_i}{\rho_c} \quad , \quad (2.4)$$

yields the composition of the universe. Every part - i.e. matter, dark energy and radiation - contributes a certain fraction correspondent to its abundance. Results of the Planck Collaboration from 2015 [6] give the latest numbers for all the cosmological parameters including Ω_i . The contribution of dark energy to the normalized energy density $\Omega = 1$ is determined to be $\Omega_\Lambda = 0.6911 \pm 0.0062$, while the contribution of matter is $\Omega_m = 0.3089 \pm 0.0062$. Only a rather short fraction of the this last number seems to be in the form of ordinary matter, which means matter that we can observe. The Planck data give us numbers for $\Omega_m h^2 = 0.14170 \pm 0.00097$ and $\Omega_b h^2 = 0.02230 \pm 0.00014$, where m denotes the total matter and b the baryonic matter. The parameter h is the reduced Hubble constant related to the Hubble constant H_0 by $H_0 = 100 h$ (km/s)/Mpc. With the numbers for $\Omega_m h^2$ and $\Omega_b h^2$ we can calculate the fraction of baryonic matter to be approximately $\Omega_b \approx 0.0486$ and the fraction of dark matter to be $\Omega_{CDM} \approx 0.2603$ respectively. Compared to the energy densities of matter and dark energy, the contribution due to radiation, $\Omega_r h^2 \approx 2.47 \times 10^{-5}$, is very small. The same is true for neutrinos. Taking into account the upper limits on neutrino masses, their energy density can be constrained to $\Omega_\nu h^2 < 0.0025$.

To conclude, the model tells us how much dark matter compared to ordinary matter is present in our universe, describes the evolution of the universe from end of inflation up to now very well and predicts the future via (2.1) and (2.2). However, in first approximation, it does not depend on the exact nature of dark matter.

2.3. Cold Dark Matter Particle Candidates

The previous sections gave information about properties that dark matter particles have to entail. As a consequence, some models can be excluded, e.g. baryonic dark matter like MACHOs mentioned in section 2.1. Also a non-baryonic standard model candidate, the neutrino, can be ruled out. It would act as hot dark matter which could not explain structure formation in the early universe. Furthermore, the upper limit for the neutrino contribution to the normalized energy density is too small.

However, there are still different particles that might satisfy the claims. The cold dark matter candidates, shown in Fig. 2.1, are the following:

- The **axion** is a light pseudo-Nambu-Goldstone boson that was introduced by Peccei and Quinn to solve the strong CP problem and was found to have attributes that leave it as a viable dark matter candidate [15–17].
- Supersymmetry (SUSY) is the only non-trivial extension of the standard model (SM). Each fermion/boson of the SM would have a boson/fermion SUSY partner. A new form of parity is introduced, the so-called R-parity, which prevents the proton decay and at the same time ensures the stability of the lightest supersymmetric particle (LSP). This LSP, the lightest **neutralino** (often a superposition of bino, photino and higgsino, the SUSY partners of the SM gauge bosons) acts as a dark matter candidate. Even more candidates are allowed with the introduction of the SUSY model, namely the **gravitino** (SUSY partner of the graviton) and the **axino** (SUSY partner of the axion).
- **WIMPs** (Weakly Interacting Massive Particles) are hypothetical particles only interacting via the gravitational and the weak or an even weaker force. They are non-relativistic because of their mass and are - generally speaking - the leading candidates for (cold) dark matter. The theory predicts particles with a self-annihilation cross section that can lead to the obtained abundance of dark matter. Furthermore, it is in accordance with SUSY, as the neutralino would possess the demanded properties (see Fig. 2.1), but it may also be realized in other theories like universal extra dimensions.

As of today, WIMPs are the most popular dark matter candidate. If they are existent and make up the obtained amount of dark matter, every square centimeter on Earth is traversed by many of them each second. However, due to their weak interaction it is a difficult task to detect them and there are a number of different experiments currently trying to attest their existence. Essentially three types of experiments can be distinguished, namely production, indirect detection and direct detection.

With the method of indirect detection, one searches for the decay or annihilation products of dark matter particles. An alternative method is the production of WIMPs in collider experiments and detection through missing mass and momentum (provided that all other particles are detected). Direct detection, on the other hand, aims for the observation of nuclear recoils due to dark matter particles.

Within this project, we are focusing on the physics of direct dark matter detection.

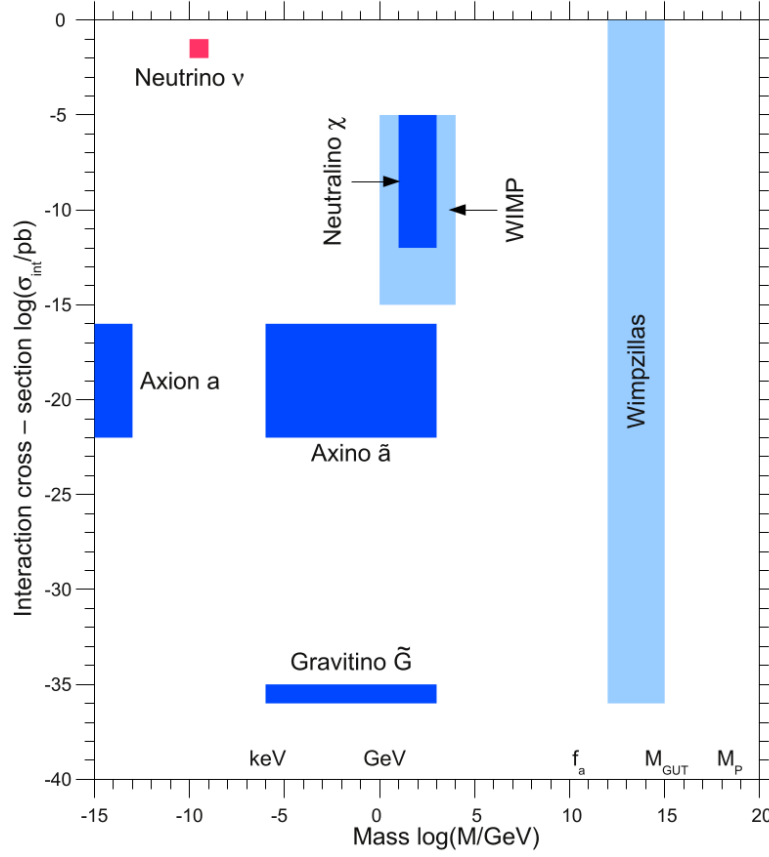


Figure 2.1.: Predicted masses and interaction cross sections of viable cold dark matter candidates. The neutrino is only shown for comparison.

Figure taken from [18].

2.4. Direct Dark Matter Detection

Direct detection of dark matter studies scattering of WIMPs (or other hypothetical dark matter particles) off atomic nuclei, usually in a detector located in an underground laboratory. The assumed velocity of WIMPs in the galactic halo leads to elastic scattering off the nuclei with expected nuclear recoil energies of a few keV up to a few tens of keV. In this energy region a lot of background events, e.g. caused by radioactivity, are present. A signal-background discrimination technique with high precision is required and radioactive contaminations have to be minimized. With techniques employed by modern experiments, signals due to electrons, γ -particles, α -particles and protons can be distinguished from neutron induced nuclear recoils. This can reduce the background significantly. Still, a remaining background due to the neutron induced events is present in the region of interest (ROI) for low-mass dark matter recoils of up to a few tens of keV.

Having a look back at Fig. 2.1, we see that the expected cross section of WIMPs is very low, going hand in hand with a low interaction rate. Thus, we expect an extremely small number of signals induced by WIMPs compared to those caused by other particles. Even with good shielding and discrimination methods the background is still dangerous and therefore has to be investigated thoroughly.

Among the many different experiments searching for dark matter directly, there are, for example, LUX, ZEPLIN and XENON using liquid xenon (LXe) detectors, CoGeNT, CDMS and EDELWEISS using cryogenic Ge detectors, DAMA/LIBRA and KIMS using solid scintillator targets (NaI(Tl) and CsI, respectively), and CRESST, combining the cryogenic and scintillator technique with the help of CaWO_4 detectors. All of these experiments are contributing their results to the search for a WIMP or an alternative dark matter particle and determine limits for the possible mass and cross section thereof. An example of an exclusion plot¹, combining the results of different collaborations, can be seen in Fig. 2.2. From looking at the different exclusion lines in the graph, it is obvious that CRESST has a leading role in setting the limits for low-mass dark matter.

¹ Exclusion plots with the latest experimental data (with cuts on spin-dependent or spin-independent interactions) can be generated at <http://dmttools.berkeley.edu/limitplots/>.

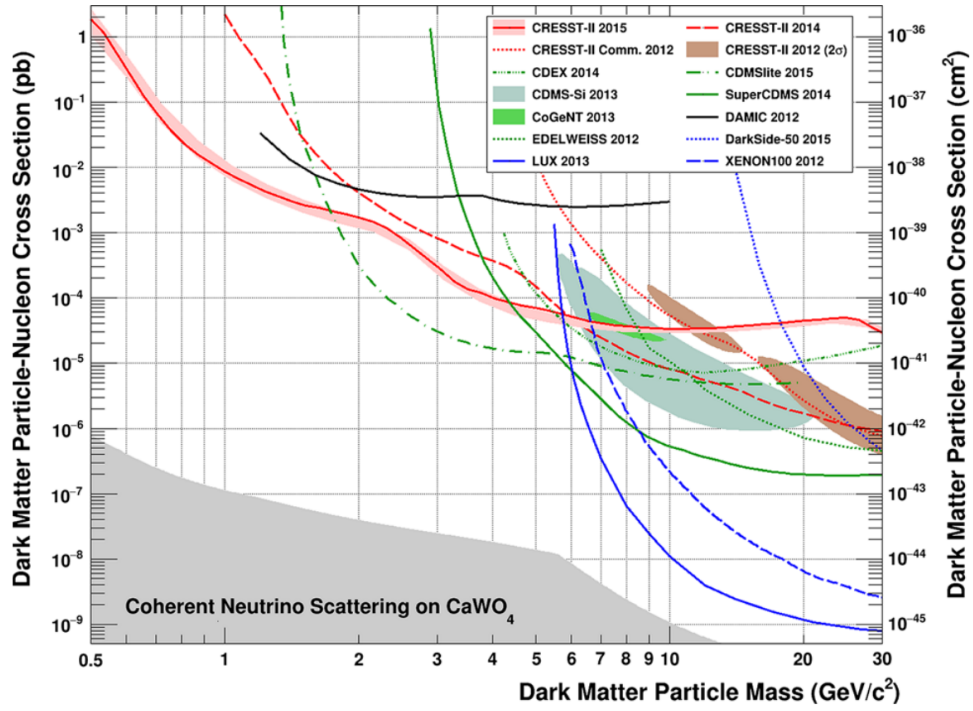


Figure 2.2.: Limits on elastic spin-independent dark matter-nucleon scattering are given. The solid red line shows the 'Lise' limit of the CRESST collaboration, setting the best limit in the very low energetic region ($\lesssim 1.7 \text{ GeV}/c^2$). Figure taken from Ref. [19].

Chapter 3.

CRESST Experiment

CRESST (Cryogenic Rare Event Search with Superconducting Thermometers) is an experiment searching for WIMP or even lower-mass dark matter with a direct detection method [19–21]. It is located at the Laboratori Nazionali del Gran Sasso (LNGS) in Italy, on average 1400 meters underground to shield the setup against cosmic radiation. This together with multiple passive shielding layers minimizes the background. Studies of the residual background, which is still expected to far exceed the possible signal due to dark matter, are highly important [22]. The detection system consists of a multi-element detector with modules composed of scintillating CaWO_4 crystals at a working temperature of ~ 15 mK. Particles scattering off a nucleon produce heat in the form of phonons and in the further course scintillation light. Two independent cryogenic calorimeters are operated to detect the phonon and the light signal.

3.1. Detector Modules – Two-Channel Detection

In the CRESST experiment, cryogenic detector modules are operated at a temperature of ~ 15 mK. Continuous cooling of the cryostat to this low temperature is provided by a dilution refrigerator. The detector modules each consist of a scintillating CaWO_4 crystal, in the following referred to as the phonon detector, and a separate light detector. In the latter, the scintillation-light photons are absorbed by a silicon on sapphire disk and also converted into phonons. Hence, both of the detectors can be read out with a transition edge sensor (TES) equipped to them. The TES is an evaporated film of Tungsten and operated at the transition temperature between superconducting and normal conducting phase. A phonon leads to an increase of the TES temperature, and thus to a higher resistance of the TES. The resistance is read out with the help of a SQUID (Superconducting Quantum Interference Device), which is sensitive to very small changes of the current through the TES and can hence provide a reliable detection of particles hitting the detector.

The phonon detector measures the energy E_{dep} deposited in the crystal due to an

incident particle. This measure cannot discriminate between different interacting particles. However, the amount of scintillation light produced and therefore the energy L measured in the light detector depends strongly on the type of particle. Higher ionizing particles lead to a reduced light signal. Thus, it can be distinguished between events due to e^-/γ -particles, α -particles, and nuclear recoils of Oxygen, Calcium and Tungsten induced by neutrons or hypothetical dark matter particles.

3.2. Scintillation Light Production in CaWO_4

In this section, the generation of scintillation light in a CaWO_4 single crystal is described on the basis of a microscopic model [23], that explains the formation of fundamental excitations and their possible radiative and non-radiative recombination processes. Furthermore, a macroscopic model (Birks' model) is discussed, which uses a phenomenological formula to describe the scintillation light production.

3.2.1. Microscopic Model

In the unexcited state, the electron configuration of a CaWO_4 single crystal consists of a filled valence band and an empty conduction band, separated by a band gap energy of roughly 5 eV. A particle traversing the detector and depositing energy, excites electrons along its track and along the track of the secondary particles. Such interactions lead to the excitation of an electron to the conduction band, leaving a hole in the valence band. At the position of a $[\text{WO}_4^*]^{2-}$ complex, the hole relaxes to the band edge, where it is preferably located at, leading to a Jahn-Teller distortion. This distortion creates an energy level within the band gap, shifted by the Jahn-Teller energy (≈ 0.63 eV) from the top of the valence band, yielding the formation of a so-called self-trapped hole (STH).

A potential well is hence present located at the position of the $[\text{WO}_4^*]^{2-}$ complex for an electron in the conduction band. The transition to the ground state is spin-forbidden for an electron at the band edge. However, due to the potential well, the electron can further relax from the band edge down to a state in the band gap and form a self-trapped exciton (STE). A sketch of the whole process of STE formation is shown in Fig. 3.1.

Different types of recombination processes can be considered for the de-excitation to the ground state, namely radiative decay, non-radiative decay, STE-STE interaction and migration to neighboring defect centers. However, at mK temperatures (working temperature of CRESST detectors), only STE-STE interaction and radiative decay are possible [23]. The STE-STE interaction, which is also referred to as

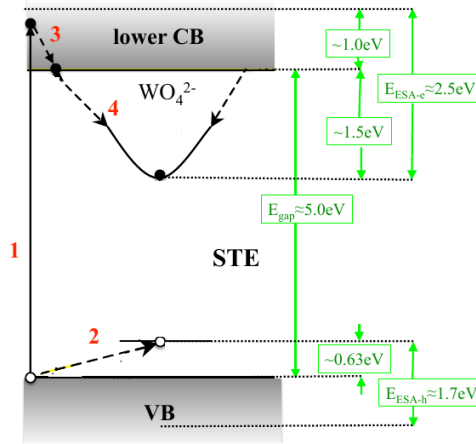


Figure 3.1.: Depiction of the formation process of self-trapped excitons (STEs). The electronic structure of a CaWO_4 crystal is indicated, with 'VB' being the valence band and 'lower CB' the lower conduction band. Red numbers 1-4 represent the steps of the STE formation: 1) Excitation of an electron from the VB to the lower CB. 2) Formation of a self-trapped hole (STH). 3) Relaxation of the excited electron to the band edge. 4) Trapping of the electron into the potential well, forming an STE. Figure taken from Ref. [23, 24].

Förster interaction, is a non-radiative recombination process. Thus, its strength and probability compared to the radiative decay process is responsible for the amount of scintillation light generated.

The Förster interaction describes the energy transfer between two excitations in the scintillating material through the non-radiative recombination of one of the them via transferring its energy to the other. As a result, only one excitation is remaining, left in an excited state, which in the further course relaxes to the ground state under the emission of phonons. The strength of the Förster interaction, compared to the competing radiative recombination process, depends strongly on the distance between the excitations and hence on the ionization density of the incident particle traversing the detector. Therefore, the non-radiative process is more dominant for higher ionizing radiation, leading to a decreased generation of scintillation light.

Further information and a very detailed description of the microscopic model of scintillation light generation in CaWO_4 can be found in Ref. [23].

3.2.2. Birks' Model

With the help of a comprehensive microscopic model, as described in the previous section, one can understand all the physical processes underlying the production of scintillation light on an atomic level. Considering the decay-time spectra of the fundamental excitations, even a time-resolved scintillation signal may be modeled and analyzed. However, if one is only interested in the amount of light output and its features, a simpler macroscopic model may be sufficient.

John B. Birks proposed such a phenomenological, macroscopic model [25, 26], relating the light output per path length $\frac{dL}{dx}$ to the energy deposition per path length $\frac{dE}{dx}$ (cf. chapter 4 for a discussion of the contributions to this quantity) via,

$$\frac{dL}{dx} = \frac{A \cdot \frac{dE}{dx}}{1 + kB \cdot \frac{dE}{dx}} \quad , \quad (3.1)$$

which is called Birks' law. If the denominator was ignored, L would be linearly proportional to E with a proportionality constant A . Hence, the light yield LY (cf. Eq. (3.2)) would neither depend on E nor on $\frac{dE}{dx}$ and would take the constant value A . Even the particle type would not play a role. All these dependencies are only taken into account by the factor $\frac{1}{1 + kB \cdot \frac{dE}{dx}}$. The non-zero term $kB \cdot \frac{dE}{dx}$ in this model is responsible for reproducing the observed effects of quenching and non-proportionality, which will be described in section 3.2.3. The term $\frac{dE}{dx}$ essentially corresponds to the ionization strength of the particle and thus, it is a measure of the excitation density generated in the scintillator. The multiplying factor kB , also referred to as Birks' constant, is indeed a combination of two independent factors k and B , where the latter is a proportionality constant that relates $\frac{dE}{dx}$ to the actual excitation density, while k is the probability for the occurrence of a quenching process of some kind.

For higher ionizing particles with a higher local energy deposition the denominator takes a greater value compared to lower ionizing particles, which accounts for the quenching effect. In addition, for a given particle, the value varies with the energy of the particle, in accordance with the change in local energy deposition, hence reproducing the non-proportionality effect (cf. section 3.2.3).

A and kB are material-dependent parameters. To be precise, they are crystal-dependent, meaning that they can vary for different crystals produced from the same material, because they depend on intrinsic properties, like e.g. the defect densities and contaminations. Hence, the parameters of Birks' law have to be determined from light yield data independently for every single crystal.

The basic mathematical formalism describing the quenching process with the help of Birks' constant is equivalent to the description within the microscopic model utilizing the Förster interaction [23, 24]. Therefore, the macroscopic Birks' model

can produce good results in many applications.

The work within this thesis is thus focused on the goal of developing an easy but accurate simulation and analysis model based on Birks' law that can describe and predict light yields and quenching factors of different particles given only the γ -measurement for a crystal.

3.2.3. Scintillation Light Quenching

The reduced amount of light seen for higher ionizing particles hitting the detector is referred to as the quenching of the light signal. As we are not interested in the total amount of scintillation light L detected but rather its amount compared to the energy E_{dep} deposited in the crystal, a new quantity called *light yield* LY is defined. It is the ratio between the light and the phonon signal,

$$LY_x(E_{dep}) = \frac{L_x}{E_{dep}} \quad , \quad (3.2)$$

where x denotes the particle type. By CRESST convention, the LY is normalized to the value obtained through the γ -calibration of the detectors, utilizing a ^{57}Co source, which emits γ -particles of 122 keV. For the calibration peak, the amount of light energy measured by the light detector is defined to take the a value of 122 keV_{ee}, where ee means electron equivalent [27], so that its LY is set to unity,

$$LY_\gamma(122 \text{ keV}) := 1 \quad . \quad (3.3)$$

The LY of γ -particles as a function of deposited energy is parametrized by the equation [28],

$$LY_\gamma(E_{dep}) = (p_0 + p_1 \cdot E_{dep}) \cdot \left(1 - p_2 \cdot \exp\left(-\frac{E_{dep}}{p_3}\right) \right) \quad , \quad (3.4)$$

where the second term (within the big brackets) represents the non-proportionality effect. This effect can, for example, be seen in Fig. 6.1 [27] in our reference data, which will be discussed in section 6.2. If all LYs are normalized to the LY obtained for γ -particles, the result yields the percentage to which the light output of particle x is quenched compared to γ -particles depositing the same amount of energy in the phonon channel. By CRESST convention, the non-proportionality term is not considered in this normalization. Therefore, the resulting values, referred to as *quenching factors* (QFs), are given by [29]

$$QF_x(E_{dep}) = \frac{LY_x(E_{dep})}{LY_{\gamma,np}(E_{dep})} = \frac{LY_x(E_{dep})}{p_0 + p_1 \cdot E_{dep}} \quad . \quad (3.5)$$

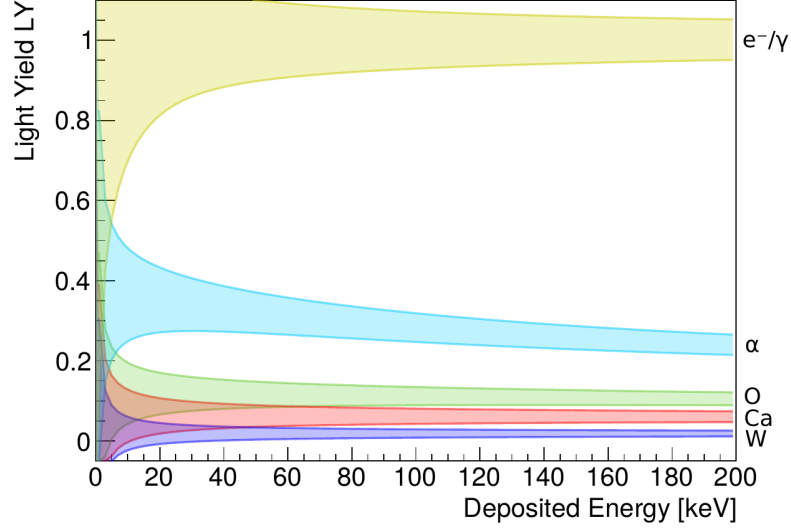


Figure 3.2.: This figure shows an estimate of where the LYs for different particles are found. The e^-/γ band lies by definition around unity, whereas the alpha particles and nuclear recoils are quenched in comparison. Numbers for the different LYs and QFs will be discussed in chapter 6 and 7. This plot was inspired by Fig. 1 within Ref. [30].

Usually, the factor p_0 is close to unity, due to the normalization to the γ calibration peak, and p_1 is very small (i.e. $\mathcal{O}(10^{-5} \text{ keV}^{-1})$) [28], so that for low energies, the QF can be approximated by

$$QF_x(E_{dep}) \approx \frac{LY_x(E_{dep})}{p_0} \quad , \quad (3.6)$$

and is therefore almost equivalent to the LY.

The presentation of CRESST data is mainly done by plotting the LY (or QF) - E_{dep} plane. In this depiction, the band roughly around unity is usually denoted as the e^-/γ band, because the light signal of e^- is similar to that of γ -particles, hence leading to a LY of approximately 1. Bands for alphas and nuclear recoils located at lower LY-values due to the quenching of the scintillation process are separated and analysed thoroughly. A sketch of such a graph is shown in Fig. 3.2. Looking at this figure, one can get a feeling for the range in which the QFs of different particles in CaWO_4 are expected.

Scintillator Non-Proportionality

As already indicated in Eq. (3.5), it is worth noticing that the quenching factors are not constant but vary with energy. This effect could be observed for nuclear

recoils in CRESST analysis for the first time rather recently [28]. However, its existence is fairly obvious when we think of the ionization strength of a particle at different energies. The local energy deposition is not constant but varies with kinetic energy of the particle, e.g. for electrons it increases (for ions it decreases) towards low energies. Therefore, the STE-density is higher (lower) and the ratio between radiative and non-radiative recombinations changes, which moreover influences the light yield (cf. section 3.2.1). This effect is called scintillator non-proportionality, as the amount of photons produced is not just proportional to the energy deposited in the scintillator.

Chapter 4.

Energy Loss Processes of Particles traversing CaWO_4

Understanding the various processes contributing to the energy deposition of different types of particles traversing a scintillating crystal is important for the work performed for this thesis. Firstly, the model which underlies all our simulations is the Birks' model, relating the amount of light produced in the scintillator to the local energy deposition of the corresponding particle. And secondly, a simulation can only give precise results, that are comparable to the experiment, if all possibly occurring physical processes are included in the code.

Thus, an overview of the theory of energy loss processes and models thereof is given in the following sections. The information is specialized on scintillating CaWO_4 crystals and on low particle energies, which are of interest for the work at hand, as the results are analyzed in an energy region up to a few hundred keV. The focus is even set on a lower region up to a few tens of keV, where recoils due to dark matter particles may be expected in the experiment.

4.1. Types of Energy Loss Processes

The total so-called *stopping power*, which is equal to the total energy deposition per path length $\frac{dE}{dx}$, can be considered to be a sum over mean stopping powers due to different processes and interactions that may occur for a certain primary particle in a specific material. It can mainly be distinguished between the following types of energy loss processes:

Electronic stopping: This type of stopping, as indicated by its name, refers to an energy loss of a primary particle due to inelastic collisions with the bound electrons in the target material. If the transferred energy is higher than the ionization threshold, these interactions may lead to the formation of STEs in CaWO_4 through the excitation of electrons to the conduction band (cf. section

3.2.1). Only energy deposited in ionization can thus lead to the generation of scintillation light.

Many different processes are involved in electronic energy loss, depending on the energy of the projectile particle and, when it comes to ions, also depending on its current charge state, which may change in the course of traversing the medium. As a precise description of the latter can hardly be achieved, an average is taken and the electronic stopping power is usually given as a function of energy only.

Nuclear stopping: In contrast to the electronic stopping, in this case the primary particle scatters elastically off an atom or nucleus in the medium. Nuclear stopping does not involve electron excitations, hence it is also referred to by the term 'non-ionizing energy loss' (NIEL). The process may lead to lattice defects, as a nucleus can be knocked off its space if the transferred energy is larger than the displacement energy. Compared to electronic stopping, the contribution of nuclear stopping to the total stopping power increases with decreasing energy and with increasing mass of the projectile particle.

Direct production of phonons: This process is comparable to nuclear stopping. However, the energy transfer is too small to lead to a recoiling nucleus, so that phonons are directly created.

Radiative loss: At high energies, at which the projectile particle starts to emit bremsstrahlung, this process has to be considered and even becomes dominant at some point in the case of electrons.

For the purpose of this thesis, the energy regime, in which radiative losses become relevant, is not of interest. Direct phonon production is also irrelevant for our studies, as we mainly want to investigate nuclear recoils. Therefore, the focus is set on electronic and nuclear stopping. In the following section, the energy loss of different particles traversing CaWO_4 is examined more carefully.

4.2. Energy Loss of different Particles

The main types of energy loss processes, that we distinguish, are electronic and nuclear stopping. However, the contributions of these processes to the total stopping and their mathematical models are highly depending on the type of particle under consideration. The following three subsections deal with the particles of interest for the work presented in this thesis.

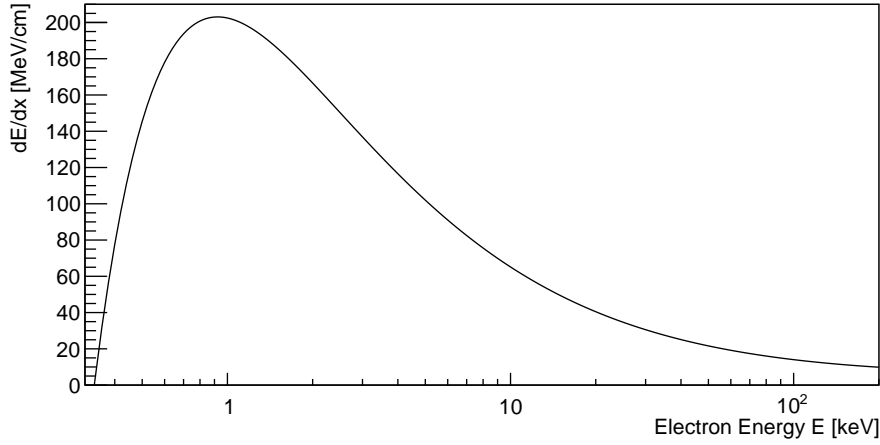


Figure 4.1.: This plot shows the stopping power of an electron in CaWO_4 according to the Berger-Seltzer formula (Eq. (4.2)). A rise towards low energies, peaking at roughly 1 keV, can be clearly seen.

4.2.1. Electrons

Considering electrons traversing a CaWO_4 crystal, only electronic stopping due to collisions with bound electrons occurs in the energy region of interest, while radiative stopping is negligible and nuclear stopping is not present at all. Thus, it can be concluded that the energy of an incident electron is deposited and converted totally into ionization at each event.

The collision stopping power can be described by the Berger-Seltzer formula, which is derived from the Bethe theory making use of the Møller cross section. The stopping power is given by the first moment of the cross section, with the moments being defined by [31]

$$M_j(\beta) = n_e \delta x \int W^j \frac{d\sigma(W; \beta)}{dW} dW \quad . \quad (4.1)$$

The order of the moment M is given by the value of j , while n_e denotes the electron density, β the ratio between the velocity of the incident particle and the speed of light, W represents the energy loss and $\frac{d\sigma}{dW}$ the differential cross section. Taking $j = 1$, one can hence obtain the Berger-Seltzer formula [32],

$$-\frac{dE}{dx} = \frac{2\pi r_e^2 n_e m_e c^2}{\beta^2} \left[\ln \left(2(\gamma + 1) \frac{m_e^2 c^4}{I^2} \right) + \frac{1}{\gamma^2} + \ln \left(\frac{\tau^2}{4} \right) + \frac{\tau^2}{8\gamma^2} - \ln(2) \frac{2\tau + 1}{\gamma^2} \right] , \quad (4.2)$$

where r_e is the classical electron radius of approximately $2.81794 \cdot 10^{-13}$ cm, n_e is the electron density in the medium, which is $1.43 \cdot 10^{24}$ e⁻/cm³ in CaWO_4 , the

combined quantity $m_e c^2 = E_0 = 511$ keV represents the rest energy of an electron and I denotes the mean excitation energy, which is calculated to take a value of 395 eV for CaWO_4 . Furthermore, the value of γ can be dynamically determined by the ratio between the total energy of the electron and its rest energy, $\gamma = \frac{E_{tot}}{E_0}$ and the parameter τ is related to γ via $\tau = 1 - \gamma$. A more detailed description of the equation may be found in the original work by Seltzer and Berger [32, 33] and in the reviews of the Particle Data Group [31].

With the help of all the known quantities, the Berger-Seltzer formula can be plotted as shown in Fig. 4.1. Looking at the logarithmic scale of the horizontal axis depicting the electron energy, one can see, that the stopping power significantly increases towards lower energies (starting roughly below 10-50 keV), peaking at ~ 1 keV. Remembering the connection between the ionization density and the scintillation light generation, also described by Birks' law (Eq. (3.1)), it is obvious at this point that the light output due to incident electrons will be reduced for decreasing electron energy.

4.2.2. Gammas

Talking about electromagnetic radiation in general, energy losses occur through the transfer of energy to electrons. Thus, the formulation given in the previous section can be applied. However, there is a slight difference when it comes to determining the light output and light yield. A γ -particle of a certain energy does not transfer its energy to a single electron but dissipates it to many of them. Thus, various electrons with lower energies and hence higher stopping power contribute to the total energy deposition of a single γ -particle. This leads to a minor reduction of the γ light yield compared to that of an electron of the same energy. The shift of a monochromatic γ -line compared to the electron band can, for example, be seen in Fig. 6.1 at 46.5 keV. In general, this discrepancy is rather small, so that in the experimental data of CRESST the light yield bands of electrons and γ -particles overlap and cannot be clearly distinguished. They are thus combined to form an e^-/γ band.

4.2.3. Ions

For ions traversing a solid, electronic and nuclear stopping are both relevant. While the contribution of electronic stopping increases with increasing kinetic energy and decreasing mass of the particle, nuclear stopping dominates at low energies, especially for heavy charged particles. A sketch of the total stopping power over a broad energy range is plotted in Fig. 4.2 for muons, as an example of a charged particle, in Copper. The different parametrisations in various energy regions are named and

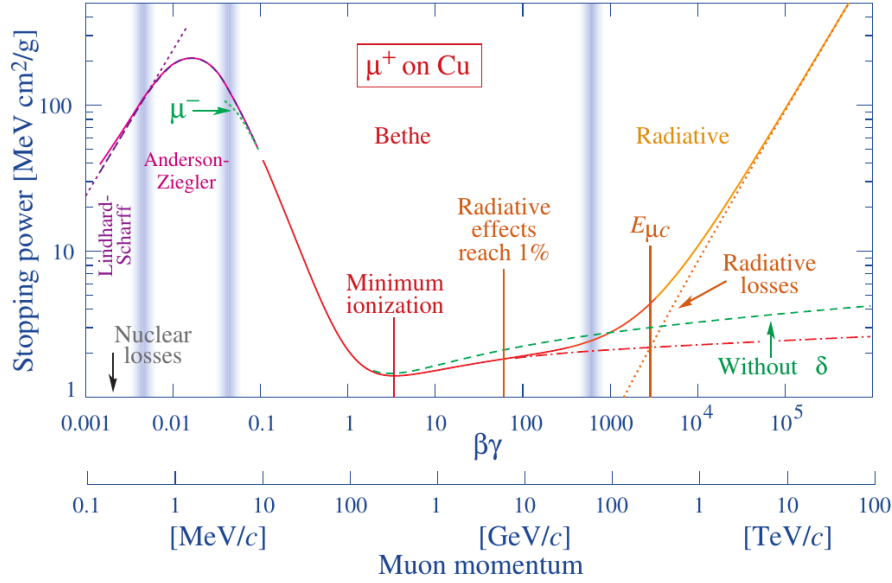


Figure 4.2.: This plot shows the stopping power of a muon (μ^\pm) in Copper. The different processes dominating in a certain energy region are named. Only at the very bottom of the depicted energy range, nuclear stopping comes into play and electronic stopping is described as being proportional to β by Lindhard(-Scharff) theory.

The picture is taken from Ref. [31].

shall be discussed in the following.

The **electronic stopping power** can again be derived from Bethe theory, however using the Rutherford differential scattering cross section. Calculating the first moment of this cross section due to Eq. (4.1) yields the classical Bethe(-Bloch) formula [31, 34],

$$-\left(\frac{dE}{dx}\right)_e = \frac{4\pi r_e^2 n_e m_e c^2 z^2}{\beta^2} \left[\frac{1}{2} \ln \left(\frac{2m_e c^2 \beta^2 W_{max}}{(1-\beta^2)I^2} \right) - \beta^2 \right] , \quad (4.3)$$

where z is the charge of the incident ion in units of the electron charge and all other parameters are the same as defined for Eq. (4.2). W_{max} denotes the maximum energy transfer, given by [31]

$$W_{max} = \frac{2m_e c^2 \beta^2 \gamma^2}{1 + 2\gamma m_e/M + (m_e/M)^2} . \quad (4.4)$$

For low particle energies, at which $2\gamma m_e \ll M$ holds, approximating the maximum energy transfer by $W_{max} = 2m_e c^2 \beta^2 \gamma^2$ is valid, simplifying Eq. (4.3) to

$$-\left(\frac{dE}{dx}\right)_e = \frac{4\pi r_e^2 n_e m_e c^2 z^2}{\beta^2} \left[\ln \left(\frac{2m_e c^2 \beta^2}{(1-\beta^2)I} \right) - \beta^2 \right] . \quad (4.5)$$

Two extensions to this model are usually added to account for effects that may occur in certain energy regions.

The first one is the so-called density effect [31, 34]. At high particle energies, the stopping power increases proportional to $\ln(\beta\gamma)$, because of the change of the particle's electric field, which enhances the cross section for distant collisions. Polarization of the medium limits the effect, leading to a correction in the square brackets of Eq. (4.5) by a function $\frac{-\delta(\beta\gamma)}{2}$. This high energy correction term, however, does hardly play a role in the energy regime considered in the CRESSST experiment.

The second extension accounts for shell corrections [31, 34] at low energies ($\beta\gamma \lesssim 0.3$). A term C/Z has to be included in the square brackets of Eq. (4.5), where C is the shell correction parameter and Z is the atomic number of the target nucleus. The correction takes into account the atomic binding and the fact that the atomic electrons are not stationary. The value of $\beta\gamma = 0.3$, below which this correction becomes relevant, corresponds to a kinetic energy of 4.4% of the rest energy of the incident particle (which is e.g. ~ 661 MeV for an ^{16}O and ~ 7.6 GeV for a ^{184}W ion).

The effect of shell corrections gets larger with decreasing energy, but going to lower energies, also further corrections have to be added. Eq. (4.5) is based on a Born approximation of first order. Higher order terms in the charge of the incident particle guarantee better precision. Therefore, the so called Bloch correction, including a term $z^2 L_2(\beta)$ inside the square brackets of Eq. (4.5) is usually added, which can be seen as the reason to call the equation "Bethe-Bloch equation" instead of just "Bethe equation". An additional correction, called Barkas correction [31, 34], leading to a differing stopping power of negatively and positively charged particles of the same mass and velocity, is added via $zL_1(\beta)$, so that the modified formula now reads [34]

$$-\left(\frac{dE}{dx}\right)_e = \frac{4\pi r_e^2 n_e m_e c^2 z^2}{\beta^2} \times \left[\ln\left(\frac{2m_e c^2 \beta^2}{(1-\beta^2)I}\right) - \beta^2 - \frac{\delta(\beta\gamma)}{2} - \frac{C}{Z} + zL_1(\beta) + z^2 L_2(\beta) \right]. \quad (4.6)$$

A detailed derivation of all the correction terms is given in Ref. [34]. Still, the treatment including these corrections is only accurate down to $\beta \approx 0.05$, which corresponds to a kinetic energy of ~ 19 MeV for ^{16}O ions. Between β values of 0.01 and 0.05, there is no satisfactory theory, but phenomenological fitting functions are applied. Below that energy, Lindhard has proposed a description of the electronic stopping power being proportional to β [35], which accurately describes experimental data.

At such low and even lower energies, **nuclear stopping power** becomes relevant and eventually dominates the total stopping power. The average nuclear stopping

power can be calculated, if the repulsive potential $V(r)$ between the incident particle and an atom in the medium is known. This may be done by integrating the energy $T(E_0, \theta(p, E_C, V(r)))$ transferred in a single nuclear collision event over all possible impact parameters p , given a particle of rest energy E_0 and a center-of-mass energy E_C [36],

$$\left(\frac{dE}{dx}\right)_n(E_0) = \int_0^\infty T(E_0, \theta(p, E_C, V(r))) \cdot 2 \cdot \pi \cdot p \cdot dp \quad . \quad (4.7)$$

The potential $V(r)$ is basically a repulsive Coulomb potential, which is screened by the electrons surrounding the target nucleus in the material,

$$V(r) = \frac{z \cdot Z \cdot e^2}{r} \cdot \Phi(r) \quad , \quad (4.8)$$

where $\Phi(r)$ is the screening function. An analytical solution to Eq. (4.7) does, in general, not exist. However, a numerical solution can be found by introducing the dimensionless quantity ϵ [36],

$$\epsilon = \frac{E_C \cdot a_U}{z \cdot Z \cdot e^2} \quad , \quad (4.9)$$

where a_U is related to the Bohr atomic radius $a_0 = 0.529 \text{ \AA}$ via

$$a_U = \frac{0.8854 \cdot a_0}{z^{0.23} + Z^{0.23}} \quad . \quad (4.10)$$

Now, the nuclear stopping power can be defined via [36]

$$\left(\frac{dE}{dx}\right)_n(E_0) = \frac{\pi \cdot a_U^2 \cdot \gamma \cdot E_0}{\epsilon} \cdot \left(\frac{dE}{dx}\right)_n(\epsilon) \quad , \quad (4.11)$$

with $\gamma = \frac{4 \cdot m \cdot M}{(m+M)^2}$, and an analytical approximation for the nuclear stopping as a function of ϵ can be derived, which yields [36]

$$\left(\frac{dE}{dx}\right)_n(\epsilon) = \begin{cases} \frac{\ln(1+1.1383 \cdot \epsilon)}{2 \cdot (\epsilon + 0.01321 \cdot \epsilon^{0.21226} + 0.19593 \cdot \epsilon^{0.5})} & \text{for } \epsilon \leq 30 \\ \frac{\ln(\epsilon)}{2 \cdot \epsilon} & \text{for } \epsilon > 30 \end{cases} \quad . \quad (4.12)$$

Eq. (4.11) can be rewritten, in order to calculate the nuclear stopping in units of $\text{eV}/(\text{atoms}/\text{cm}^2)$, to

$$\left(\frac{dE}{dx}\right)_n(E_0) = \frac{8.462 \cdot 10^{-15} \cdot z \cdot Z \cdot m}{(m+M) \cdot (z^{0.23} + Z^{0.23})} \cdot \left(\frac{dE}{dx}\right)_n(\epsilon) \quad . \quad (4.13)$$

After the discussion of the models for electronic and nuclear stopping on the previous pages, a general comment shall be given, by having a further look into the

exemplary plot in Fig. 4.2. The depiction only shows the graph down to $\beta\gamma = 0.001$, while the energies that are interesting for this thesis are far below that value. The figure shows that only at the bottommost depicted energy, nuclear losses start contributing and electronic losses are described by Lindhard theory. No precise and extensive, generally applicable theory exists in the very low energetic regime below the bottom limit shown in the plot. Furthermore, as can be seen from the discussion and equations in this section, the theoretical stopping power formulas are applicable only for elemental materials rather than for compounds. Achieving a precise description is hence more difficult for the latter.

Of course, experimental data always provide the most accurate stopping power values. Thus, different collaborations, among them the ICRU (International Commission on Radiation Units) and SRIM (Stopping and Range of Ions in Matter) [37], have collected data and listed them in stopping power tables. Values for all possible single-elemental ions in almost all elemental materials and even in some compounds have been published. Stopping powers of ions in compounds for which no data have been collected may be calculated via Bragg's rule superimposing the stopping powers of the single elements which the material consists of,

$$\left(\frac{dE}{dx}\right)_n = \sum_i w_i \left(\frac{dE}{dx}\right)_{n,i}, \quad (4.14)$$

where w_i denotes the mass fraction of element i in the compound. However, corrections due to the different binding energies of electrons in the compound compared to the free elements have to be taken into account.

The tabulated values are utilized in many simulation softwares, especially in the low energetic regime, where the theory does not match the experiments with high enough precision. Also in the simulations for this thesis, tabulated stopping power values are applied, which will be discussed in detail in chapter 7.

Chapter 5.

Simulation and Analysis Technique

In this chapter, information about the key aspects of the simulated light yield determination shall be given. After presenting an overview of the methodology, the geometry used in the simulations is described. Then, the generation of incident particles is covered, as well as the tracing of their tracks and interactions. In the last sections, the computation of the light yield from the obtained data and the conversion to quenching factors by the normalization to the gamma calibration values is discussed.

5.1. Overview of the Methodology

In the CRESST experiment, phonon and light signal are measured simultaneously, as discussed in section 3.1. Energy depositions in the scintillating CaWO_4 crystal lead to excitations of electrons which may form pairs of self-trapped excitons (STEs) and self-trapped holes (STHs). These can either de-excite to the ground state via emission of optical photons or via a non-radiative recombination process (cf. section 3.2.1 about the microscopic model). A light detector is attached to the target crystal measuring the amount of energy of the optical photons that reach this detector. Not every single photon will hit the light detector, which thus only has a certain detection efficiency. However, the efficiency is independent of the type of incident particle that leads to the phonon and light production. As LYs are calculated via dividing the light energy by the phonon energy (cf. Eq. (3.2)) and normalizing to the value obtained in the gamma calibration, the dependence on the light collection efficiency cancels and LYs and QFs for each particle are independent of the efficiency. For this reason, we do not simulate the light propagation in this work, but calculate the LY directly by using the deposited energies. For consistency checks, however, we did a small simulation with activated light propagation (characteristic values for CaWO_4 therefore needed in the simulations could be found in Ref. [38, 39] and online at <http://scintillator.lbl.gov/>), but as expected we found no deviation with our approach.

All simulations conducted for the work of this thesis are based on the Geant4 (v.10.2.1) simulation code, which has dedicatedly been developed for the simulation of the passage of particles through matter on a single-event basis. The results that we obtain are analysed with the help of ROOT (v.6.36.36). A more detailed description of these software packages is given in appendix A.

Our method aims for the description of the QFs of nuclear recoils via a semi-empirical model based on Birks' law (Eq. (3.1)). Energy depositions simulated with Geant4 are inserted into this equation. Employing experimental input values for the Birks parameters A and kB (cf. section 6.1), the light output and in the further course LY and QF of an incident particle can be calculated. The results are compared to experimental reference data of single scattering events (cf. section 6.2). If distinct sources are taken, it is crucial to ensure, that the experimental data used as an input for the calculation and those used as a reference for our results are compatible.

Ideally, this methodology shall lead to a reduction of the free parameters needed for the parametrization of the experimental LY/QF data from 9 to 2, i.e. A and kB .

5.2. Geometry and Particles used in the Simulations

The geometry mainly used in the simulations for this thesis is very simple. As for our purpose, only the interactions of an incident particle with the detector material is of interest, we do not need to take into account the full detector geometry including the housing and holders of the crystal. Hence, a free floating CaWO_4 crystal surrounded by vacuum is simulated. Also the shape and size of the crystal does not have noticeable impact on the results, as long as the dimensions are not that small that incident particles may likely undergo no interactions within the detector volume. Thus, a cubic crystal with a side length of 64 mm is defined, as it was used in the detector 'TUM40' of CRESST.

For the main part of the simulations, incident particles are started on the surface of a sphere around the cube, where they are randomly distributed. Their initial momentum direction points inwards, i.e. towards the crystal, defined by random angles between $0 \leq \theta \leq \frac{\pi}{2}$ and $0 \leq \phi \leq 2\pi$. The upper bound for θ can be reduced to prevent momentum directions close to the tangents of the sphere, which lead to particle tracks not crossing the target volume.

The incident particles used in the simulations are e^- , γ -particles, α -particles and neutrons. The latter can lead to recoiling nuclei (O, Ca, W) in the crystal, from

which corresponding data can be collected. If the focus is set on the light yield data of these nuclear recoils rather than on the entire light yield spectrum due to interactions of primary neutrons, which can also scatter inelastically or on multiple nuclei, a lot of simulation time and memory space can be saved by directly starting O, Ca and W ions instead of neutrons. In this case, the particles are obviously not started outside the cube but at a random position inside the crystal.

The energies of all the particles are chosen such that data in the desired energy region (e.g. for comparison to a reference plot) are produced. For particles which usually deposit their whole energy in the crystal, a uniform distribution of energies between $0 \leq E_{kin} \leq E_{kin,max}$ is defined (e.g. $E_{kin,max} = 600$ keV for the studies in chapter 7). This is the case for e^- , γ -particles, α -particles and for the O, Ca and W ions. If, however, neutrons are started, a mono-energetic beam is simulated. Secondary recoil ions are then created via elastic scattering, so that their kinetic energies can again take values between zero and a certain maximum given due to kinematics. The maximum, in this case, is different for different ions. An incident neutron of 11 MeV, for example, can lead to recoils of W up to ~ 250 keV, of Ca up to ~ 1000 keV and of O up to ~ 1800 keV.

5.3. Particle Cascade identification and allocation

An incident particle, that reaches the detector crystal, interacts with the electrons, nuclei or with the whole atoms within the material. Usually, besides generating excitations and depositing energy directly into phonons, this also leads to the production of secondary particles. The energy and type of the incident particle determines, if and which further secondaries may be created. Hence, daughter particles can generate secondary particles themselves, until their energy is not high enough any more. A single primary particle hitting the detector can therefore lead to a cascade of particles in the material, which all contribute to the energy loss process and energy deposition within the crystal. A schematic illustration of such a cascade is depicted in Fig. 5.1.

It is crucial that these particle cascades can be identified in the simulation and that the data can be allocated to the particle initially creating the cascade, as all energy depositions of the primary particle together with those of the secondaries add up to the total energy deposition. The same is true for the scintillation light output and as a consequence also for the light yield (cf. Eq. (3.2)). Due to the single event basis of the Geant4 simulations and the data storage in tree format, tracking the cascade can be done by applying a ROOT script to the data file, that has been created during simulation, running a recursive loop over all the secondary tracks.

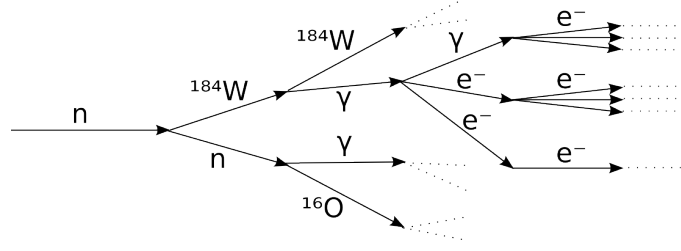


Figure 5.1.: This graphic shows an example of a particle cascade induced by a neutron within CaWO_4 . The incident neutron scatters elastically off a tungsten nucleus and then inelastically off oxygen. Inelastic processes lead to production of γ -particles, which result in electromagnetic cascades of electrons and further photons. The dots at the end of the arrows indicate that the particle cascade might not end at this point.

The script invokes the following steps (its code can be found in appendix B.2): After establishing access to the stored data in the output .root-file, the loop over all events in the input .root-file begins. For every event, the data of the primary particle (in our case e^- , γ , α , n , O , Ca or W) are extracted. Within this function, a loop over all 'hits', i.e. interactions, of the particle is performed, storing mainly the energy deposition and step length for each of them. Then, the same function is called again for all secondary particles caused by the primary one. The same type of data are thus recorded and are allocated to the particle that caused the cascade. This behavior is recursively repeated for the tertiary etc. tracks. Initially, the cascade is assigned to the primary particle. However, if the recursion encounters a recoiling Ca , O or W ion, a new cascade is defined and assigned to the recoiling ion. This new cascade now contains all secondary particles caused by the recoil. With this method the whole cascade is portioned and each interaction is assigned either to a recoiling ion (Ca , O , W) or to the primary particle.

After the whole cascade of secondary particles is processed, the light output dL in each step is calculated via Birks' formula (Eq. (3.1)) rewritten to

$$dL = \frac{A \cdot dE}{1 + kB \cdot \frac{dE}{dx}} \quad , \quad (5.1)$$

where dE and dx are the corresponding energy deposition and step length, while A and kB are crystal dependent input parameters, as discussed in section 3.2.2. The computed light outputs together with the energy depositions can then be used to determine the light yield of either the recoiling ions or, by summing up the sub-cascades, the primary particle.

5.4. Light Yield Computation

The ROOT script described in the previous section stores the light outputs and energy depositions (and further data needed for the analysis) in a .root-file. This output can then be used by a further script to calculate and plot the light yields (LYs) of all events.

The LY is defined as the ratio between the total light output and energy deposition (Eq. (3.2)) of a particle hitting the detector. For a precise calculation, one would have to calculate the integral over all light outputs,

$$LY(E) = \frac{L}{E}(E) = \frac{1}{E} \int dL = \frac{1}{E} \int_0^E \frac{dL}{dE'} dE' \quad , \quad (5.2)$$

inserting Eq. (5.1) for the infinitesimal light output.

However, if enough steps are performed in the stopping processes of the particles, approximating the integral by a sum is sufficient, so that

$$LY(E) = \frac{1}{E} \sum \Delta L = \frac{1}{\sum \Delta E} \sum \Delta L \quad . \quad (5.3)$$

This is the form of the equation used in our LY calculation script. The values of the single energy depositions ΔE and light outputs ΔL calculated with the help of Eq. (5.1) are stored in the output .root-file that is created as described in the previous section. Hence, the calculation is a rather easy task, given that the data preparation works properly.

5.5. Normalization to 122 keV Gamma Events

When discussing the scintillation light output and quenching in section 3.2.3, it has been mentioned that, by CRESSST convention, the light yields are normalized to the value obtained with γ -particles of 122 keV emitted by a ^{57}Co calibration source (cf. Eq. (3.3)). This has to be done in the simulations as well, in order to make the results comparable. After conducting the simulation, the calculation of the light yield is done according to the method described in sections 5.3 and 5.4, which can be applied to any type of primary particle. For the Birks parameters kB and A , we have to use experimental reference values, which will be discussed in section 6.1. Then, the mean LY of the obtained photo peak located at 122 keV, representing the γ -particles which deposit their whole energy in the crystal, is used for the normalization. Therefore, a Gaussian,

$$q_0 \cdot \exp \left[-\frac{1}{2} \left(\frac{LY - q_1}{q_2} \right)^2 \right] \quad , \quad (5.4)$$

is fitted to the number of data points in the LY histogram in the corresponding range of deposited energies, where q_1 yields the value for normalization. The actual simulation is presented in section 7.2.

5.6. Quenching Factor Calculation

To further compute the quenching factors (QFs), γ -particles of different energies have to be simulated and the phenomenological parametrization given in Eq. (3.4) has to be fitted to the data in the LY - E_{dep} plane. In section 7.2, this procedure is discussed for the actual simulation and depicted in Fig. 7.3. The QFs of all particles, i.e. the relation of their LYs to that of a γ -particle depositing the same amount of energy, can be calculated with the help of this fit according to Eq. (3.5). Due to the behavior of the LY of γ -particles, the fit usually yields values of p_0 close to unity and $p_1 \ll 1$. Hence, the QFs at low energies are almost equivalent to the normalized LYs.

Chapter 6.

Reference Values for our simulated Results

The simulations of light yields based on Birks' law require input values, namely the crystal dependent parameters A and kB of Eq. (3.1). These have to be taken from a measurement of a real CaWO_4 crystal and the simulated results that are obtained with these parameter values have to be compared to respective experimental results. The experimental data we used as a reference are discussed in the following sections.

6.1. Birks' parameters

Birks parameters of CaWO_4 crystals used in the CRESST experiment have been determined for different crystals in the past. One example is given in Ref. [27], where Lang et al. measured the corresponding values of A and the Birks constant kB for detector module 'Daisy' based on data taken in CRESST run 27 and an exposure of 12.31 kg d, where they also studied the scintillator non-proportionality effect. Electron data were measured with the detector module mainly due to an internal contamination with ^{90}Sr and a smaller fraction of other beta emitters. No gamma calibration source was present at the time of their data taking, but some additional gamma lines resulting from internal and external sources are superimposed to the continuous electron spectrum. The plot of data points in the LY - energy plane they obtained is depicted in Fig. 6.1, where mean LY values are indicated by white data points with error bars. At least in one energy bin, the contribution of a gamma line is clearly visible at lower LY compared to electron events. The reason for the reduced LY of γ -particles is the share of their energy over several electrons of low energy which results in a lower LY (cf. section 4.2.2 for details). Responsible for the visible γ -line at 46.5 keV is an external contamination with ^{210}Pb .

Lang et al. fitted the mean electron LYs by integrating Birks' law (Eq. (3.1)), which yields an equivalent representation as in Eq. (5.2). For the stopping powers (dE/dx) , values were taken from the 'estar' database [40], for which one can read

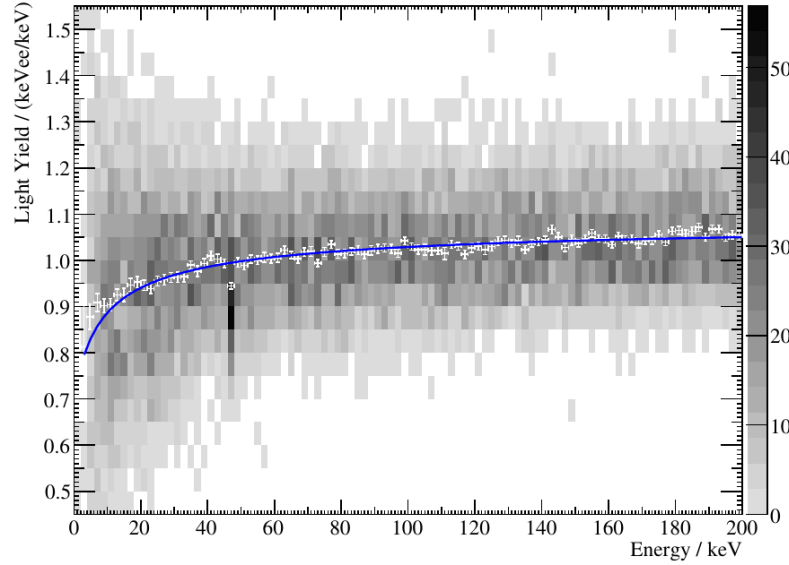


Figure 6.1.: Number of events as a function of LY and E_{dep} . White marks indicate the LY averaged over 2 keV, fitted by Birks' law (blue line). The data correspond to an exposure of 12.31 kg d acquired during CRESST run 27. Figure taken from Ref. [27].

on their homepage, however, that the Bethe theory and proceedings proposed by Berger and Seltzer [32, 33] are used to describe electronic stopping power. The Berger-Seltzer formula has been discussed in section 4.2.1 (Eq. (4.2)) already.

Conducting the fit, Lang et al. could obtain the Birks parameters for the CaWO_4 crystal 'Daisy', which are given by the values $A = (1.096 \pm 0.003)$ $\text{keV}_{ee}/\text{keV}$ and $kB = (18.5 \pm 0.7)$ nm/keV . The keV_{ee} unit is introduced in the gamma calibration and defined, so that the scintillation light energy of a 122 keV γ -particle, depositing its whole energy in the crystal, is 122 keV_{ee} (cf. section 3.2.3). The parameter A is hence expected to take a value close to unity, as it describes the linear dependence of dL/dx on dE/dx in the absence of scintillator non-proportionality, i.e. at high energies.

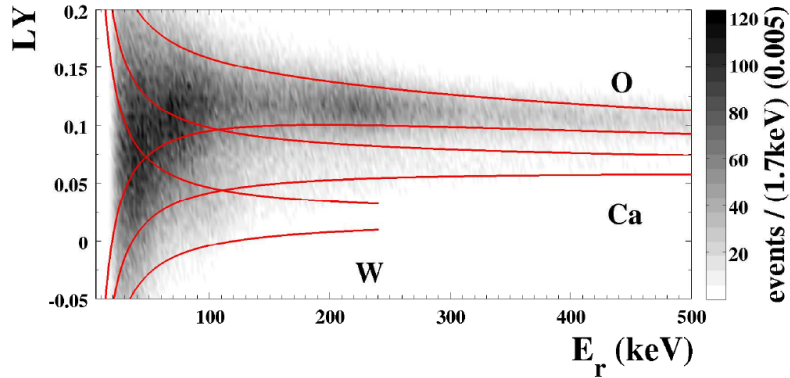


Figure 6.2.: Nuclear recoil data in the LY - energy plane induced by a mono-energetic 11 MeV neutron beam are depicted in a 2D histogram. The solid red lines indicate 1σ bounds for O, Ca and W events, adjusted to the data with the help of a correlated maximum likelihood (ML) fit.

The plot is taken from Ref. [28].

6.2. Quenching Factor Data

The best dataset for the whole spectrum of particles and their respective quenching factors (QFs) seen in the detectors would obviously come from the same CRESST run and the same detector module, that have been used to determine the Birks parameters described in the previous section. However, such data about module 'Daisy' in CRESST run 27 could not be found. Hence, other compatible data had to be taken.

As a reference for the QF of α -particles, the studies of backgrounds in the CRESST experiment by K. Schaeffner [22] were employed. For her dedicated *alpha* analysis, she used CRESST detector module K09. Within her work, she could show the energy dependence of the QF of α -particles for the first time. However, since the introduction of the TUM40 detector design in CRESST, the collected data are far less susceptible to the alpha background [30]. For this reason, we lay our focus on the studies of nuclear recoils in this thesis.

The most recently published measurements of QFs of O, Ca and W in CaWO_4 are taken as a reference. These were conducted by R. Strauss et al. [28, 29] at the neutron-scattering facility of the Maier-Leibnitz-Laboratorium (MLL) in Garching. They used a CRESST-like detector module called 'cw520' in the experiment, which was irradiated with a mono-energetic neutron beam of 11 MeV.

The mean light yield (LY) of the e^-/γ events is parametrised via the phenomenological model given by Eq. (3.4), normalized to unity for $\text{LY}_\gamma(122 \text{ keV})$ by the usual CRESST convention. This phenomenological approach gives rise to a similar

	LY_x^∞	f_x	λ_x
O	0.07908 ± 0.00002	0.7088 ± 0.0008	567.1 ± 0.9
Ca	0.0595 ± 0.0008	0.189 ± 0.002	801 ± 19
W	0.021 ± 0.002	—	—

Table 6.1.: The values given in this table are results of the ML analysis for the parameters of the phenomenological LY parametrization due to Eq. (6.1) as given in Ref. [28]. 1σ confidence limits of the statistical errors are added.

parametrization of the LYs of nuclear recoils. The data measured for O, Ca and W are depicted in the LY - energy plane in Fig. 6.2. The solid red lines were derived from a correlated maximum likelihood (ML) fit and give the 1σ acceptance bounds, within which O, Ca and W events are expected. At low energies these bands can be seen to overlap. Thus, the fitting technique was refined with the help of two assumptions. The first one is, that the mean LY of O and Ca recoils can be phenomenologically parametrized similarly to the one of γ -particles via

$$LY_x(E_r) = LY_x^\infty(1 + f_x \exp(-E_r/\lambda_x)) \quad , \quad (6.1)$$

where LY_x^∞ is the high energy limit of the LY (at $E_r = \infty$), f_x is a measure for the energy-dependence of the LY of nucleus x as well as λ_x , which determines the exponential decrease with increasing energy. The second assumption takes a constant value for the mean LY of W recoils.

The results that could be obtained in [28] with the help of these hypothesis lead to the fit values listed in Tab. 6.1. The corresponding functions are normalized to the LY of the gamma calibration and the QFs are plotted in Fig. 6.3. Shaded areas around the mean value in the graphic indicate the 1σ and 2σ limits due to statistical and systematical errors. It has to be mentioned that systematic errors dominate in comparison to the statistical ones that are given in Tab. 6.1, which would hardly be visible in the plot alone. Further looking at the graphic, an energy dependence of the QFs is clearly visible. Although expected from theory and predicted, for example, by Birks' model, this was the first time that the effect of non-proportionality could be observed for the nuclear scatters in CaWO_4 .

As no information on the determination of Birks parameters for crystal 'cw520' can be found, we are not able to do the simulations directly for this crystal to compare the results. As stated in the previous section, we take the A and kB values of CRESST detector module 'Daisy' instead. Hence, one has to come up with a way to relate the results of the different crystals to each other. Such a conversion has been proposed by R. Strauss et al. as well [28, 29]. The QFs of the different CRESST detector modules have been analyzed, mainly for O-events between 150 and 200 keV, as they dominate at these energies due to kinematics. A

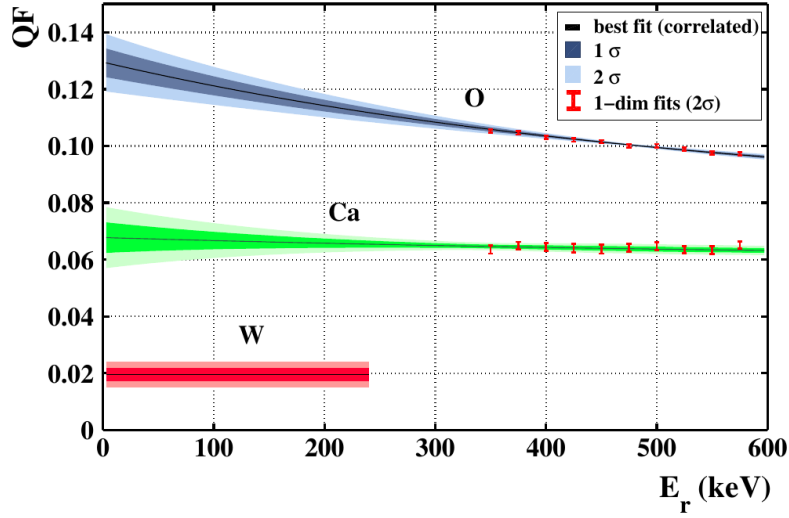


Figure 6.3.: The phenomenological parameterizations (Eq. (6.1)) are plotted for the parameter values given in Tab. 6.1 determined via the correlated ML fit. Shaded error bounds depict the 1σ and 2σ confidence limits. The red error bars starting at 350 keV are results of a 1-dim fit which obviously agree with ML analysis.

Figure taken from Ref. [28].

variation between the different modules could be found with the highest QF being 11% above the lowest and the mean QF of all modules being 12% lower than the QF measured for the crystal 'cw520' used in their work (see Tab. 6.2). This variation could be found to be correlated to the optical quality of the crystal. The higher the defect density, the lower is the absolute light output. However, this dependence seems to be weaker for nuclear recoils compared to electrons or gammas. This proposition is in agreement with simulations presented in Ref. [23]. Thus, the QF, relating the LY of a nuclear scatter to the LY of a γ -particle, which deposits the same energy, is higher for a crystal with higher defect density.

In Ref. [28], a simple, linear model is proposed for the conversion of the QF_x^{cw520} measured for 'cw520' to any other of the CRESST detector modules, which reads

$$QF_{x,i}(E_r) = \epsilon_i \cdot QF_x^{cw520}(E_r) \quad . \quad (6.2)$$

Here, x denotes the nucleus and i the detector module. A list of the ϵ values is given in Tab. 6.2 and Ref. [29]. Thus, when doing the simulations with the Birks parameters of 'Daisy', we have to validate the results based on QFs that are shifted compared to those depicted in Fig. 6.3 by a factor of $\epsilon_{Daisy} \approx 0.94$.

For the detector module K09, used for the alpha background analysis [22], however, no nuclear recoil data are available and hence, no ϵ value can be extracted.

crystal	ϵ	$\text{QF}_O(175 \text{ keV})$
VK33	0.88 ± 0.007	0.102 ± 0.001
Verena	0.91 ± 0.017	0.106 ± 0.002
Maya	0.88 ± 0.007	0.103 ± 0.001
Sabine	0.86 ± 0.01	0.100 ± 0.001
Wibke	0.87 ± 0.009	0.101 ± 0.001
K07	0.85 ± 0.01	0.098 ± 0.001
Daisy	0.94 ± 0.02	0.109 ± 0.002
Rita	0.84 ± 0.006	0.098 ± 0.001
cw520	1.00(def)	0.1159 ± 0.002

Table 6.2.: The difference between quenching factors of various CaWO_4 crystals can exemplary be seen from the tabulated values for O recoils of ~ 175 keV. QFs of distinct detector modules are related to the QF of crystal 'cw520' via the ϵ factors, as described in the text.
Data taken from Ref. [29].

This is not a huge issue as our work is generally focused on nuclear recoils. Still, we have to keep in mind that all comparisons of simulations of α -particles contain errors of up to 16 %, taking into account the variations of ϵ values in Tab. 6.2.

Chapter 7.

Simulation Models and Results

Within the following sections, all the simulation models that we applied are explained and results and comparisons to the experimental data are presented. The chapter starts with a section about the baseline physics implementation in Geant4. Afterwards, the results of our simulations are presented. Issues with and possible extensions to the default physics models and to the way that particle tracks are simulated are discussed. The extensions presented in sections 7.4 - 7.7 went hand in hand with writing additional code classes and functions in complement to the existing code and adopting further data files on the stopping power of ions.

The structure within the sections 7.3 - 7.7, each covering a specific model, are similar. First, the relevant code adaptations are explained and the motivation for each extension to the default Geant4 settings is stated. Then, the results of the simulations are presented and discussed with regard to the experimental reference data. Finally, a conclusion on the goodness of the model with respect to describing real data is drawn and possible improvements to this model are mentioned.

7.1. Baseline Physics Implementation in Geant4

The starting point of our work is the ImpCRESST simulation framework based on standard Geant4 code. A short description of the functionality of the Geant4 software is given in appendix A.1. There, we also explain how to define the parameters of the simulations and to start the desired amount of particles. In the following, however, after stating the geometry used for our simulations, we want to give a more detailed overview of code files that are important to us.

Simulation Geometry

The detector material and geometry have to be implemented in the code framework and called by their corresponding names when starting a simulation (cf. appendix A.1.1). We use a CaWO_4 cube with the dimensions of the TUM40 crystal, free

floating in vacuum, as a target. The primary particles are started randomly distributed on a sphere around this cube with inwards pointing momentum. A more detailed description is given in section 5.2.

Important Source Files and Procedures

For the purpose of this thesis, the stopping process of particles within the detector material is investigated. The interesting part of the simulation therefore happens when the particle reaches the detector volume and undergoes interactions. These are treated by various code files and classes. For a certain kind of interaction, e.g. Compton scattering, different models may exist for different energy regions. As our simulations are conducted for low energies of maximally 2 MeV (but mainly rather in the keV regime), only one of these will be important for us, however. The classes of highest relevance are discussed in the following:

- **G4StandardPhysics_option4:** This class is one of the standard physics lists for electromagnetic physics in Geant4. Among the available options (1-4), this option is recommended by Geant4 (see e.g. in the Geant4 User's Guides).

In this file, a loop over all particle types is performed and the corresponding electromagnetic models that may occur are assigned to each of them. The particles and energies of our simulations constrain these models to some that may be important:

- For low-energetic γ -particles, Compton scattering, the photoelectric effect, gamma conversion and Rayleigh scattering are implemented via the `G4LivermoreComptonModel`, `G4LivermorePhotoelectricModel`, `G4PenelopeGammaConversionModel` and `G4RayleighScattering` respectively.
- The possible interactions of electrons are multiple scattering, ionization and bremsstrahlung, described by `G4UrbanMscModel195`, `G4eIonisation` and `G4eBremsstrahlung`.
- For α -particles, multiple scattering, ion ionization and nuclear stopping may happen as described by the classes `G4hMultipleScattering`, `G4ionIonisation` and `G4NuclearStopping`. Multiple scattering, however, is neglectable in our simulations.
- Charged particles of a single element with atomic number greater than 2 are summarized by the term 'GenericIon' and can interact the same way as α -particles. However, their ion ionization process is simulated with the help of `G4IonParametrisedLossModel`.

With the forward look to the results that we are obtaining and our special in-

terest in the energy loss process of ions in the detector, the classes responsible for electronic and nuclear stopping of ions are discussed in more detail.

- **G4IonParametrisedLossModel:** This class deals with the electronic stopping of ions heavier than helium. As its name suggests, no analytical or numerical calculations of stopping powers are conducted in the principal part, but parametrized values are used. The ICRU (International Commission on Radiation Units) published stopping power tables for ions in elemental materials as well as in some compounds in their ICRU 73 report [41]. These tables together with updates on further projectile-target combinations are saved at a designated location in the Geant4 code repository and are loaded in the constructor of the parametrised loss model. In the initialisation step, dE/dx is sampled at distinct energies for all ion material combinations relevant for the simulated geometry. The tabulated values for the stopping powers are used for ion energies below 1 GeV/nucleon. Above that energy, the Bethe-Bloch formalism (cf. section 4.2.3) would be used, which is, however, far above the scope of energies in our simulations.

If a compound target is not covered by the tables, as is the case for CaWO_4 , Bragg's additivity rule is used (cf. Eq. (4.14)). This means that the stopping power within the compound is calculated by adding up the stopping powers in all elemental constituents weighted with respect to their atomic number density.

- **G4NuclearStopping:** In Geant4, this is the only option for the treatment of nuclear stopping. The model specified in this class for the calculation of the stopping power is `G4ICRU49NuclearStoppingModel`. Again, this is a parametrized model taking values published in the ICRU 49 report. However, having a deeper look into the code, it can be seen that it is actually 'semi-parametrised'. The function `NuclearStoppingPower` makes use of the proceedings described in section 4.2.3, resulting in Eq. (4.13). The prefactor and the reduced energy occurring in this equation are calculated analytically, but the stopping power for the reduced energy is computed with the help of tabulated values.

A technical description of how the listed classes contribute to the simulated energy loss process in Geant4 can be found in appendix A.1.2 for the example of an ion. In the following, a brief physical explanation thereof shall be given:

The different energy loss processes of a particle are not treated simultaneously, but are invoked one after another. Electronic stopping is the first process taken into account. The step length of the process in the simulation is chosen according to the inverse of the cross-section for an electronic energy loss, i.e. the associated mean free path. In parallel, a maximum range for the particle in the material, based on the respective electronic stopping power, is calculated. If the step length at some

point exceeds this range, i.e. the probability for further interactions drops below a certain value, the final step is reached and the particle is stopped.

After covering electronic stopping, nuclear stopping is taken into account. The projectile energy used for this calculation is defined as the mean kinetic energy between the initial value before the step and the one after subtracting the proposed electronic energy loss. This value is then taken as an input for the proceedings described above and in section 4.2.3.

Implementation of Parametrized Stopping Powers

Understanding the default method, by which ICRU electronic stopping powers are made available for the `G4IonParametrisedLossModel`, is necessary for future adaptations. Therefore, a more detailed explanation than above shall be given.

The ICRU electronic stopping powers are stored at a designated place in the code repository of Geant4, namely in a sub-folder that can be found in `share/Geant4-10.2.1/data/G4EMLOW6.48/ion_stopping_data/icru73`, within the main folder of the Geant4 software. The version numbers can, of course, differ from the ones stated above. This `icru73` folder contains files named `zZZ_YY.dat`, which is a special format used to assign the correct file to a projectile-material combination. `ZZ` denotes the atomic number of the incident ion and `YY` the atomic number of an elemental material or the name of a compound material, e.g. `G4_AIR`, for which data are available. The file content is also written in a specific format, needed to make the data readable for Geant4. The first line of a file gives the minimum and maximum energy covered by the table in units of MeV per nucleon and states the number of energy entries in the table. The second line repeats the number of entries in the table. Finally, starting from the third line, the actual two-column table is written. The first column represents the energy per nucleon in MeV and the second one the mass stopping power in $\text{MeV cm}^2 / \text{mg}$. The data tables are added to the parametrised loss model in the constructor of `G4IonParametrisedLossModel` via the function `AddDEDXTable(name, source folder, scaling)`, where the name is `ICRU73`, the source folder, using `G4EMLOW6.48` as the starting directory, is given by `ion_stopping_power/icru73` and `scaling`, which is written dedicated to the table format of the source files, is implemented due to `G4IonDEDXScalingICRU73`. Each ICRU table contains 53 entries for energies between 0.025 and 1000 MeV per nucleon. An interpolation and extrapolation is employed to cover the whole energy range.

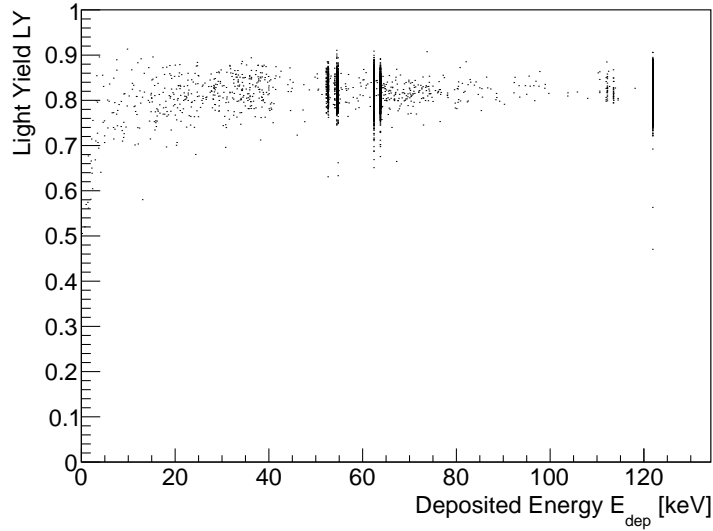


Figure 7.1.: The light yield (LY) of γ -particles with incident energy of 122 keV hitting a CaWO_4 crystal is plotted against the energy deposited in the material. Points distributed over the whole energy range due to Compton scattering and escape lines at specific energies are visible as well as the photo peak at 122 keV.

7.2. Gamma Calibration Simulation

By CRESST convention, a ^{57}Co source emitting γ -particles of 122 keV is employed for the calibration of a target crystal. The observed data are then used for the normalization of all further results. This procedure is already described in sections 3.2.3 and 5.5.

The same normalization obviously has to be applied in our simulations. Therefore, γ -particles of said energy are started in our simulation geometry (cf. section 5.2) initially. The calculation of the light yield is done according to the method described in sections 5.3 and 5.4, which can be applied to any type of primary particle. For kB and A , we used the experimental reference values discussed in section 6.1. The result, starting 75,000 incident γ -particles, is depicted in Fig. 7.1, which shows the data points in the LY - E_{dep} plane. The continuous distribution of data points across all values of deposited energies appears due to Compton scattering. Also visible are several escape lines at specific positions. The most prominent line, however, is the photo peak at 122 keV, which represents the γ -particles depositing their whole energy in the crystal. The mean LY of this peak is used for the normalization and determined by fitting a Gaussian (Eq. (5.4)) to the number of data points in the LY histogram. We chose an energy range between $120 \text{ keV} < E_{\text{dep}} <$

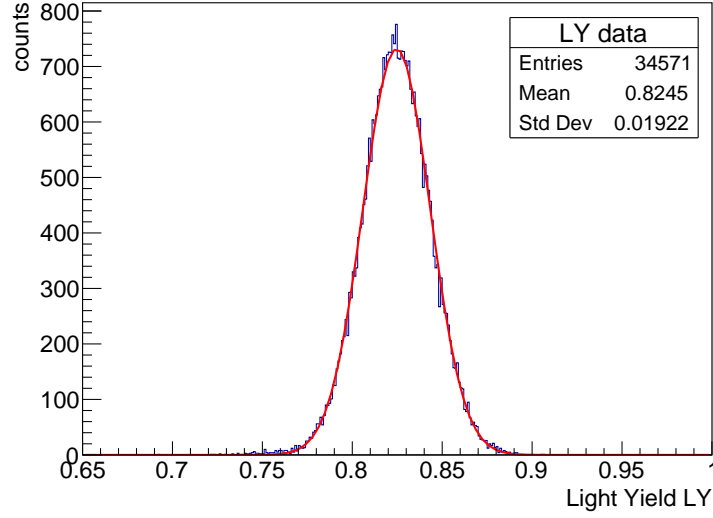


Figure 7.2.: A histogram is filled with the light yield (LY) of events at the photo peak of the gamma calibration (cf. Fig. 7.1) choosing a range of $120 \text{ keV} < E_{dep} < 124 \text{ keV}$ around the peak for the projection. The red curve shows the fitted Gaussian determining the mean LY.

124 keV for the corresponding fit. In Fig. 7.2, the histogram and fit is depicted. The mean LY is given by the mean of the Gaussian, which in our case takes the value

$$LY_{\gamma, norm} = 0.82463 \pm 0.01871 \quad . \quad (7.1)$$

With the help of this value, the normalized LYs for all particles can be calculated.

To further attain the quenching factors (QFs), the method described in sections 3.2.3 and 5.6 is applied. For this purpose, γ -particles of different energies are simulated and the phenomenological parametrization given in Eq. (3.4) is fitted to the data in the LY - E_{dep} plane. This procedure is shown in Fig. 7.3, where the green line represents the corresponding fit to the black data points. The parameter values determined for further use are $p_0 = 0.975 \pm 0.001$ and $p_1 = (2.23 \pm 0.13) \cdot 10^{-4}$. These values are used to calculate the QFs according to Eq. (3.5). Due to the value of p_0 close to unity and $p_1 \ll 1$, the QFs at low energies are almost equivalent to the normalized LYs.

The calibration values determined in this section will be true for all simulations presented in the following. They do not depend on the modifications applied in sections 7.4 - 7.7, because these are only targeting and influencing the simulation of α -particles and ions.

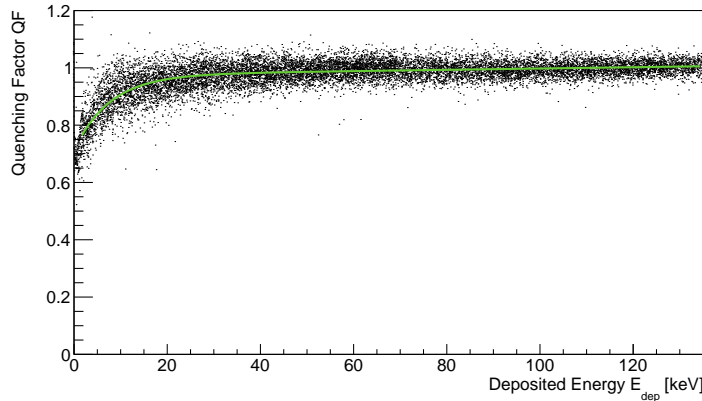


Figure 7.3.: Fit according to Eq. (3.4) (green line) to the simulated and normalized LY data (black points) of γ -particles with initial energies uniformly distributed between 0 and 135 keV.

7.3. Standard Geant4 Settings

Our first LY simulations are conducted with the default settings of the Geant4 code distribution. No modifications and extensions to the classes described in section 7.1 are applied.

Simulation and Results

In the following, the results of the simulations shall be presented. The technique explained in chapter 5 is applied to extract the important data from the .root files created during the simulations and to calculate the light yields (LYs) and quenching factors (QFs) of all the particles hitting the detector. Three different types of simulations, shooting electrons, alphas and neutrons at the CaWO_4 crystal, contribute to the illustration of LYs in Fig. 7.4.

The electron LY, depicted in yellow, shows the expected behavior, being at unity or slightly above (as it should be a little higher than the LY of γ -particles which is normalized to unity at 122 keV, cf. section 4.2.2) across the largest part of the energy region, only decreasing at very low energies, i.e. below ~ 10 keV. This is exactly what is supposed to happen, if we look at the depiction of the electron stopping power in Fig. 4.1, which strongly increases for energies below this value, and remember how the stopping power correlates to the effect of non-proportionality. This correlation can, for example, also be seen from the denominator of Birks' law (Eq. (3.1)). The electron band therefore looks very similar to the one in the experiment.

However, the other LY data seem to be incorrect, even comparing them only to

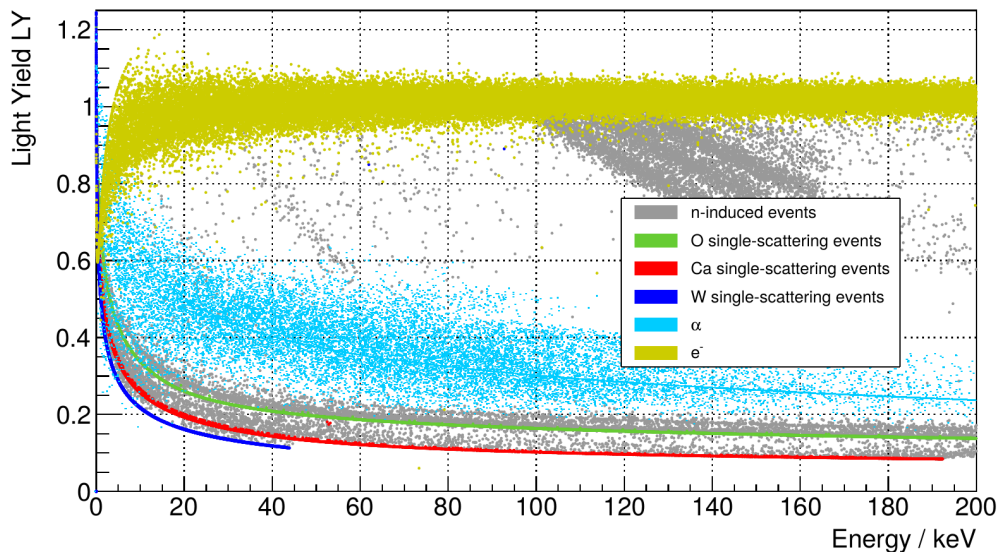


Figure 7.4.: The graphic shows the calculated LYs within CaWO_4 , when simulations are conducted with default Geant4 settings. Normalization to 122 keV gammas is applied, so that the yellow electron band is roughly at unity. The light-blue data points represent α -particles. All remaining events are neutron-induced. In gray, inelastic neutron scatterings and scatterings off multiple nuclei can be seen, while in green, red and blue, the single scatterings off O, Ca and W, respectively, are depicted.

the rough estimates in Fig. 3.2. First, we discuss the LY obtained for α -particles, afterwards the LYs of neutron-induced events, before we finally discuss possible explanations for the observed deviations.

In Fig. 7.4, the α -data are represented by the very broad light-blue band. This distribution of points is the first indication of problems encountered with the simulation, as such a broad band would not be expected compared to other simulated data. Albeit hardly visible due to the overlap of the data points, the α -band can be divided in two distinct populations: a broader band and a sharp line-like band within the former. The broadly distributed population originates from surface effects, which is made obvious by redoing the simulation of α -particles, letting them start inside the target crystal. The result is shown in Fig. 7.5, where only the sharp line, which could be detected in the previous plot, is existing, but the other distribution of data points is gone. One can understand these outcomes by describing the procedure of an alpha hitting the surface of the material. The alpha has a high cross section for interactions within the target, thus its mean free path is low and processes close to the surface will happen. If the alpha enters and is scattered in specific angles, the particle may leave the detector volume again. Hence, it only deposits part of its energy in the material in these events. This leads to a dis-

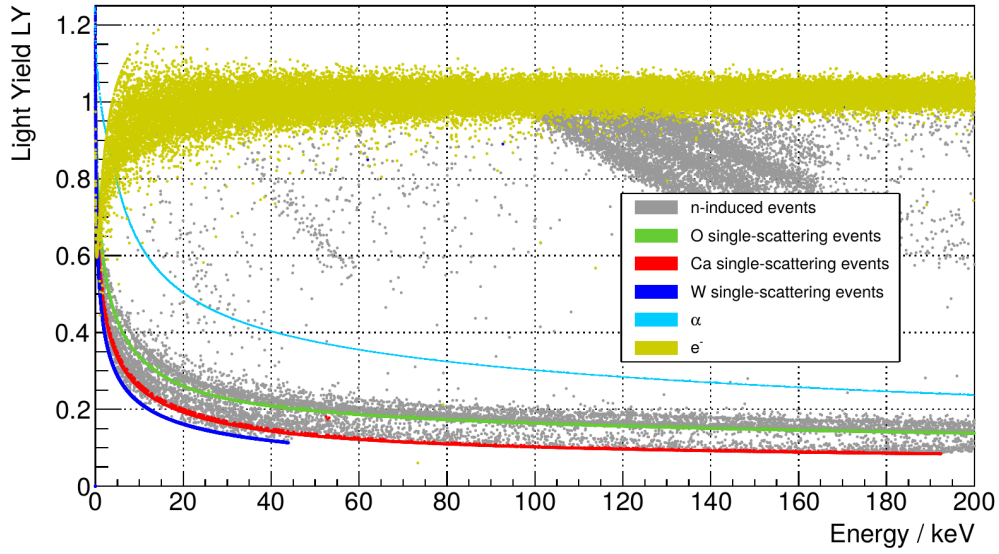


Figure 7.5.: This graphic is equivalent to Fig. 7.4, except for the fact that α -particles are started inside the target crystal. This leads to a single, light-blue line representing their data and shows that the points distributed around this line originate from surface effects.

tribution of points at different LY values for the same deposited energy, because alphas with diverse kinetic energies may deposit the same amount of energy, while their stopping power is different. The deposition of the whole particle energy in the detector leads to the sharp line which can be seen in the graphics. From basic considerations, one would expect that this full-absorption-line poses an upper limit on the whole population of events. The decreasing LY towards higher energies should lead to data points only below this line for α -particles which only deposit part of their energy. However, this is obviously not the case in our simulation, indicating a further issue. Besides this, a short comparison of the LY as a function of the deposited energy to the expected behavior is sufficient to recognize that the simulated data widely deviate from the experimentally obtained characteristic. A QF slightly above 0.2 increasing up to a value between 0.35 and 0.4 at lowest energies would be expected [22]. The plot of our simulated data, however, shows a faster increase leading to a very steep rise below ~ 20 keV, so that LY values even exceeding the ones of electrons are generated. A similar deviation of slope and offset is observed for the nuclear recoil bands. Hence, possible solutions will be discussed together after we describe the neutron simulation.

Neutron-induced events in the LY - energy plane shown in Fig. 7.4 and 7.5 are depicted in gray, green, red and blue. The distinction between these colors is as follows: Neutron single scattering events off an O, Ca or W nucleus are marked in green, red and blue, respectively, whereas gray denotes all other neutron-induced

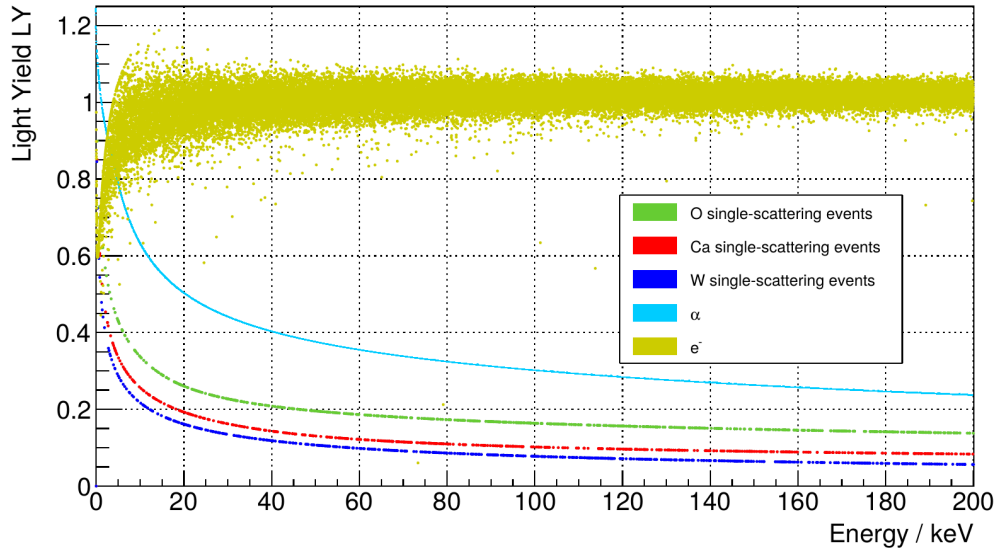


Figure 7.6.: The data in this plot are mainly equivalent to those depicted in Fig. 7.5. The difference is that only single scattering events are shown and that all bands extend across the entire energy region displayed.

scatterings, e.g. scatterings including multiple species of ions. At high LYs, the features due to inelastic neutron scattering, where the main part of the energy deposition happens through electromagnetic cascades (an example of such a reaction is given in the lower part of the cascade depicted in Fig. 5.1), can nicely be seen. Bands in this regime like the gray ones obtained between ~ 100 and 180 keV are expected. The gray data points close to the colored single scattering bands, on the other hand, originate from multiple neutron scattering. All possible combinations of scatterings can occur with arbitrary multiplicities leading to points at all possible values between the single scattering lines. However, for the analysis in this thesis, we will focus on the single scattering events to compare to the experimentally found mean LYs of the nuclear recoils. The behavior of these can already from Fig. 7.4 and 7.5 adjudicated to be erroneous, similar to the one of α -particles discussed previously. For better comparability to plots in the following sections and to experimental data, a graphic only containing the single scattering events is depicted in Fig. 7.6.

As the focus of this work is set on the nuclear recoils, a closer look at their QFs with a direct comparison to the phenomenological functions derived from the experiment (cf. Fig. 6.3) is displayed in Fig. 7.7. The energy range in this plot is adapted to the one in the reference ranging up to 600 keV. Only single scattering events are shown. Therefore, the time-saving simulation method, starting the O, Ca and W ions in the material directly instead of shooting neutrons of a few tens of MeV initially to create the recoils, has been chosen. Looking at Fig. 7.7 now,

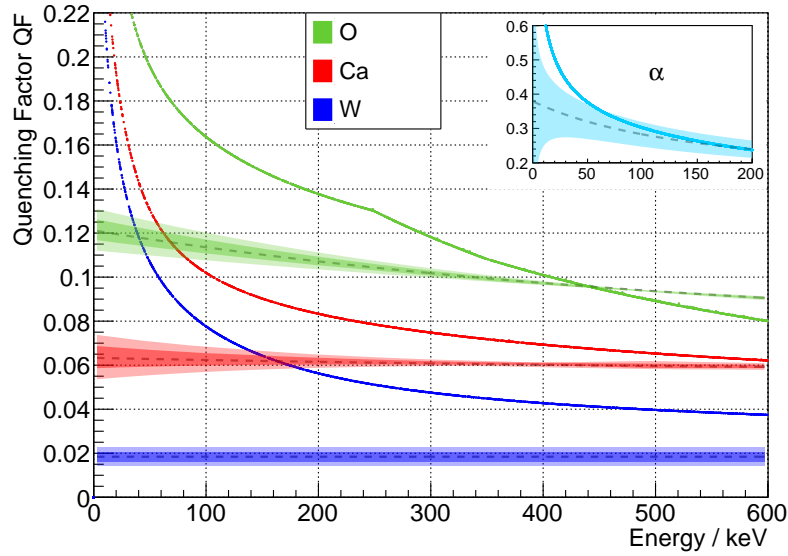


Figure 7.7.: A zoom at the QFs due to nuclear recoils is depicted for an energy range between 0 and 600 keV. The inset in the upper right part shows a similar depiction for α -particles. For comparison, experimental curves are represented by the dashed lines (mean values) and shaded areas (1σ and 2σ error bounds, cf. Fig. 6.3 for nuclear recoils and Fig. 3.2 for alphas). The obtained QFs in the simulations and the strange kink visible for O at ~ 250 keV point out that there are issues using default Geant4 settings. Variation of the data points are smaller than the line width.

some issues are clearly visible. Compared to the experimental curves, which are represented by the dashed lines (mean values) and shaded areas (1σ and 2σ error bounds), the slopes of the simulated QFs is by far too steep. This is especially the case for low energies, which are of highest interest to us, as in the CRESST experiment, the region of interest for dark matter induced nuclear recoils is in the order of a few up to a few tens of keV. The simulation strongly overestimates the QF in this region. Even for higher energies, the QF values and gradients of the curves do not match. In addition, the QF of oxygen shows a strange kink at roughly 250 keV, which has to be a simulation artifact, for example originating from a sudden change of the stopping power model without a smooth transition. The way the QF is calculated via Birks' law, a smooth stopping power function would otherwise lead to a smooth QF curve.

The inset in the upper right part of Fig. 7.7 additionally shows the comparison of the simulation to the experiment for α -particles. Reference data for the dashed line and shaded area are taken from Ref. [22]. Similar to the behavior of the nuclear

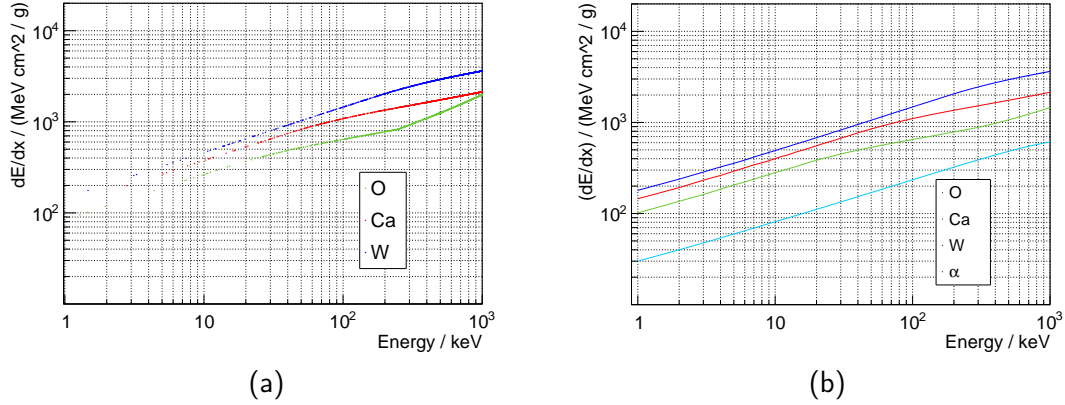


Figure 7.8.: For comparison, the total stopping powers within CaWO_4 obtained in the simulation with default settings are depicted in the left plot (a), while the electronic stopping power, that is tabulated in Geant4, is shown in the right graphic (b). It can clearly be seen, that only electronic stopping is invoked in the simulations, at least at low energies.

recoil bands, the simulated alpha band rises too steeply towards low energies.

Problem Sources and Solutions

Analyzing the issues described above, one striking malfunction in the simulation can be detected. The way that step sizes are determined does not work as desired for low-energetic ions and α -particles. This does not mean that the method is wrong in general, but that it has been designed for higher energies. Its procedure can shortly be explained as follows: Each possible process (discrete or continuous) proposes a step length based on its cross section in a Monte Carlo approach. The smallest of these physical step lengths will be invoked. If it is longer than the distance to the next volume boundary (geometric step length), a recalculation imposing the geometric step length is conducted.

For low energies and especially for highly ionizing particles, the problem is that the determined step lengths are longer than the so-called 'final range', which sets the maximum distance a particle with a certain energy may travel within a distinct material. Thus, the ions and also the α -particles are stopped in a single step, leading to incorrect stopping calculations. As described in section 7.1, different interactions are called one after another. First, electronic stopping is invoked, which in this case stops the particle and deposits the whole energy according to the electronic stopping power. Thereafter, the nuclear stopping process cannot be invoked any more, hence not taking into account its large contribution to the total stopping power. This can be seen from Fig. 7.8, where the stopping power, that could be extracted from the

```

event #5: (1 Tracks)
Primary Track: alpha
Start Status: Ekin = 43.5352 keV   in Volume: World
End Status:   Ekin = 0 keV         in Volume: Cube
# Hits: 6      | Step Lengths | Energy Deposits |
                | 0.000111231 mm | 13.0554 keV      |
                | 0.000114781 mm | 1.71117 keV      |
                | 0.000114781 mm | 5.15021 keV      |
                | 0.000114781 mm | 15.4418 keV      |
                | 0.000114781 mm | 1.14127 keV      |
                | 0.000152291 mm | 7.03542 keV      |
# Secondary Tracks: 0

```

Figure 7.9.: An example of the stepping data of a simulated alpha event with standard Geant4 settings, showing that the step length stays the same for some consecutive steps.

simulated data (a) is compared to the tabulated electronic stopping powers used in Geant4 (b). By eye, a very good agreement between these can be seen, specifically for low energies. Only for oxygen at an energy above ~ 250 keV, a deviation is detectable, which was already visible in Fig. 7.7 as a strange kink in the QF graph. In the course of the simulation, no fluctuations of energy losses are applied, as this would be done on a step-by-step basis, which does not work with only a single step, in which the whole energy is deposited. Hence, when doing simulations with extended models, in the next sections, we will show results without energy loss fluctuations first for better comparison.

It turns out that issues with the step size are also the cause for the previously described problem with the α -band. The simulation results showed a broad band in the LY - energy plane with unphysical events above the line of full energy deposition. Looking at step lengths and energy depositions, it can be seen that distances for ~ 2 -6 consecutive steps are often exactly the same, while the energy depositions in these steps show large variations. An example of this behavior is shown in Fig. 7.9. Albeit the origin of this miscalculation is unknown, we found a solution.

A user-defined maximum step length can be set with the help of a class called 'G4StepLimiter'. An appropriate value leads to a higher number of steps for each event. Thus, nuclear stopping is invoked and a higher precision for the calculation of the LY, for which we use the sum approximation (Eq. (5.3)) instead of the integral (Eq. (5.2)), inserting the light outputs calculated with Birks' law, can be achieved. The details and results are given in the next section.

7.4. Standard Geant4 with Step Limitation

In order to get rid of the main issue found with the simulations using default Geant4 settings, a maximum step size has to be employed in the code.

Adaptation of the Physics List

There are classes and physics lists provided by Geant4, which can be used to limit the step size. The physics list is called `G4StepLimiterPhysics` and can be registered in the main physics list `PhysicsList.cc` which by itself calls sub-lists dedicated to certain interactions, e.g. it calls `G4EmStandardPhysics_option4` to implement electromagnetic interactions. If processes are, however, registered in the main list, they are applied to all particles. As we do not need a step limitation for electrons and gammas, a different approach was chosen. Within the electromagnetic physics list, the class `G4StepLimiter` can be used to activate the limitation for the desired particles. Thus, an adapted class, which we named `EmStandardPhysics_option5`, has been written and the process has been activated for alphas and ions only.

The desired step length has to be set for each material in the geometry. In our case this is only CaWO_4 . For the vacuum, defined around the detector in the simulation, no step limitation is needed. The maximum step size has to be assigned to the so-called logical volume, i.e. the volume managing all properties and information about the detector part, not taking into account its position, in the file defining the CaWO_4 cube. An appropriate value for the maximum step size was found to be 1 nm. However, it has to be mentioned, that small changes of the step limit hardly change the results at this point.

Simulation and Results

The same configuration of Geant4 was used as described in section 7.1 with the exception of the modifications stated above. In addition, an explicit command is now added to disable energy loss fluctuations in the simulations for the better comparison to previous results. For the same reason, we focus again on single scattering events. Hence, as before, we start the recoiling ions directly in the crystal. However, alphas are still started outside. The features due to multiple and inelastic neutron scattering are therefore missing in the depiction in Fig. 7.10 of the simulated data.

Looking at this plot, except for the electron band, which has not altered, because it is not affected by the applied modifications, some changes are obvious at first sight. All the other LY curves are notably shifted to lower values and show different features than before.

For α -particles, the line indicating deposition of the total initial kinetic energy in the detector is clearly visible. Its slope towards lowest energies is not as steep as before (cf. Fig. 7.6). Still, the values are too high compared to the experiment, which indicates a LY slightly above 0.2 at 200 keV and a raise towards a value close

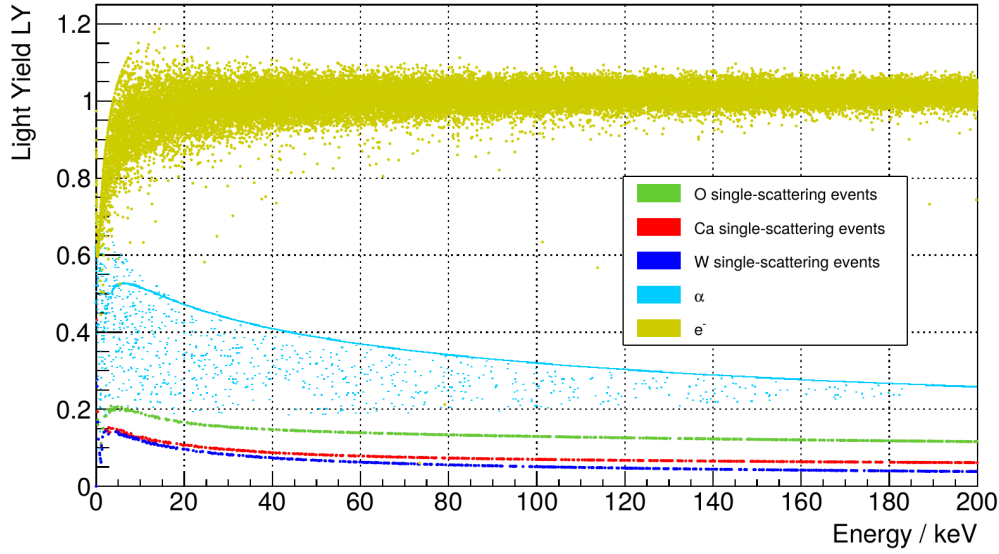


Figure 7.10.: The LYs, obtained after introducing a maximum step size of 1 nm within the CaWO_4 target crystal, are depicted. Except for this adaptation, the Geant4 settings are left unchanged. The color code in this graphic is the same as in Fig. 7.6 and a detailed comparison to said figure is given in the text.

to 0.4 at the lowest depicted energies. However, a significant improvement can also be seen in the physical meaningfulness of the data. Contrary to the result obtained with the default Geant4 settings, no data points are found above the line of total energy deposition for energies above ~ 10 keV. Below this energy, the simulation still seems to have problems calculating the correct energy depositions, especially in the final step of an event, in which the particle is stopped. This leads to a reduction of the LY at very low energy as depicted in the graphic and to some data points that therefore lie above the sharp line. If the simulation is conducted with α -particles starting inside the CaWO_4 cube, all the points that do not lie on the line disappear again, as shown in Fig. 7.11.

The nuclear recoil bands are also clearly seen at lower LY values than with default Geant4 settings. An improvement is especially indicated by the obtained limited values at low energies compared to the very steep rise towards high LYs in Fig. 7.6. However, having a closer look at the nuclear recoils and comparing their QFs to the experimental ones, as done in Fig. 7.12, enables a more detailed analysis. In this plot, the dashed lines (mean values) and shaded areas (1σ and 2σ error bounds, cf. Fig. 6.3 for nuclear recoils and Fig. 3.2 for alphas) represent the experimental observations, while the full lines are the simulated curves. When comparing with Fig. 7.7, we see, that the kink in the O band is gone. Furthermore, the QF values have generally improved, featuring lower values. However, they are still far off

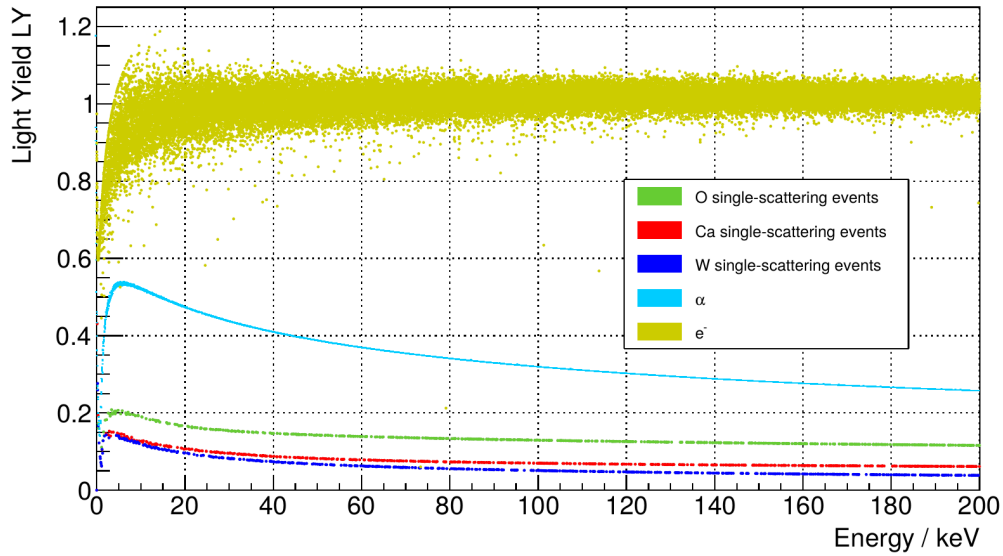


Figure 7.11.: This graphic is equivalent to Fig. 7.10, except that alphas were started inside the target material. Therefore the light-blue data points below the line, which originated from surface effects, vanished.

from the expected ones and also the gradients of the curves still do not match the experimental data. The largest discrepancies can be obtained at low energies.

Possible Extensions to this Model

Of course, to some extent the slopes at low energies originate from using the Birks equation (Eq. (3.1)) to calculate the light output and LY. The formalism might not be fully adequate at the lowest energies, where the denominator naturally leads to a rather steep rise. However, it obviously always depends on the stopping powers of the particles. As discussed in section 7.3, when describing the important classes for simulating the stopping process, tabulated values adopted from ICRU publications are used by default in Geant4. There are other sources for stopping power data, of which at least one is widely used, namely SRIM (Stopping and Range of Ions in Matter) [37]. Implementing this alternative set of stopping powers in the Geant4 code can be done in order to gain an expertise about which of the data may reproduce the experimental results more precisely. This will be the topic of the next section.

A further extension to the model presented in this section would naturally come from activating the energy loss fluctuations. The effect of these fluctuations and the obtained results will be discussed in section 7.8.

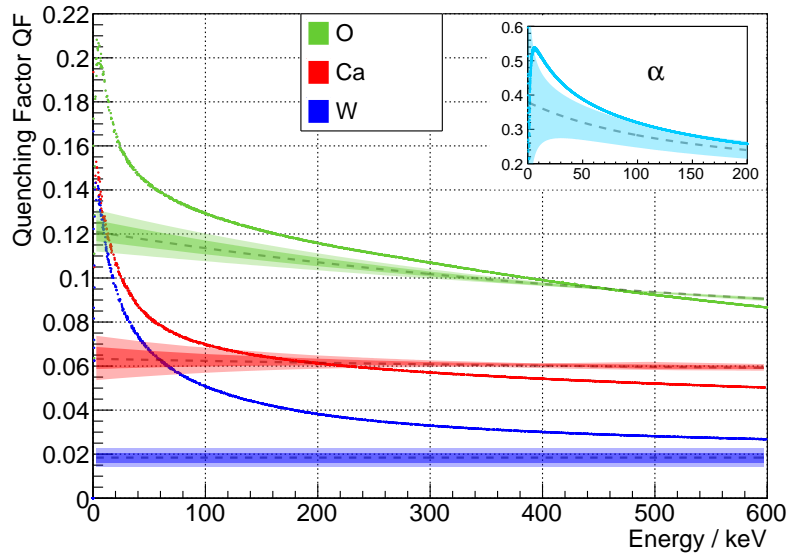


Figure 7.12.: Comparison between the QFs of nuclear recoils, obtained in simulations using standard Geant4 settings with the addition of a manually set step limit of 1 nm (full lines), to the experimental data, given by the dashed lines (mean values) and shaded areas (1σ and 2σ error bounds, cf. Fig. 6.3 for nuclear recoils and Fig. 3.2 for alphas).

7.5. SRIM Stopping Powers and Step Limit

This section deals with introducing a different set of tabulated stopping powers to the Geant4 code. The data are adopted from SRIM and shall be compared to the other prominent source for data of ion stopping powers provided by the ICRU to find the data set that reproduces the experimental results with higher accuracy.

Making SRIM Stopping Powers available to Geant4

In order to be able to use the SRIM stopping power data in the simulations, tables have to be extracted from the SRIM website [42] and added to the code repository in Geant4-readable format. On the website, interactive tools for obtaining electronic and nuclear stopping power data, separately, are available. An incident particle has to be chosen, a user defined material can be selected and a minimum and maximum energy of interest have to be stated. In our case, CaWO_4 is the target and incident particles are He (i.e. α -particle), O, Ca and W. In Fig. 7.13, the obtained total stopping powers are depicted in the left graphic (a). The right plot (b) shows the electronic and nuclear stopping powers separately, for the example of

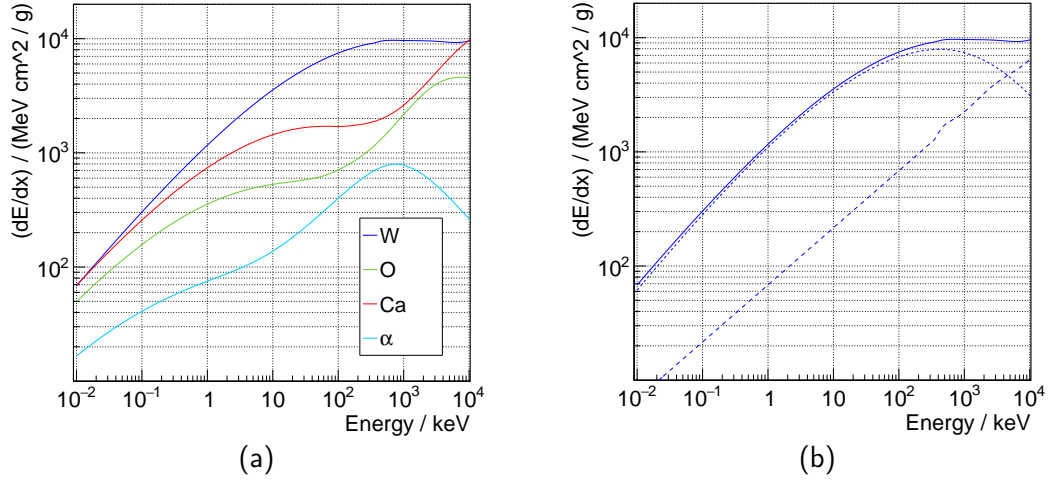


Figure 7.13.: SRIM stopping powers: (a) Total stopping powers of α -particles and O, Ca and W ions in CaWO_4 . (b) Total stopping power split into electronic (large dashes) and nuclear (short dashes) stopping powers for the example of W.

W. The smaller-dashed curve, dominating the total stopping power at low energies, represents the nuclear stopping. For lighter particles, the energy at which nuclear stopping exceeds electronic stopping, is lower. In the following, we will discuss how the SRIM data can be fed to the simulations.

The implementation of the SRIM stopping powers follows the standard implementation of the ICRU stopping powers in the `G4IonParametrisedLossModel` as described in section 7.1. The tables obtained from the SRIM website are copied to a text file after converting energy as well as stopping power values to the correct units of MeV per nucleon and MeV cm²/mg. The energy range can be chosen freely on the SRIM website. Hence, a minimum of 10^{-5} MeV and maximum of 100 MeV are considered, which obviously translate into different energies per nucleon for each nucleus, as these numbers are therefore divided by the respective mass number. Our SRIM tables have 127 entries in the selected energy range. To make the SRIM data readable for Geant4 we follow the format and file name specification as given in section 7.1. As the name of the target material is `CRESST_CaWO4`, the file for oxygen is called `'z8_CRESST_CaWO4.dat'`, for example. Those for alphas, calcium and tungsten start with `z2`, `z20` and `z74` respectively.

Two new sub-folders are added to the `'ion_stopping_data'` in the Geant4 data repository `G4EMLOW6.48`. One contains electronic and one nuclear stopping data. Therefore, they are called `'srim_electronic_stopping'` and `'srim_nuclear_stopping'`. While the application of the nuclear stopping powers needs further adaptations, which will be discussed below, the electronic stopping powers are ready to be used

in the simulations.

In our `EmStandardPhysics_option5` physics list, an option is added for the particle names 'alpha' and 'GenericIon' that uses the `G4IonParametrisedLossModel` for the ion ionization process, adding the command `AddDEDXTable(name, source folder, scaling)`. For the purpose of applying the SRIM electronic stopping powers, the source folder is set to 'ion_stopping_power/srim_electronic_stopping'. The scaling then has to be left blank, because the ICRU scaling option cannot be applied. The respective source code can be found in appendix B.

As we also want to use the SRIM data for alphas, a further adaptation has to be made. By default, the `G4IonParametrisedLossModel` only works for nuclei with an atomic number of $Z = 3$ or greater. Thus, we adapt the code to our own `IonParametrisedLossModel`, where the minimum atomic number is changed to $Z = 2$ in the initialisation method. After these changes, SRIM electronic stopping powers can be used in the simulation for all desired particles (α , O, Ca, W).

However, for nuclear stopping the implementation is more difficult. The standard Geant4 class dealing with it is `G4NuclearStopping`, of which a short description is given in the list at the beginning of section 7.1. This class does not access external data tables, but makes use of an ICRU model contained in the class `G4ICRU49NuclearStoppingModel`. There, stopping powers are calculated via an analytic formula, which incorporates tabulated data. However, these data are internally available in a method of the class itself. The model that we want to implement for nuclear stopping should, however, work equivalent to the electronic stopping power model, utilizing data from an external table, without the need of applying an additional formula. Thus, based on the `IonParametrizedLossModel`, we develop a nuclear stopping model, which we call `SRIMNuclearStoppingModel`. Some dispensable methods are deleted for this model and availability for alphas, like in the electronic stopping model, is ensured. Other than that, there are only a few but still essential adaptations to be made. In the constructor, the corresponding tables are added via `AddDEDXTable("SRIMNuclearStopping", new G4IonStoppingData("ion_stopping_data/srim_nuclear_stopping"))` and the quantity called 'energyLossLimit' is changed from 0.01 to 1. If the energy loss in a step is larger than the kinetic energy of the particle multiplied by this latter value, the calculation is usually refined to guarantee high accuracy. However, this method is written for electronic stopping and can hardly be adapted to nuclear stopping. Thus, a value of 1 is chosen, so that the tabulated values are always directly employed. Of course, a small step size has to be used, in order to keep the energy loss per step low compared to the kinetic energy without having to apply a refinement via the 'energyLossLimit' exception, hence still achieving high accuracy at low energies.

In addition, a class very similar to the standard `G4NuclearStopping` is written,

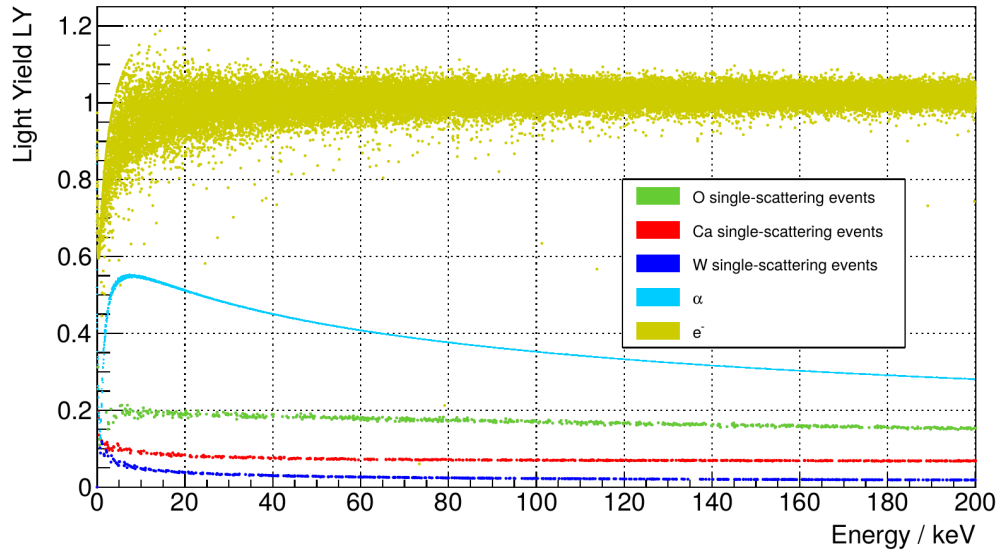


Figure 7.14.: This figure shows the resulting plot in the LY - energy plane of a simulation using SRIM stopping powers for α -particles and O, Ca and W ions in a CaWO_4 crystal. Again, a step limit of 1 nm has been applied.

which is able to call the `SRIMNuclearStoppingModel` class and its method responsible for calculating the energy loss due to nuclear stopping. The source code of this new `NuclearStoppingSRIM` class is almost the same as the one of the default Geant4 class it is based on, except for adding the SRIM model in its initialisation method and using the corresponding `ComputeDEDXPerVolume` function in its `AlongStepDoIt` method. In order to make the SRIM nuclear stopping powers accessible in the simulations, this class now has to be instantiated in the physics list `G4EmStandardPhysics_option5` and registered for particles 'alpha' and 'GenericIon'.

Simulation and Results

With the help of the data tables added to the code repository and the new and adapted source files and classes discussed in the previous subsection, the simulations can be rerun with the utilization of SRIM stopping powers instead of the default ICRU stopping powers. Besides these adaptations, energy loss fluctuations are again ignored for the sake of better comparability of the models. The step limit of 1 nm is kept unchanged, because it leads to a sufficient amount of steps in the course of the simulated stopping process to ascertain precise results using the tabulated stopping power data and building the sum of light outputs due to Birks' law instead of integrating the equation.

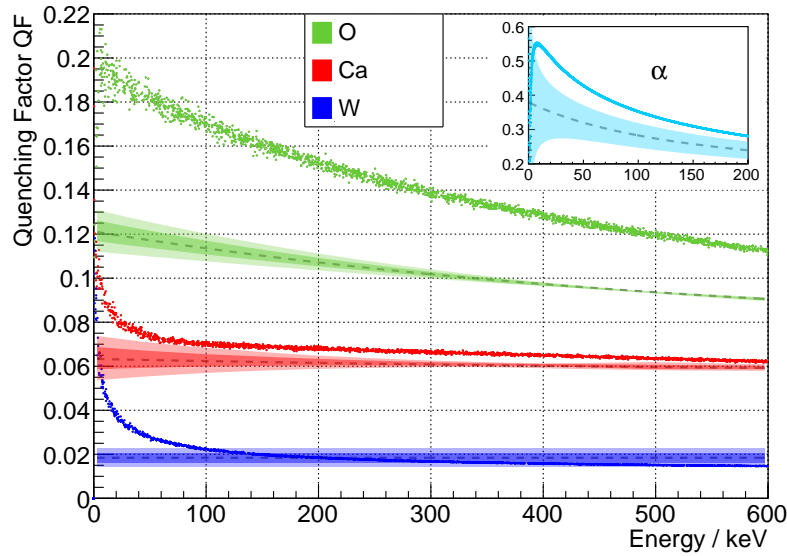


Figure 7.15.: A zoom on the QFs of nuclear recoils is presented for the simulations using SRIM stopping powers and a step limit of 1 nm. The dashed lines (mean values) and shaded areas (1σ and 2σ error bounds, cf. Fig. 6.3 for nuclear recoils and Fig. 3.2 for alphas) represent the experimental results.

The resulting plot is shown in Fig. 7.14. As before, only the single scattering events are depicted. Furthermore, α -particles are started inside the detector to only observe the line of total energy deposition. Looking at this plot now, already some differences can be obtained in comparison to the simulations conducted in the previous section (cf. Fig. 7.11).

The LY of alphas (light blue) is slightly higher using the tabulated SRIM stopping powers than with the default Geant4 ion ionization model (remember, that no parametrized model was available for the electronic stopping of alphas in standard Geant4). However, the shape of the curves are very similar.

Looking at the nuclear recoil bands, one can at least see that tungsten events (blue) are further separated from calcium events (red) than with the ICRU model and that the tungsten events are at lower LYs, while oxygen events (green) are at higher LYs. A closer look at the nuclear recoil bands, shown in Fig. 7.15, can be used for a more detailed analysis. The dashed lines (mean values) and shaded areas (1σ and 2σ error bounds, cf. Fig. 6.3 for nuclear recoils and Fig. 3.2 for alphas) in this graphic represent the experimental results again. For Ca and W, steep slopes at low energies are still visible with the SRIM model. However, for higher energies, the gradients of all the QF curves are in rather good agreement with the experimental ones. Also, the absolute values are not too far off, except for the ones

of oxygen. However, improvements will be seen in section 7.8, discussing the effects of energy loss fluctuations on the results.

Conclusion on the SRIM Model

All in all, the SRIM stopping powers seem to describe the experimental data better than the default Geant4 model based on ICRU stopping powers. The QFs are much more stable towards lower energies. This means, the behavior and shape of the data is in better agreement with the experiment. Only the unrealistic slopes at low energies are still existent with this model, though highly reduced compared to the standard Geant4 model. Also, absolute values of oxygen QFs do not match the experiment very well. This issue will be partly resolved in section 7.8, however, when energy loss fluctuations are taken into account.

7.6. G4ScreenedNuclearRecoil Class

A further model, which is investigated within this thesis, uses a different approach for the nuclear stopping power. This model is included in the Geant4 distribution in example TestEm7, but not in the main code. It is incorporated in a file named `G4ScreenedNuclearRecoil`, which already points to the method that is used. The nuclear recoils are modeled with a screened interatomic potential function. Therefore, this class is said to provide more accurate results than the default model and SRIM simulations [43]. In the following, an explanation of its functionality is given.

Class Description, Functionality and Implementation

`G4ScreenedNuclearRecoil` is written for the purpose of adequately simulating nuclear recoils taking into account the screening of the interatomic potential due to the electrons around the target nucleus. It therefore extends the default nuclear stopping model and is additionally said to use SRIM nuclear stopping powers instead of the ones published by the ICRU. A detailed discussion of the class is given in Ref. [43]. The main features are listed here:

- The screened interatomic potential function,

$$V(r) = \frac{Z_1 Z_2 e^2}{r} \Phi\left(\frac{r}{a}\right) \quad , \quad (7.2)$$

is used, where Z_1 and Z_2 are the atomic numbers of the projectile and the target, e is the electron charge, $\Phi(\frac{r}{a})$ is the screening function, r is the inter-nuclear separation and a is the characteristic screening length.

- Three different screening functions are available by default, which are Ziegler-Biersack-Littmark ("zbl"), Lens-Jensen ("lj") and Moliere ("mol") screening. Further functions could be manually added.
- The scattering integral,

$$\theta_c = \pi - 2\beta \int_{x_0}^{\infty} f(z) dz/z^2 \quad , \quad (7.3)$$

is solved explicitly for the reduced impact parameter $\beta = b/a$ and the reduced center-of-mass energy $\epsilon = E_c a / (Z_1 Z_2 e^2)$ contained in the function $f(z)$, which reads

$$f(z) = \left(1 - \frac{\Phi(z)}{z \epsilon} - \frac{\beta^2}{z^2} \right)^{-1/2} . \quad (7.4)$$

- SRIM data of nuclear stopping powers are used.
- Nuclear recoiling secondaries are implemented. This means that an incident nuclear recoil can itself lead to nuclear recoils, creating secondary tracks and therefore leading to a recoil cascade. This is not possible in the standard Geant4 implementation of nuclear stopping. There, no production of secondary tracks is included, but only the energy loss along the track of the primary recoiling nucleus is followed.

In the implementation of this method to the Geant4 code, some public variables of the ScreenedNuclearRecoil class, which are set in the constructor, are highly significant and can be changed by the user. They are important for the physics happening in the process and are described as follows:

- *ScreeningKey*: is a string variable, which denotes the screening function that shall be used in the simulation, therefore leading to the generation of the desired screening tables and cross sections. By default, it is set to "zbl".
- *GenerateRecoils*: is a Boolean variable, which defines, if secondary recoil nuclei should be generated and tracked. The default value is 1. If it is changed to 0, the energy is locally deposited, instead of allocating it to a secondary recoiling nucleus.
- *RecoilCutoff*: is a double variable denoting the energy per nucleon, below which no further secondary recoil will be generated, even if *GenerateRecoils* is set to 1. Furthermore, all particles with an energy per nucleon below the given value are stopped and do not further interact. They only deposit their remaining energy. The cut is set to 100 eV by default.
- *PhysicsCutoff*: is a double variable setting an energy cut for the calculation of the scattering cross section. Forward multiple scattering needs a lower cut

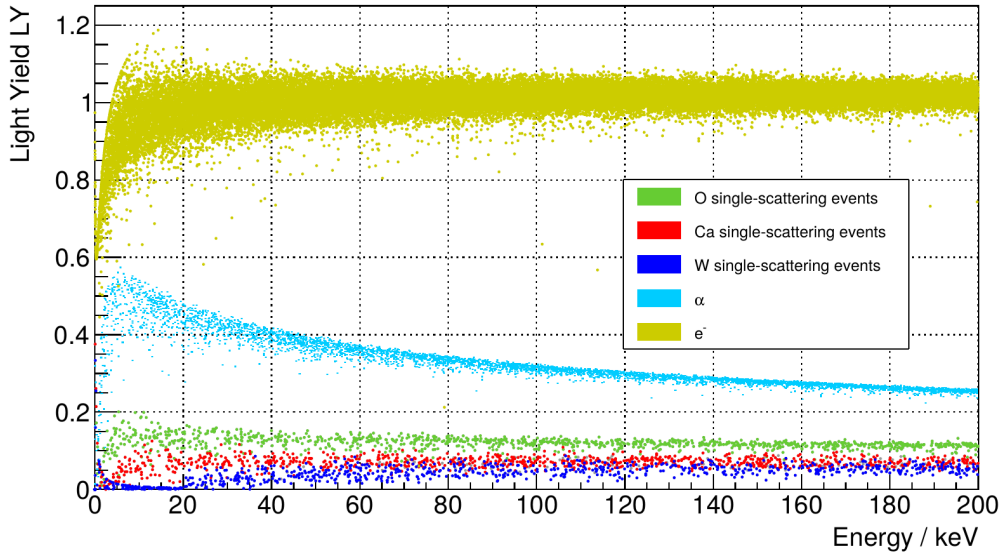


Figure 7.16.: LYs within CaWO_4 , when conducting a simulation using the screened nuclear recoil model with default parameter values and an additionally applied step limit of 1 nm are depicted in the LY - energy plane.

value than backscattering. However, the header file of this class tells that there is usually no reason to change this parameter from its default value of 10 eV and the article [43] states that a change should not have a strong influence on the results.

After instantiating the `G4ScreenedNuclearRecoil` class in our physics list and registering it for alpha particles and ions, simulations can be conducted.

Simulation with default Settings

Again, the same configuration as described in section 7.1 is used, except for registering the `G4ScreenedNuclearRecoil` class for nuclear stopping in the electromagnetic physics list. The resulting LY plot is depicted in Fig. 7.16. The color coding is the same as before, where alpha events are shown in light-blue, O in green, Ca in red and W in blue.

The LY of α -particles has not changed drastically, which is expected, because alpha particles do not lead to a lot of nuclear recoiling secondaries above the cut energy defined by the *RecoilCutoff* parameter. The band is only broadened slightly towards lower LYs, because the secondary recoils all have a lower LY than the incident alphas.

The nuclear recoil bands of O, Ca and W, however, show some strange features. All of the LYs drop at some point, approaching low energies. Especially for W, this

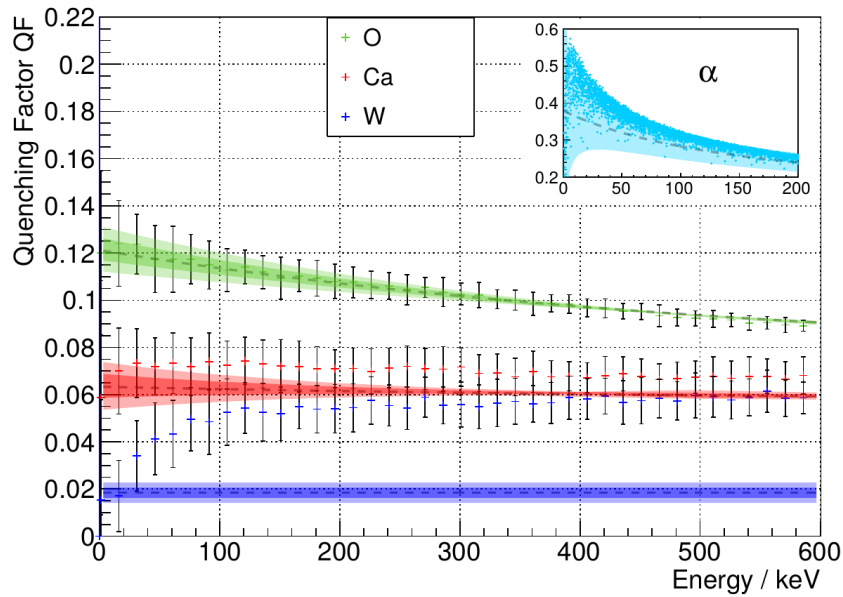


Figure 7.17.: A zoom on the QFs of nuclear recoils is presented for the simulations using the screened nuclear recoil model, with default values of its adjustable parameters, and a step limit of 1 nm. The dashed lines (mean values) and shaded areas (1σ and 2σ error bounds, cf. Fig. 6.3 for nuclear recoils and Fig. 3.2 for alphas) represent the experimental results.

behavior is strongly pronounced. It is clearly visible that its LY jumps to values close to zero below 20 keV. A further issue is, however, that its LY rises to values similar to those of Ca for higher energies. Because of the distribution of data points overlapping at least for the two nuclei mentioned, a different representation is used when zooming in on the nuclear recoils. Mean values with error bars are shown, as done in Fig. 7.17, while the dashed lines (mean values) and shaded areas (1σ and 2σ error bounds, cf. Fig. 6.3 for nuclear recoils and Fig. 3.2 for alphas) are the experimental results. Due to the wider energy region and the applied bin width, the behavior at low energies is not as obvious as in the full LY plot. Still, some issues can be identified. Except for the oxygen QF, which quite nicely follows the experimental curve, there are problems with the data. The QF of Ca is a little too high, almost across the whole region, and the QF of W, as already mentioned, rises with increasing energies until it almost approaches the values obtained for Ca.

Problem Sources and possible Solution

Analysing the tracking data of the simulations, one can see that particle cascades are created, which mostly consist of O, because of two reasons. First, O makes up

for 2/3 of all atoms in CaWO_4 and second, lower energetic recoils can be generated compared to those of heavier nuclei, because its energy per nucleon may rather be above the *RecoilCutoff*. As the secondary particles obviously also contribute to the LY of the initial nuclear recoil, the higher value for O affects the LY of Ca and W. This is the reason for the shift towards higher values, most pronounced for W. As a possible solution, a larger *RecoilCutoff* could be chosen, leading to a lower amount of secondary particles and therefore to a less distinct shift of the LY values.

However, the *RecoilCutoff* also plays a role in the second issue found for very low energies, where the LY drops down almost to zero. The reason for this behavior is, that the cutoff also defines the energy per nucleon below which a particle is stopped within a single step. If the step is rather small in relation to the remaining energy, which is deposited in this last step, a very high local energy deposition (dE/dx) is attained. Calculating the light output and respectively the LY with the help of Birks' law, Eq. (3.1), this results in a value close to zero. A *RecoilCutoff* of 100 eV per nucleon, for example, translates to a kinetic energy of $\sim 18,4$ keV for W, which is exactly the value at which the drop can be seen in the plot of Fig. 7.16. To resolve this issue, a lower value of the *RecoilCutoff* would be needed.

Thus, the two problems might be solved by the exact opposite measure. Obviously, a satisfying result therefore cannot be obtained. Adaptations are needed to resolve both issues at once.

7.7. Modification of *G4ScreenedNuclearRecoil*

The standard screened nuclear recoil class discussed in the previous section does not provide satisfying results. Modifications to its code are thus tested, trying to solve the obtained issues.

Code Modifications

As the *RecoilCutoff* has to be increased in order to solve the first and decreased to solve the second issue, the methods of the *G4ScreenedNuclearRecoil* class are adapted in a way that the cutoff is divided into two quantities. One of them is still called *RecoilCutoff*, but is now only used to determine the energy per nucleon, below which no further recoil particles are generated. The other is named *StoppingCutoff* and is replacing the *RecoilCutoff* at every position in the source code, at which it had been used to determine the energy per nucleon, below which a particle is stopped in a single step. Hence, with this adaptation of *G4ScreenedNuclearRecoil*, called *G4ScreenedNuclearRecoilMod*, the cut for stopping a particle can be set independently from the one for generating recoil tracks.

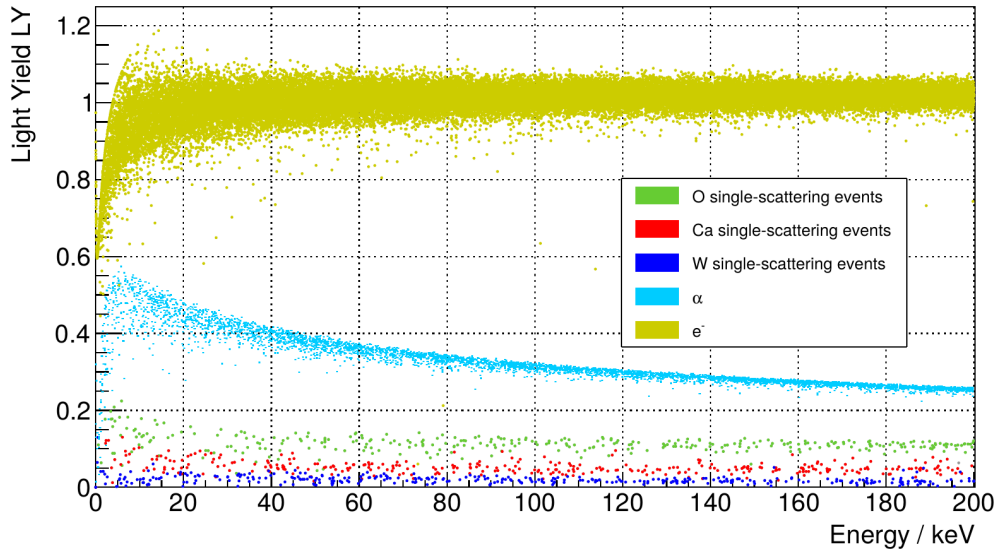


Figure 7.18.: Resulting LYs within CaWO_4 , when conducting a simulation using the modified screened nuclear recoil model with parameter values of 2,200 eV for the *RecoilCutoff* and 25 eV for the *StoppingCutoff*, additionally applying a step limit of 1 nm.

Results of the Simulations

Addressing the issues discussed in section 7.6, an increased *RecoilCutoff* and a decreased *StoppingCutoff* are chosen. The resulting LY plot is shown in Fig. 7.18, where values of 2,200 eV and 25 eV have been used for the cutoffs, respectively. These phenomenological values have been selected in the process of trying to find the best fit to the experimental data for W. A detailed look on the nuclear recoils with comparison to the experiment is presented in Fig. 7.19. As can be seen in the graphic, the results for W actually fit quite nicely, although a slight increase of QF values towards higher energies might be detectable. The simulations for O have only slightly changed, shifting the QFs towards lower values. However, the QF of Ca is clearly too low across the whole displayed energy region.

Hence, a further adaptation is tested. In order to prevent the QFs of W and Ca from rising at higher energies, the *RecoilCutoff* is made energy-dependent. In addition, to resolve the issue with the LY of Ca, a further dependence of this cutoff on the mass of the incident particle is introduced. Obviously, all of these adaptations are only of phenomenological nature, trying to adequately describe the experimental data. A linear dependence of the cutoff on the incident energy E_i and the mass A_1 via $\text{RecoilCutoff} = c_1 + c_2 \cdot E_i \cdot A_1$ with the constant values $c_1 = 500$ eV and $c_2 = 5.2 \cdot 10^{-5}$ leads to the results depicted in Fig. 7.20, providing a rather good fit to the dashed experimental curves. However, issues at very low energies

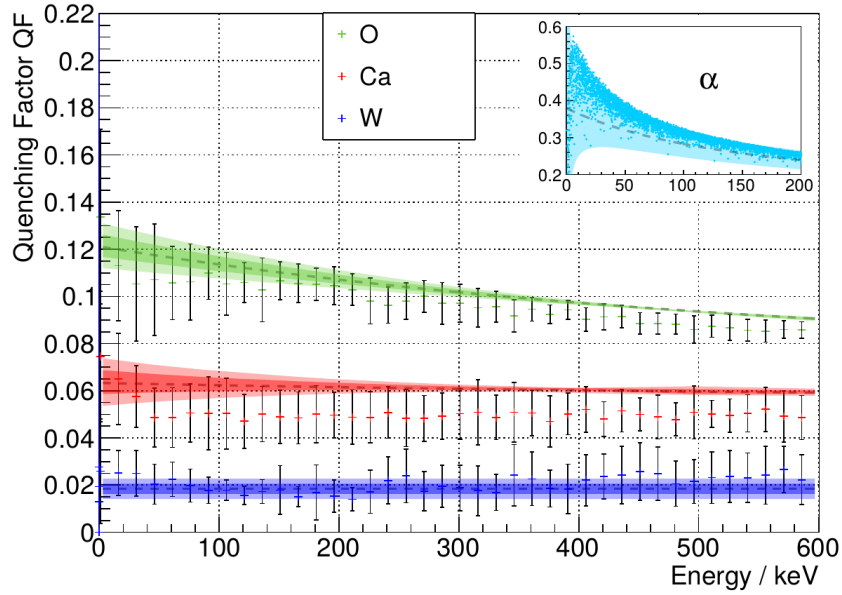


Figure 7.19.: The QFs of nuclear recoils are depicted, conducting simulations with the adapted screened nuclear recoil model. A *RecoilCutoff* of 2,200 eV and a *StoppingCutoff* of 25 eV are taken, together with a step limit of 1 nm. The dashed lines (mean values) and shaded areas (1σ and 2σ error bounds, cf. Fig. 6.3 for nuclear recoils and Fig. 3.2 for alphas) represent the experimental results.

will always persist.

Conclusion on the Screened Nuclear Recoil Model

The standard *G4ScreenedNuclearRecoil* model is said to describe the nuclear stopping more accurate than the standard Geant4 *G4NuclearStopping* model, as it solves the scattering integral explicitly and creates secondary recoiling nuclei. These facts sound very promising. However, from the beginning onward, the quantity called *RecoilCutoff* can be brought to question. One may ask, if there is a physical motivation behind defining an energy per nucleon, below which no recoil particle is generated. Naively, one might think that a minimum energy is needed to kick a nucleus from its lattice space, the so-called displacement energy, which in CaWO_4 is almost the same for every constituent, namely 28 eV for O and 25 eV for Ca and W [23]. Thus, it is not obvious, why the *RecoilCutoff* is set to 100 eV by default and multiplied by the mass number of the targeted nucleus to define the actual cut energy, below which no recoiling nucleus is generated. With this definition, the minimum recoil energy necessary to generate a recoiling W ion is much higher

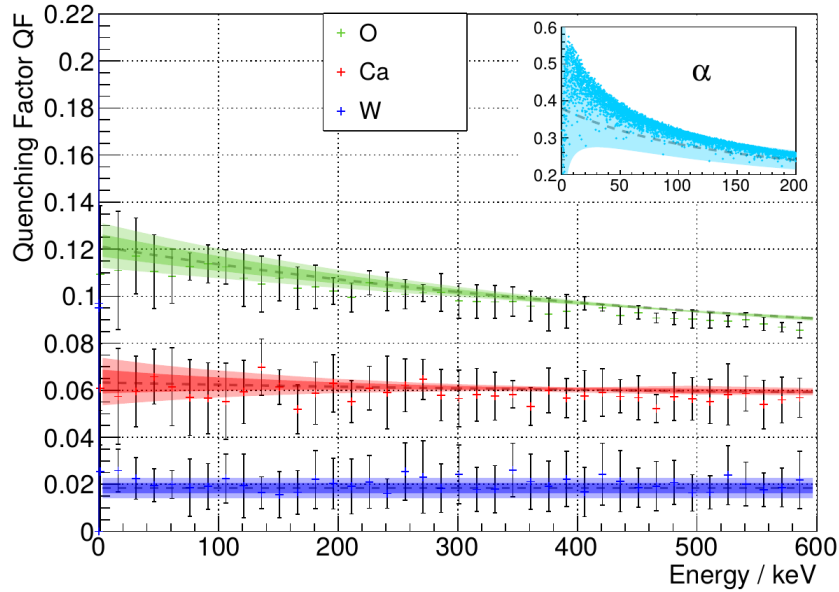


Figure 7.20.: QFs of nuclear recoils obtained in simulations with a further adaption of the screened nuclear recoil model are presented. The *StoppingCutoff* of 25 eV remains unchanged, but the *RecoilCutoff* has a linear dependence on the mass and energy of the incident particle. Details about the adaptation are given in the text. The dashed lines (mean values) and shaded areas (1σ and 2σ error bounds, cf. Fig. 6.3 for nuclear recoils and Fig. 3.2 for alphas) represent the experimental results.

than the energy needed to create a recoiling O ion, for example. The second effect of the *RecoilCutoff*, leading to the stopping of a particle below a certain energy, furthermore only seems like a phenomenological implementation done to improve simulation speed and to affect the results at low energies. Again, one may pose the question why this cutoff depends on the mass of the incident ion.

All in all, the standard `G4ScreenedNuclearRecoil` class seems to embody a phenomenological model proposing a parameter called *RecoilCutoff*, but lacking a motivation for this cutoff and its given value.

Due to the default value not yielding good results, adaptations have been tested in `G4ScreenedNuclearRecoilMod`, dividing the *RecoilCutoff* into two separate parameters, one controlling the generation of recoils and the other the stopping of particles. This phenomenological model could improve the results obtained with the default settings and produce LYs close to the experimental ones. However, this is not synonymous with being the best model for fitting the experimental data, as we will see, when energy fluctuations are taken into account in the following section.

7.8. Effect of Energy Loss Fluctuations

In sections 7.4 - 7.7, energy loss fluctuations have been turned off. This has been done due to the default Geant4 settings not accounting for energy loss fluctuations in the energy regime we are interested in. For better comparison of the different considered physical models that we implemented, the fluctuations have therefore been neglected in a first step, leading to a better understanding of how the various models change the obtained LY results.

Not taking into account energy loss fluctuations, however, is not a correct and physically meaningful behavior. Therefore, the fluctuations are included in a next step and their effects are the topic of the following discussions.

Dealing with Energy Loss Fluctuations in Geant4

The energy loss fluctuations of ions are treated by the method `SampleFluctuations` of the `G4IonFluctuations` class. Within this method, there are different options of applying variations to the mean energy loss along a step. These are chosen according to the mass of a particle, its kinetic energy, the mean energy loss, and the step length. Mainly, there are three options, which are applied in our simulations. In the first, fluctuations are sampled due to a Gaussian distribution, in the second, they are sampled due to a Gamma distribution, and in the third, a uniform distribution is applied. The Gaussian distribution is used, if the mean energy loss μ divided by the standard deviation σ , calculated by the `Dispersion` method of `G4IonFluctuations`, exceeds a certain value a . Thus, the model is chosen in cases, where the usual deviations are rather small compared to the mean energy loss. If this is not the case but the ratio is still bigger than a lower value b , i.e. $a \geq \mu/\sigma > b$, the Gamma distribution is applied. For even smaller ratios μ/σ , the uniform distribution is used.

As the standard deviation and the magnitude of fluctuations depends on the type of particle, its energy and also on the step length, different models may be applied for different incident particles in the simulations. In general, the fluctuations decrease for increasing particle mass, stopping power and step length. For lighter particles and small step sizes a larger fluctuation is expected. Still, the applied fluctuations may also vary with the chosen energy loss model, so that the effects for the same particle in the same energy region might not be similar in every case. This will be shown in the next subsection.

The different distributions used for modeling the fluctuations are affecting the shape of the LY bands. While the Gaussian distribution leads to a rather small variance of energy losses around the mean value, the Gamma distribution, depending on its parameters, can lead to large deviations. The shape parameter of the

distribution is small for the obtained energies and step lengths, often taking a value smaller than unity. In this case, the probability density of the distribution goes to infinity at zero and shows an exponential decrease towards higher values. This can lead to the feature that, in a lot of steps, a rather small energy deposition happens, while only in a few steps, a high amount of energy is deposited.

Effect of Fluctuations on the LY

Fluctuations lead to different energy depositions of the same particle with the same energy in different steps. Thus, the effective stopping power dE/dx varies as well. If sampled due to a Gamma distribution, the stopping power can be small in the majority of steps but very high in some other steps. The light output L and the light yield LY calculated with the help of Birks' law (Eq. (3.1)) are therefore affected. Based on summing up the light outputs of each step due to

$$L = \sum_i \Delta L_i = \sum_i \frac{S \cdot \left(\frac{\Delta E}{\Delta x}\right)_i}{1 + kB \cdot \left(\frac{\Delta E}{\Delta x}\right)_i} \cdot \Delta x_i \quad , \quad (7.5)$$

the impact of fluctuations is illustrated in the following example:

After limiting the step size, it usually takes a few hundred simulation steps for a single particle to be stopped. If we now, for example, look at 10 successive steps, where each has the same step length Δx , and consider an accumulated energy deposition E in these steps, we can compare two cases:

- Without energy loss fluctuations:
Across the 10 considered steps, an almost constant stopping power can be assumed. Hence, the energy loss in all 10 steps is the same and the light output, according to Eq. (7.5), is

$$L = 10 \cdot \Delta L = 10 \cdot \frac{S \cdot \frac{E/10}{\Delta x}}{1 + kB \cdot \frac{E/10}{\Delta x}} \cdot \Delta x = \frac{S \cdot E}{1 + kB \cdot \frac{E}{10 \cdot \Delta x}} \quad . \quad (7.6)$$

The LY is thus given by

$$LY = \frac{L}{E} = \frac{S}{1 + kB \cdot \frac{E}{10 \cdot \Delta x}} \quad . \quad (7.7)$$

- With energy loss fluctuations:
The effect is the largest if we consider low particle masses and small step sizes, so that the Gamma distribution is applied. An extreme example shall be given. Instead of taking a lot of steps with low energy deposition and a few with high energy deposition, we assume that in 9 out of 10

steps, the amount can be entirely neglected, while in a single step, the total energy E is deposited. If this is the case, then the light output reads

$$L = \Delta L = \frac{S \cdot E}{1 + kB \cdot \frac{E}{\Delta x}} \quad , \quad (7.8)$$

and the resulting LY is given by

$$LY = \frac{L}{E} = \frac{S}{1 + kB \cdot \frac{E}{\Delta x}} \quad . \quad (7.9)$$

This case study shows that the difference between the two extremes is given by a factor 10 (i.e. the number of steps considered) in the part of the denominator, where the Birks parameter kB contributes, which accounts for the quenching and non-proportionality. The real physical situation will be somewhere between the extreme cases of exactly following the mean energy loss, on the one hand, and such large fluctuations that only in a single step a high amount of energy is deposited, on the other hand.

From this example it is obvious, however, that energy loss fluctuations, in general, lead to a decreased LY. The strength of this effect depends on the model applied and on its parameters. Therefore, in our simulations, a greater shift will be seen for α -particles and O ions compared to the Ca and W ions.

Results with activated Energy Loss Fluctuations

In the previous subsections, a description of the effect that is expected due to energy loss fluctuations is discussed. Now, the actual simulations are conducted, analysed and compared for the different models considered in sections 7.4 - 7.7. For this purpose, the simulations are rerun with the same settings as in the mentioned sections, except for activating energy loss fluctuations. The maximum step size is therefore again set to 1 nm. A further subsection will be dedicated to the impact of this parameter value on the results.

In the following, we present the simulated data obtained with our various models. The plots of the nuclear recoil bands are given in Fig. 7.21. The first graphic, Fig. 7.21(a), shows the result for the standard Geant4 stopping model with step limit, as discussed in section 7.4. The second one, Fig. 7.21(b), gives the results for SRIM stopping powers in combination with a step limit (cf. section 7.5). Finally, in the third one, Fig. 7.21(c), the data obtained with the modified screened nuclear recoil model, discussed in section 7.7, are depicted. The effects described in the previous subsection are present, but there are some essential differences between the distinct models.

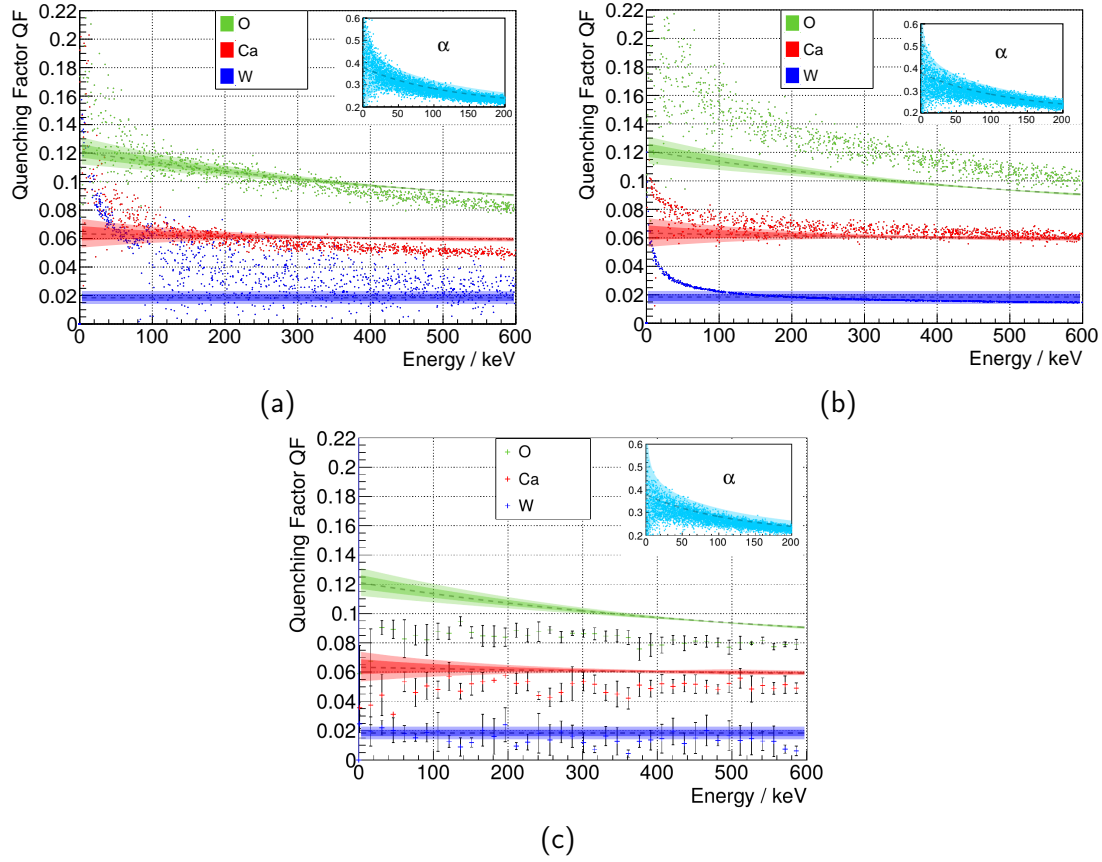


Figure 7.21.: Comparison between the different models discussed in sections 7.4 - 7.7 with activated energy loss fluctuations and a step limit of 1 nm for nuclear recoils and 4 nm for α -particles: (a) represents the standard Geant4 stopping model, (b) the model using SRIM stopping powers and (c) the adapted model of screened nuclear recoils. The dashed lines (mean values) and shaded areas (1σ and 2σ error bounds, cf. Fig. 6.3 for nuclear recoils and Fig. 3.2 for alphas) represent the experimental reference data.

Looking at Fig. 7.21(a) and comparing it to the result without energy loss fluctuations depicted in Fig. 7.12, a broadening of the bands is the most obvious consequence. If we further compare the mean QF values, we can obtain almost unchanged values for W and only slightly lowered ones for Ca, whereas for O there is a clear decrease, which gets more pronounced towards lower energies. Looking at the data points of W, somewhere below 100 keV a change of models obviously happens. Further analysis shows that above ~ 80 keV a Gamma distribution is applied, whereas below this energy it is a uniform distribution. Seemingly, the Gamma distribution leads to a very strong broadening compared to the uniform one. This is not entirely understood, as the QFs of Ca and O are modeled with a Gamma distribution across

the whole depicted energy region and do not show such severe variations. Although the QF of O looks better after adding the fluctuations, all in all, the model does not present a good fit to the experimental data. The behaviour of the mean QF values of W and Ca does not change significantly and, especially at low energies, deviates strongly from the pattern obtained in the experiment.

Fig. 7.21(b), displaying the results using SRIM stopping powers, shows a somewhat different picture. The energy loss fluctuations of W are modeled via a uniform distribution in the entire energy region and the respective QF curve is hardly broadened. For Ca and O, this is different, as down to a certain energy, a Gamma distribution is applied. In the case of Ca, for example, only below ~ 10 keV the fluctuation model changes to a uniform distribution. It is hard to see in the graphic, but below this energy, the broadening is less pronounced. The same has been obtained in Fig. 7.21(a) for the W band. Comparing the mean QFs to those presented in Fig. 7.15, the greatest shift to lower values is present for O, while the Ca band is only slightly altered and the W band almost exactly stays the same due to very small fluctuations relative to the mean energy losses. This behaviour is similar to the one obtained with the standard Geant4 stopping powers.

In Fig. 7.21(c), the effect of energy loss fluctuations on the data obtained with the modified screened nuclear recoil model is shown. Rerunning the simulations (cf. Fig. 7.20), which represented the experimental curves rather well, now results in stronger deviations. Just as before, the mean QFs are shifted to lower values, with a larger shift for lighter particles. One could try to adapt the parameters (*RecoilCutoff* and *StoppingCutoff*) to improve the simulation. However, any adaptation would increase the QF of W the most, while the QF of O would almost stay the same due to the cutoff values only affecting the total number of recoiling nuclei generated, but not the relative composition of the recoil cascade and due to the fact that no recoiling nuclei with higher QFs than those of O, which could shift the O band to higher values, are present. Thus, any changes would not substantially improve the results, so that this phenomenological model seems to lose its validity.

The model that might come closest to the experiment is the one using SRIM stopping powers and limiting the step length, although none of the models yields a satisfying fit across the entire energy region considered in the plots. Especially at low energies, except for the screened nuclear recoil model, the models still show a rather steep slope towards larger values, which is not expected from experimental observations.

Impact of the Step Limit Value

In this section, the impact of the step limit on the simulated results is discussed by taking the example of the best-fitting model (SRIM + step limit + fluctuations).

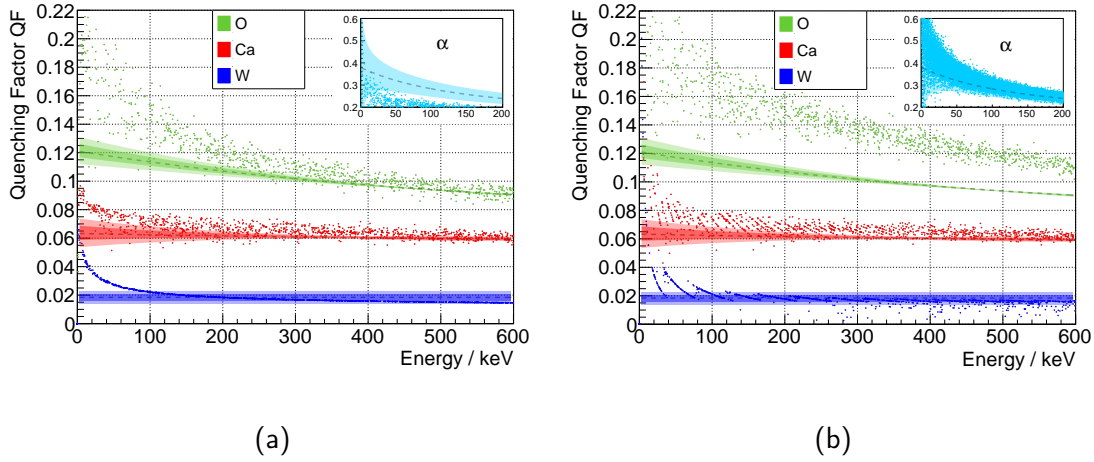


Figure 7.22.: Different step limits and their impacts on the QFs of nuclear recoils in CaWO_4 are analysed for the model using SRIM stopping powers in the simulations. In (a), a maximum step size of 0.5 nm for nuclear recoils and 1 nm for α -particles is chosen, while in (b), a larger value of 10 nm for both, nuclear recoils and α -particles, is tested.

The data in Fig. 7.21(b) are obtained with a step limit of 1 nm. A variation of this length leads to different distributions being used in modeling the fluctuations and to modified parameters of a certain distribution.

Further reducing the maximum step length to 0.5 nm results in the data depicted in Fig. 7.22(a). Looking at the Ca band, for which a change of the broadness could be seen at ~ 10 keV for a step limit of 1 nm due to an alteration of the applied distribution, this change can now be obtained at a slightly higher energy of ~ 20 keV. Also, the shape parameter of the Gamma distribution is reduced, leading to larger variations between low and high energy depositions. Hence, the QFs are reduced for the lower step limit. Again, this effect is more pronounced for lighter particles. The QF of O therefore further approaches the experimental curve. A lower step limit may lead to an additional reduction of the QF. However, the bad behaviour at low energies seemingly continues to exist.

A larger value of the step limit obviously leads to the opposite effect. The QF of O increases and the fit to the experiment gets worse. Furthermore, at some point, problems with the simulation occur, if the step length is too high for the considered energies, which has been the motivation to introduce a step limit in the first place. These effects can be seen in Fig. 7.22(b), where a maximum step size of 10 nm is applied. The issues with Ca and W are obvious, especially towards low energies, and the increased QF of O can be seen as well.

Finally, a depiction of the whole LY spectrum, also showing α -particles and

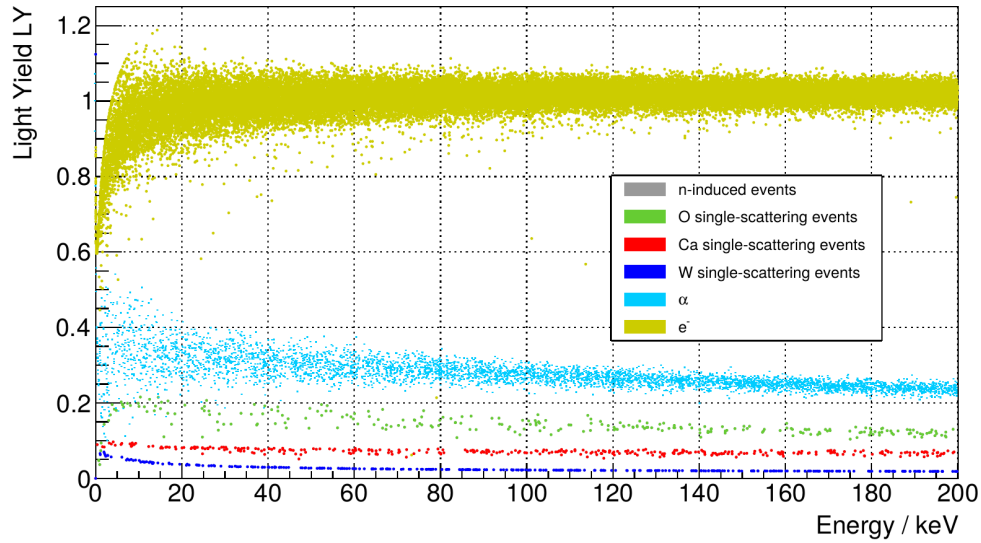


Figure 7.23.: Results across the whole LY spectrum are depicted for simulations with SRIM stopping powers and activated energy loss fluctuations. The step limit for nuclear recoils is 0.5 nm, whereas, for α -particles, it is 4 nm.

electrons, is given in Fig. 7.23. For the nuclear recoil bands, a step limit of 0.5 nm is chosen, while for the α -particles, the limit is set to 4 nm, in order to obtain data points close to the experimentally expected values. If this large-scale plot is compared to the schematic model in Fig. 3.2, it can be shown, that within the error bars, all QFs except for the one of O fit rather well. An overlay of these two plots is presented in Fig. 7.24. Increasing the fluctuations slightly more by reducing the step limit even further might lead to better fitting data of the nuclear recoils. Thus, looking at these results, the simulation may at least give an idea of where the different QF bands are located. However, a closer comparison to the experiment, zooming in on the nuclear recoil bands, fails to produce precise results.

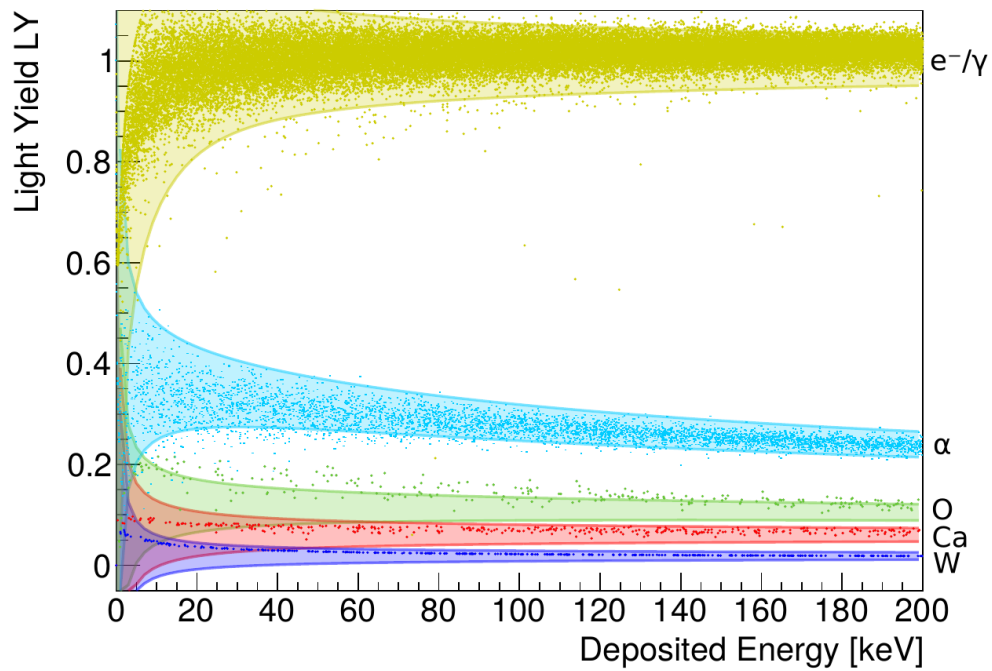


Figure 7.24.: An overlay of Fig. 3.2 and Fig. 7.23 is presented, in order to show how comparable the simulations are to the schematic depiction of expected LYs. A good agreement is found for electrons, alphas and part of the nuclear recoils.

Chapter 8.

Summary and Conclusion

The CRESST experiment searches for dark matter by looking for dark matter induced nuclear recoils in cryogenic CaWO_4 crystals. Nuclear recoils of O, Ca and W are distinguished from the e^-/γ and α background via their LY. Hence a detailed understanding of the LY is important.

So far, CRESST used a dedicated parametrization of the O, Ca and W populations with 9 parameters, which need to be determined empirically via calibration measurements and ML fits. The aim of this work was to predict the populations of O, Ca and W via MC simulations, using only the measurements of the e^-/γ band, hence reducing the number of free parameters from initially 9 to ideally 2.

Our simulations are based on the MC code Geant4 and provide information about the created particle cascades, energy depositions, step lengths and various other features. Based on these simulated data, we followed the approach of calculating the generated light output (L) with the help of the empirical Birks formula (Eq. (3.1)). The two Birks parameters A and kB , which can be determined for a certain crystal from gamma calibration data, might in the ideal case be sufficient to predict the LYs of all other particles. In order to compare our results to experimental data, we used the parameter values determined for CRESST target crystal 'Daisy', which take the values [27] $A = (1.096 \pm 0.003) \text{ keV}_{ee}/\text{keV}$ and $kB = (18.5 \pm 0.7) \text{ nm}/\text{keV}$.

Problems with the simulations using the standard version of Geant4 (v4.10.2.1) with default settings were detected in our low-energetic region of interest. As the easiest solution of applying a step limit to the simulations, which at least lead to a correct treatment of all the mechanisms contributing to the energy loss process, still failed in producing satisfying results, further adaptations were tested.

Standard stopping powers in Geant4 are taken from tabulated data published by the ICRU [41]. As an alternative, we made a further widely accepted source for stopping powers, namely SRIM [37, 42], available in the simulations. The results with these stopping powers looked more promising, because the gradients of the simulated QF curves and also the absolute QF values were in better agreement with the ones obtained in the experiment.

Still, a further model was tested, which should extend the precision of the contribution of nuclear stopping by applying a screened interatomic potential, computing the explicit solution of the scattering integral and creating nuclear recoiling secondaries [43]. However, this model uses a semi-empirical approach and can be customised via some adjustable parameters, for which no values could be found that would result in a correct simulation of all particles and energies. Therefore, an adaptation of the model, splitting one of its parameters, the *RecoilCutoff*, into two parts, was implemented. With this model, the number of free parameters needed to describe the QFs might increase to 4, i.e. A , kB and the 2 cut-parameters, if the latter are also crystal dependent. Still, this would be an improvement compared to the 9 parameters used so far. However, better results could only be obtained by neglecting energy loss fluctuations.

The effect of energy loss fluctuations was discussed in the last part of this thesis. Every deviation from the mean energy loss leads to a reduced LY and QF, as there is an enhanced local energy deposition (large dE/dx) in some steps, increasing the quenching effect, meaning that less light is generated for the same amount of deposited energy. The fluctuation model and the amplitude of fluctuations vary with the mass of the incident particle, its energy and also with the maximum step length manually added to the code. An estimate of the real physical energy loss fluctuations present in the experiment would be needed to assess the goodness of the model. One may ask, for example, if the use of Gaussian, Gamma or uniform distributions and their respectively calculated standard deviations are justified. The chosen maximum step length can be used to modify the fluctuations. Smaller step size generally leads to increasing fluctuations and therefore lower LYs and QFs. When enabling energy loss fluctuations, the simulation model using SRIM stopping powers shows the best results, although not precisely fitting the experimental data, especially at low energies $\lesssim 100$ keV. The screened model, however, totally fails in producing acceptable results for all particles and energies.

In conclusion, a huge improvement compared to the results obtained with standard Geant4 settings could be achieved. Still, an accurate modeling of LYs and QFs based on Geant4 and Birks law could not be gained. Only a rather rough estimate, of where to find the different QF curves for a certain crystal, can be given after determining the Birks parameters of that crystal from its gamma calibration data. To achieve results with higher precision, one could either try to analyse and adapt the fluctuation model, which might be a doubtful approach, however. Alternatively, one would have to switch to a very different, more complex simulation method, which does not rely on Birks law, but rather uses a detailed description of the quenching process by applying a microscopic model. As this relies on solid state physics, it may not be feasible to implement it in Geant4, which was designed to simulate nuclear, particle, and atomic physics.

Appendix A.

Simulation and Analysis Software and Scripts

This section briefly introduces the software used for all simulations and corresponding data analyses conducted in the course of this thesis. Extensive additional information can be found within the citations given in the respective sections below. For our simulations we use ImpCRESST, the simulation code of the CRESST experiment which is based on the Geant4 simulation toolkit (v10.2.1). The analysis is done with Root (v6.36.36).

A.1. Geant4

Geant4 is a Monte Carlo (MC) simulation software toolkit based on the programming language C++. It has been designed especially for the purpose of tracking single particles passing through matter and interacting with other particles [44, 45].

The single particle approach leads to a perfect data treatment and preparation for an event-by-event based analysis. Standard classes, functions and libraries for geometry, materials, particles, primary event generation, tracking, physics models and processes, sensitive detectors, data generation, information storage and visualisation exist. Their files are open source and can therefore be utilized and modified to meet one's demands.

The tracking of a particle in the simulation works as follows:

A primary particle (track) is created with a certain initial position and momentum. For this primary particle, different physics processes may be possible, e.g. a hadronic process, a decay or pure transportation without interaction. The simulation proceeds in single steps. The step length and the process for each step are chosen randomly but according to the probabilities for the occurrence of each process and according to its mean free path (MC approach). At the end of the step, the particle status is updated with the new momentum, energy, direction and

position after applying the given process and secondary particles (tracks) may be generated. Such steps are simulated for each track until the particle annihilates, is captured, leaves the observed volume or has a kinetic energy below a user-specified cut-off. In the latter case, the particle track is terminated but the kinetic energy is locally deposited, hence the conservation of energy is considered.

Information, that a user wants to obtain, can be written to a .root-file during simulation. This output may include positions, times, particle momenta and energies, process names, energy depositions, step lengths, etc. for each interaction.

A.1.1. UI/Macro Files

A macro can be used to define all parameters of the simulations via user interface (UI) commands and then start the simulation. An example of such a file is given in the following, where neutrons are started from the surface of a sphere around the target cube, with momentum direction towards the inside of the sphere and an incident energy of 2 MeV. The chosen detector geometry (CaWO4Cube) is defined in a separate C++ file. Low-energy electromagnetic physics are enabled and energy loss fluctuations are deactivated in this example. Finally, the command '/run/beamOn x' starts a simulation with x incident particles.

```

1 #Read RNG status from file
2 #/random/resetEngineFrom ./seed.rndm
3
4 #Store RNG status to file and
5 #provide status also to user code
6 /run/storeRndmStatToEvent 1
7
8 #No detailed printout during the simulation run
9 /tracking/verbose 0
10
11 #Enable visualization
12 #/control/execute ./vis.mac
13
14 #Use a free-floating, CaWO4 cube as geometry
15 #The available geometries are listed in '
    ExperimentalSetupFactory.cc'
16 /geometry/setSetup CaWO4Cube
17 /geometry/buildSetup
18
19 #Set primary particle via the General Particle Source
20 #Start neutrons from a sphere around the cube

```



```

21 /source/type gps
22 /gps/particle neutron
23 /gps/pos/type Surface
24 /gps/pos/shape Sphere
25 /gps/pos/centre 0.0 0.0 0.0 mm
26 #The radius has to be adapted to the chosen geometry
27 /gps/pos/radius 50 mm
28 /gps/ang/type iso
29 /gps/ang/mintheta 0 deg
30 /gps/ang/maxtheta 90 deg
31 /gps/ang/minphi 0 deg
32 /gps/ang/maxphi 360 deg
33 /gps/ang/surfnorm true
34 /gps/ene/mono 2 MeV
35
36 #Enable low-energy physics
37 /run/initialize
38 /process/em/deexcitation World true true true
39 /process/em/fluo true
40 /process/em/aufer true
41 /process/em/pixe true
42 /process/em/deexcitationIgnoreCut true
43
44 /process/eLoss/fluct false
45
46 #Set name of output file
47 /data/setPrefix ./neutrons_2MeV_10000_fluct_off_
48 #Store all tracks, including those which don't create
   hits
49 /data/storeAllTracks true
50 /run/particle/dumpCutValues
51 #Start simulation
52 /run/beamOn 10000

```

A.1.2. Stepping Performance

In the following, we want to give a short overview over the technical details of how Geant4 performs the steps of a particle in the simulations. The description is focused on the invocation of energy loss processes, as these are most important for our work.

A class called `G4SteppingManager` controls all the methods contributing in each step of a particle. Its function `G4SteppingManager::InvokeAlongStepDoIts` is in charge of calling the `AlongStepDoIt` methods of the respective processes.

First, the function dealing with the electronic stopping of a particle is invoked, which is `G4VEnergyLossProcess::AlongStepDoIt`. If the step length is greater than the final range calculated for the kinetic energy of the particle in the material it traverses, the energy loss is set to be equal to the kinetic energy, which means that the particle is stopped. Otherwise, if the particle is an ion, the function `currentModel->CorrectionsAlongStep` is called, where `currentModel` refers to the parametrised model in `G4IonParametrisedLossModel` when using the electromagnetic physics list `G4EmStandardPhysics_option4`. For the calculation of the electronic stopping power `G4IonParametrisedLossModel::ComputedEDXPerVolume` is invoked. Corrections to the calculation with tabulated values are applied, if the energy loss exceeds a certain fraction of the kinetic energy of the particle. The step length is then refined to gain higher accuracy.

Afterwards, nuclear stopping is taken into account via calling the `AlongStepDoIt` method of `G4NuclearStopping`. The mean kinetic energy between the value before the step and the one after subtracting the proposed electronic energy loss is taken as the projectile energy. The nuclear energy loss for the given ion-material combination is then calculated via `G4ICRU49NuclearStoppingModel::ComputedEDXPerVolume`.

A.2. Root

ROOT [46, 47] is an object oriented data analysis framework written in C++. It has been developed due to the ever growing amount of data produced in modern particle physics experiments. Typically, it can be applied very effectively for analysis and visualisation of real or simulated data that consist of many statistically independent events with the same data structure.

Selective data access is guaranteed via vertical data partitioning of user-defined objects. They are implemented in a so-called *TTree* which stores different *TBranches*. Such a branch can itself be partitioned into further branches and/or store objects or data members of a class. A simple data member or variable is the end point of a branch and is called a leaf. This tree structure increases read-out speed of desired information.

For visualisation of the data, one can, for example, draw a graph using the *TGraph* class or a histogram with the base class *TH1*.

A.2.1. Root Analysis Script

In the following, the most important Root script developed for our LY/QF analysis is presented. This script creates a new .root-file containing the LY data extracted from the .root-files created during the simulations by looping over the particle cascades and calculating the light output in each step. The cascades are tracked by the recursive function 'getHitData' and every light output is assigned to the particle initially creating the secondaries. Not only the light outputs and energy depositions, but all information that might be useful for further analysis, e.g. if an initial neutron only scattered on a single nucleus, is recorded. The code of this script is printed below:

```

1 double calculateLightYield( double dE, double dx ) {
2     // calculates dL using Birk's formula
3
4     const double A = 1.096;                // A=(1.096+- .003)
5     keV_(ee)/keV
6     const double kB = 18.5e-3; // mm/MeV // kB=(18.5+- .7) nm
7     /keV. Both values taken from arXiv:0910.4414v1
8     return A*dE / (1 + kB*dE/dx);
9 }
10
11 void getHitData( Cresst::Data::Event *myEvent,
12     const Cresst::Data::Track *myTrack,
13     std::string particleName,
14     const std::string &gpsParticleName,
15     std::vector<double> &energyDeposits_Ca,
16     std::vector<double> &energyDeposits_W,
17     std::vector<double> &energyDeposits_0,
18     std::vector<double> &energyDeposits_primary,
19     ,
20     std::vector<double> &stepLengths_Ca,
21     std::vector<double> &stepLengths_W,
22     std::vector<double> &stepLengths_0,
23     std::vector<double> &stepLengths_primary,
24     std::vector<double> &E_Ca,
25     std::vector<double> &E_W,
26     std::vector<double> &E_0,
27     std::vector<double> &E_primary,
28     unsigned int &multiplicity_Ca,
29     unsigned int &multiplicity_W,

```

```

28         unsigned int                &multiplicity_0,
29         unsigned int                &multiplicity_primary,
30         int &nbCaEvents, int &nbWEvents, int &nbOEvents, int
        &nbPrimaryEvents,
31         int &nbCaHits, int &nbWHits, int &nbOHits, int &
        nbPrimaryHits) {
32
33         // determine the nucleus that caused a particle cascade
        or energy deposition:
34         std::string nucleusName = particleName;
35         particleName = myTrack->GetParticleName();
36         if(particleName.find("Ca") != std::string::npos) {
37             nucleusName = "Ca";
38             multiplicity_Ca++;
39             nbCaEvents++;
40         } else if(particleName.find("W") != std::string::npos)
        {
41             nucleusName = "W";
42             multiplicity_W++;
43             nbWEvents++;
44         } else if(particleName.find("O") != std::string::npos)
        {
45             nucleusName = "O";
46             multiplicity_O++;
47             nbOEvents++;
48         }
49
50         // obtain data for each nucleus:
51         if(nucleusName == "Ca") {
52             for(unsigned int i=0; i<myTrack->GetNbOfHits(); i++)
        {
53                 energyDeposits_Ca.push_back( myTrack->GetHits()->at
        (i)->GetEnergyDeposit() );
54                 stepLengths_Ca.push_back ( myTrack->GetHits()->at(i)
        ->GetStepLength() );
55                 if(2*i+1 < myTrack->GetNbOfParticleStatuses()){
56                     E_Ca.push_back ( myTrack->GetParticleStatuses()->
        at(2*i+1)->GetKineticEnergy() );
57                 }
58                 nbCaHits++;
59             }
60         }

```

```

61  if(nucleusName == "W") {
62      for(unsigned int i=0; i<myTrack->GetNbOfHits(); i++)
63      {
64          energyDeposits_W.push_back( myTrack->GetHits()->at(
65          i)->GetEnergyDeposit() );
66          stepLengths_W.push_back ( myTrack->GetHits()->at(i)
67          ->GetStepLength() );
68          if(2*i+1 < myTrack->GetNbOfParticleStatuses()){
69              E_W.push_back ( myTrack->GetParticleStatuses()->
70              at(2*i+1)->GetKineticEnergy() );
71          }
72          nbWHits++;
73      }
74  }
75  if(nucleusName == "O") {
76      for(unsigned int i=0; i<myTrack->GetNbOfHits(); i++)
77      {
78          energyDeposits_O.push_back( myTrack->GetHits()->at(
79          i)->GetEnergyDeposit() );
80          stepLengths_O.push_back ( myTrack->GetHits()->at(i)
81          ->GetStepLength() );
82          if(2*i+1 < myTrack->GetNbOfParticleStatuses()){
83              E_O.push_back ( myTrack->GetParticleStatuses()->
84              at(2*i+1)->GetKineticEnergy() );
85          }
86          nbOHits++;
87      }
88  }
89  if(nucleusName == gpsParticleName) {
90      for(unsigned int i=0; i<myTrack->GetNbOfHits(); i++)
91      {
92          energyDeposits_primary.push_back( myTrack->GetHits
93          (->at(i)->GetEnergyDeposit() );
94          stepLengths_primary.push_back ( myTrack->GetHits()
95          ->at(i)->GetStepLength() );
96          E_primary.push_back ( myTrack->GetStartStatus()->
97          GetKineticEnergy() );
98          nbPrimaryHits++;
99      }
100  }
101  // descend to 'lower levels':

```

```

91   for(unsigned int i=0; i<myTrack->GetSecTracks()->size()
92       ; i++) {
93       getHitData( myEvent,
94       myTrack->GetSecTracks()->at(i),
95       nucleusName,
96       gpsParticleName,
97       energyDeposits_Ca,
98       energyDeposits_W,
99       energyDeposits_O,
100      energyDeposits_primary,
101      stepLengths_Ca,
102      stepLengths_W,
103      stepLengths_O,
104      stepLengths_primary,
105      E_Ca,
106      E_W,
107      E_O,
108      E_primary,
109      multiplicity_Ca,
110      multiplicity_W,
111      multiplicity_O,
112      multiplicity_primary,
113      nbCaEvents, nbWEvents, nbOEvents, nbPrimaryEvents,
114      nbCaHits, nbWHits, nbOHits, nbPrimaryHits);
115  }
116  }
117
118
119  void
120      lightYield_createTreeFromSim_newBranches_newSingleScatteringQuery
121      () {
122
123      // name of root file containing ImpCRESST simulation
124      data:
125      const std::string rootFileName = "...";
126      //
127      // name of particles from the Geant4 gps ('general
128      particle source'):
129      const std::string gpsParticleName = "...";
130      //
131      // (core) name of ROOT output files (without extension

```

```

    '.root'):
128 std::string outFileName_root = "...";
129 //////////////////////////////////////////
130
131 TFile *rawData = new TFile(rootFileName.c_str());
132 TTree *inTree = nullptr;
133 rawData->GetObject("tree", inTree);
134 Cresst::Data::Event *myEvent = nullptr;
135 inTree->SetBranchAddress("event", &myEvent);
136 outFileName_root += inTree->GetEntries() +
    gpsParticleName + ".root";
137 TFile *outFile_root = new TFile(outFileName_root.c_str
    (), "recreate");
138
139 // this tree holds the structure that is eventually
    written into a ROOT file:
140 TTree outTree("T", "lightYieldData");
141
142 // these variables contain the tree data at the end of
    each event
143 unsigned int eventID;
144 double energyDeposit_total,
145     energyDeposit_CaFraction,
146     energyDeposit_WFraction,
147     energyDeposit_OFraction,
148     energyDeposit_primaryFraction;
149 double lightYield_total,
150     lightYield_CaFraction,
151     lightYield_WFraction,
152     lightYield_OFraction,
153     lightYield_primaryFraction;
154 double initial_energy;
155 unsigned int NbNeutronScatterings;
156 unsigned int multiplicity_Ca,
157     multiplicity_W,
158     multiplicity_O,
159     multiplicity_primary;
160 const unsigned int max = 50000;
161 unsigned int NbenergyDeposit_Ca,
162     NbenergyDeposit_W,
163     NbenergyDeposit_O,
164     NbenergyDeposit_primary;

```

```

165 double dE_Ca[max], dE_W[max], dE_O[max], dE_primary[max
166 ];
167 double dx_Ca[max], dx_W[max], dx_O[max], dx_primary[max
168 ];
169 double Ekin_prestep_Ca[max], Ekin_prestep_W[max],
170 Ekin_prestep_O[max], Ekin_prestep_primary[max];
171
172 outTree.Branch("eventID", &eventID, "eventID/i");
173
174 outTree.Branch("energyDeposit_total", &
175 energyDeposit_total, "energyDeposit_total/D");
176 outTree.Branch("energyDeposit_CaFraction", &
177 energyDeposit_CaFraction, "energyDeposit_CaFraction/D"
178 );
179 outTree.Branch("energyDeposit_WFraction", &
180 energyDeposit_WFraction, "energyDeposit_WFraction/D");
181 outTree.Branch("energyDeposit_OFraction", &
182 energyDeposit_OFraction, "energyDeposit_OFraction/D");
183 outTree.Branch("energyDeposit_primaryFraction", &
184 energyDeposit_primaryFraction, "
185 energyDeposit_primaryFraction/D");
186
187 outTree.Branch("NbenergyDeposit_Ca", &
188 NbenergyDeposit_Ca, "NbenergyDeposit_Ca/i");
189 outTree.Branch("NbenergyDeposit_W", &NbenergyDeposit_W,
190 "NbenergyDeposit_W/i");
191 outTree.Branch("NbenergyDeposit_O", &NbenergyDeposit_O,
192 "NbenergyDeposit_O/i");
193 outTree.Branch("NbenergyDeposit_primary", &
194 NbenergyDeposit_primary, "NbenergyDeposit_primary/i");
195
196 outTree.Branch("dE_Ca", &dE_Ca, "dE_Ca[
197 NbenergyDeposit_Ca]/D");
198 outTree.Branch("dE_W", &dE_W, "dE_W[NbenergyDeposit_W]/
199 D");
200 outTree.Branch("dE_O", &dE_O, "dE_O[NbenergyDeposit_O]/
201 D");
202 outTree.Branch("dE_primary", &dE_primary, "dE_primary[
203 NbenergyDeposit_primary]/D");
204
205 outTree.Branch("dx_Ca", &dx_Ca, "dx_Ca[
206 NbenergyDeposit_Ca]/D");

```



```

188 outTree.Branch("dx_W", &dx_W, "dx_W[NbenergyDeposit_W]/
    D");
189 outTree.Branch("dx_O", &dx_O, "dx_O[NbenergyDeposit_O]/
    D");
190 outTree.Branch("dx_primary", &dx_primary, "dx_primary[
    NbenergyDeposit_primary]/D");
191
192 outTree.Branch("Ekin_prestep_Ca", &Ekin_prestep_Ca, "
    Ekin_prestep_Ca[NbenergyDeposit_Ca]/D");
193 outTree.Branch("Ekin_prestep_W", &Ekin_prestep_W, "
    Ekin_prestep_W[NbenergyDeposit_W]/D");
194 outTree.Branch("Ekin_prestep_O", &Ekin_prestep_O, "
    Ekin_prestep_O[NbenergyDeposit_O]/D");
195 outTree.Branch("Ekin_prestep_primary", &
    Ekin_prestep_primary, "Ekin_prestep_primary[
    NbenergyDeposit_primary]/D");
196
197 outTree.Branch("initial_energy", &initial_energy, "
    initial_energy/D");
198
199 outTree.Branch("NbNeutronScatterings", &
    NbNeutronScatterings, "NbNeutronScatterings/i");
200
201 outTree.Branch("lightYield_total", &lightYield_total, "
    lightYield_total/D");
202 outTree.Branch("lightYield_CaFraction", &
    lightYield_CaFraction, "lightYield_CaFraction/D");
203 outTree.Branch("lightYield_WFraction", &
    lightYield_WFraction, "lightYield_WFraction/D");
204 outTree.Branch("lightYield_OFraction", &
    lightYield_OFraction, "lightYield_OFraction/D");
205 outTree.Branch("lightYield_primaryFraction", &
    lightYield_primaryFraction, "
    lightYield_primaryFraction/D");
206
207 outTree.Branch("multiplicity_Ca", &multiplicity_Ca, "
    multiplicity_Ca/i");
208 outTree.Branch("multiplicity_W", &multiplicity_W, "
    multiplicity_W/i");
209 outTree.Branch("multiplicity_O", &multiplicity_O, "
    multiplicity_O/i");
210 outTree.Branch("multiplicity_primary", &

```

```

multiplicity_primary, "multiplicity_primary/i");
211
212 // counting variables:
213 int nbCaEvents = 0, nbWEvents = 0, nbOEvents = 0,
    nbPrimaryEvents = 0;
214 int nbCaHits = 0, nbWHits = 0, nbOHits = 0,
    nbPrimaryHits = 0;
215 const int nbEvents = inTree->GetEntries();
216
217 // loop over all events:
218 for(unsigned int ev=0; ev<nbEvents; ev++) {
219     if(ev%100==0) std::cout << "Processing event " << ev
    << " of " << inTree->GetEntries()
220         << "... (" << ev/double(inTree->GetEntries())*
    100 << " %)" << std::endl;
221
222     inTree->GetEntry(ev);
223
224     std::string particleName = gpsParticleName;
225
226     // reset variables:
227     energyDeposit_total = 0;
228     energyDeposit_CaFraction = 0;
229     energyDeposit_WFraction = 0;
230     energyDeposit_OFraction = 0;
231     energyDeposit_primaryFraction = 0;
232     lightYield_total = 0;
233     lightYield_CaFraction = 0;
234     lightYield_WFraction = 0;
235     lightYield_OFraction = 0;
236     lightYield_primaryFraction = 0;
237     multiplicity_Ca = 0;
238     multiplicity_W = 0;
239     multiplicity_O = 0;
240     multiplicity_primary = 0;
241     NbenergyDeposit_Ca = 0;
242     NbenergyDeposit_W = 0;
243     NbenergyDeposit_O = 0;
244     NbenergyDeposit_primary = 0;
245     NbNeutronScatterings = 0;
246     memset(dE_Ca, 0, sizeof(dE_Ca));
247     memset(dE_W, 0, sizeof(dE_W));

```

```

248     memset(dE_0, 0, sizeof(dE_0));
249     memset(dE_primary, 0, sizeof(dE_primary));
250     memset(dx_Ca, 0, sizeof(dx_Ca));
251     memset(dx_W, 0, sizeof(dx_W));
252     memset(dx_0, 0, sizeof(dx_0));
253     memset(dx_primary, 0, sizeof(dx_primary));
254     memset(Ekin_prestep_Ca, 0, sizeof(Ekin_prestep_Ca));
255     memset(Ekin_prestep_W, 0, sizeof(Ekin_prestep_W));
256     memset(Ekin_prestep_0, 0, sizeof(Ekin_prestep_0));
257     memset(Ekin_prestep_primary, 0, sizeof(
Ekin_prestep_primary));
258     std::vector<double> energyDeposits_Ca(0),
259         energyDeposits_W(0),
260         energyDeposits_0(0),
261         energyDeposits_primary(0);
262     std::vector<double> stepLengths_Ca(0),
263         stepLengths_W(0),
264         stepLengths_0(0),
265         stepLengths_primary(0);
266     std::vector<double> E_Ca(0),
267         E_W(0),
268         E_0(0),
269         E_primary(0);
270
271     initial_energy = myEvent->GetPrimaryTrack()->
GetStartStatus()->GetKineticEnergy();
272
273     if(myEvent->GetPrimaryTrack()->GetParticleName() == "
neutron"){
274         NbNeutronScatterings = myEvent->GetPrimaryTrack()->
GetNbOfSecTracks();
275     }
276
277     // track the cascade particles and obtain data:
278     getHitData( myEvent,
279         myEvent->GetPrimaryTrack(),
280         particleName,
281         gpsParticleName,
282
283         energyDeposits_Ca,
284         energyDeposits_W,
285         energyDeposits_0,

```

```

286     energyDeposits_primary ,
287     stepLengths_Ca ,
288     stepLengths_W ,
289     stepLengths_0 ,
290     stepLengths_primary ,
291     E_Ca ,
292     E_W ,
293     E_0 ,
294     E_primary ,
295
296     multiplicity_Ca ,
297     multiplicity_W ,
298     multiplicity_0 ,
299     multiplicity_primary ,
300
301     nbCaEvents , nbWEvents , nbOEvents , nbPrimaryEvents ,
302     nbCaHits , nbWHits , nbOHits , nbPrimaryHits);
303
304     NbenergyDeposit_Ca = energyDeposits_Ca.size();
305     NbenergyDeposit_W = energyDeposits_W.size();
306     NbenergyDeposit_0 = energyDeposits_0.size();
307     NbenergyDeposit_primary = energyDeposits_primary.size
308     ();
309
310     // calculate light yield:
311     for(unsigned int i=0; i<NbenergyDeposit_Ca; i++) {
312         energyDeposit_CaFraction += energyDeposits_Ca.at(i)
313         ; // not really a fraction at this point
314         lightYield_CaFraction += calculateLightYield(
315         energyDeposits_Ca.at(i), stepLengths_Ca.at(i) );
316         dE_Ca[i] = energyDeposits_Ca.at(i);
317         dx_Ca[i] = stepLengths_Ca.at(i);
318         if(i<E_Ca.size()) Ekin_prestep_Ca[i] = E_Ca.at(i);
319     }
320     for(unsigned int i=0; i<NbenergyDeposit_W; i++) {
321         energyDeposit_WFraction += energyDeposits_W.at(i);
322         lightYield_WFraction += calculateLightYield(
323         energyDeposits_W.at(i), stepLengths_W.at(i) );
324         dE_W[i] = energyDeposits_W.at(i);
325         dx_W[i] = stepLengths_W.at(i);
326         if(i<E_W.size()) Ekin_prestep_W[i] = E_W.at(i);
327     }

```

```

324     for(unsigned int i=0; i<NbenergyDeposit_0; i++) {
325         energyDeposit_0Fraction += energyDeposits_0.at(i);
326         lightYield_0Fraction += calculateLightYield(
energyDeposits_0.at(i), stepLengths_0.at(i) );
327         dE_0[i] = energyDeposits_0.at(i);
328         dx_0[i] = stepLengths_0.at(i);
329         if(i<E_0.size()) Ekin_prestep_0[i] = E_0.at(i);
330     }
331     for(unsigned int i=0; i<NbenergyDeposit_primary; i++)
{
332         energyDeposit_primaryFraction +=
energyDeposits_primary.at(i);
333         lightYield_primaryFraction += calculateLightYield(
energyDeposits_primary.at(i), stepLengths_primary.at(i)
) );
334         dE_primary[i] = energyDeposits_primary.at(i);
335         dx_primary[i] = stepLengths_primary.at(i);
336         Ekin_prestep_primary[i] = E_primary.at(i);
337     }
338
339     // some variables have to be prepared for the TTree
output:
340     energyDeposit_total = energyDeposit_CaFraction +
energyDeposit_WFraction + energyDeposit_0Fraction +
energyDeposit_primaryFraction;
341     if(energyDeposit_total != 0) {
342         energyDeposit_CaFraction /= energyDeposit_total; //
now it's actually a fraction
343         energyDeposit_WFraction /= energyDeposit_total;
344         energyDeposit_0Fraction /= energyDeposit_total;
345         energyDeposit_primaryFraction /=
energyDeposit_total;
346     }
347     lightYield_total = lightYield_CaFraction +
lightYield_WFraction + lightYield_0Fraction +
lightYield_primaryFraction;
348     if(lightYield_total != 0) {
349         lightYield_CaFraction /= lightYield_total;
350         lightYield_WFraction /= lightYield_total;
351         lightYield_0Fraction /= lightYield_total;
352         lightYield_primaryFraction /= lightYield_total;
353     }

```

```

354     eventID = myEvent->GetEventID();
355
356     outTree.Fill();
357 }
358 } // end of for loop over all events
359
360
361 std::cout << "Finished processing events." << std::endl
362     << std::endl;
363 rawData->Close();
364 outTree.Write(); std::cout << "File " <<
365     outFile_name_root << " created." << std::endl;
366 outFile_root->Close();
367
368 //////////////////////////////////////
369 // printing summary:
370 //////////////////////////////////////
371 std::cout << std::endl;
372 std::cout << "##### SUMMARY
373     #####" << std::endl;
374 std::cout << "    (" << nbEvents << " " <<
375     gpsParticleName << "s were fired)" << std::endl;
376 std::cout << "# Ca events:          " << nbCaEvents << "\t
377     --> # hits: " << nbCaHits << std::endl
378     << "# W events:          " << nbWEvents << "\t--> #
379     hits: " << nbWHits << std::endl
380     << "# O events:          " << nbOEvents << "\t--> #
381     hits: " << nbOHits << std::endl
382     << "# primary events: " << nbPrimaryEvents << "\t
383     --> # hits: " << nbPrimaryHits << std::endl;
384 std::cout << std::endl;
385 }

```

Appendix B.

New and Adapted Geant4 Classes

An overview over changes done to the Geant4 source code is briefly presented in this chapter. The different source files and important lines are listed in the following with a short description attached to them.

Electromagnetic Physics List

The electromagnetic physics list `G4EmStandardPhysics_option4`, which can be found in the Geant4 source files, has been adapted in a newly written `option5` to make the different physics models, that we have tested, available in the simulations.

Besides the standard nuclear stopping class `G4NuclearStopping`, a further class called `G4NuclearStoppingSRIM`, which is responsible for applying a parametrized loss model using SRIM stopping powers, and the class `G4ScreenedNuclearRecoil`, providing an extended nuclear stopping model based on a screened interatomic potential, are introduced. `G4NuclearStoppingSRIM` was developed within this work and `G4ScreenedNuclearRecoil` was taken from the Geant4 example 'TestEm7'. A modification of the latter, called `G4ScreenedNuclearRecoilMod`, was furthermore developed to improve the results. The following code snippet shows how to instantiate them:

```
262 // nuclear stopping
263 G4NuclearStopping* nuc = new G4NuclearStopping(); //
    standard nuclear stopping model provided by Geant4
264 G4NuclearStoppingSRIM* pnuc = new G4NuclearStoppingSRIM
    (); //parametrized model equal to
    G4IonParametrizedLossModel using SRIM data tables that
    have to be added to G4EML0W6.48/ion_stopping_data/
    srim_nuclear_stopping for nuclear stopping of O, Ca
    and W within CaWO4
265 G4ScreenedNuclearRecoil* nucr = new
    G4ScreenedNuclearRecoil(); //screened nuclear recoil
```

```

    model, that provides enhanced precision (but higher
    time and memory consumption)
266 G4ScreenedNuclearRecoilMod* nucr_mod = new
    G4ScreenedNuclearRecoilMod(); //modified screened
    nuclear recoil model
267 G4double energyLimit = 100.*MeV;
268 nucr->SetMaxEnergyForScattering(energyLimit);
269 nucr_mod->SetMaxEnergyForScattering(energyLimit);

```

Further down the code, when looping over the different particles, the previously instantiated processes together with others can be registered for alphas and ions. First, electronic stopping is activated via `G4ionIonisation` and chosen to be dealt with by `G4IonParametrisedLossModel`. The latter may be extended by adding a `DEDXTable` covering SRIM stopping powers (line 440), which have to be tabulated and added to the code repository beforehand (cf. section 7.5).

```

435 myG4ionIonisation* ionIoni = new myG4ionIonisation();
436
437 myIPLM = new myG4IonParametrisedLossModel();
438
439 //possibility to use SRIM data for electronic stopping:
440 myIPLM -> AddDEDXTable("SRIMElectronicStopping", new
    G4IonStoppingData("ion_stopping_data/
    srim_electronic_stopping"));
441
442 ionIoni->SetEmModel(myIPLM);
443 ionIoni->SetStepFunction(0.1, 1*um);
444 ph->RegisterProcess(ionIoni, particle);

```

One of the four available nuclear stopping models is then registered.

```

452 ph->RegisterProcess(nuc, particle); //standard nuclear
    stopping model

```

```

453 ph->RegisterProcess(pnuc, particle); //parametrized
    nuclear stopping model (SRIM)

```

```

454 ph->RegisterProcess(nucr, particle); //screened nuclear
    recoil model

```

```

455 ph->RegisterProcess(nucr_mod, particle); //modified
    screened nuclear recoil model

```


Additionally, the step limiter process is activated.

```

456  G4StepLimiter* steplim = new G4StepLimiter(); //step
    limiter process activation
457  ph->RegisterProcess(steplim, particle);

```

CaWO₄ Target Cube

In the file, which defines the target crystal, a maximum step length within the volume is defined. This value is applied to the simulation of each particle, for which the step limiter process has been registered in the electromagnetic physics list. As shown in the code snippet below, the step size is assigned to the logical volume of the crystal called 'cube_log'.

```

56  //////////// introduce a maximum step size to the logical
    volume, used by every particle for which the process
    G4StepLimiter is registered in
    G4EmStandardPhysics_option5
57      G4double maxStep = 1e-6*mm;
58      fStepLimit = new G4UserLimits(maxStep);
59      cube_log->SetUserLimits(fStepLimit);
60  ////////////////////////////////////////////

```

Parametrised Electronic Energy Loss Model

The main modification to the parametrised loss model dealing with electronic stopping, `G4IonParametrisedLossModel`, is making it accessible for α -particles by changing the minimum applicable atomic number (line 338) to 2.

```

337  //changed the minimum atomic number to 2, so that
    parametrized data can also be added/used for alphas
338  for(G4int atomicNumberIon = 2; atomicNumberIon < 102;
    atomicNumberIon++) {
339
340      LossTableList::iterator iter = lossTableList.begin();
341      LossTableList::iterator iter_end = lossTableList.end
    ();
342
343      for(; iter != iter_end; iter++) {
344
345          if(*iter == 0) {

```

```

346         G4cout << "myG4IonParametrisedLossModel::
Initialise():"
347             << " Skipping illegal table."
348             << G4endl;
349     }
350
351     G4bool isApplicable =
352         (*iter) -> BuildDEDXTable(atomicNumberIon,
material);
353
354     if(isApplicable) {
355 #ifdef PRINT_TABLE_BUILT
356         G4cout << "   Atomic Number Ion = " << atomicNumberIon
357             << ", Material = " << material -> GetName()
358             << ", Table = " << (*iter) -> GetName()
359             << G4endl;
360 #endif
361         break;
362     }
363 }
364 }

```

SRIM Nuclear Stopping Powers

A nuclear stopping class, very similar to `G4NuclearStopping` was developed within this work, making a new class accessible, which embodies the parametrised loss model for nuclear stopping. So, the main difference is in the initialisation method, reading:

```

90     if(!isInitialized) {
91         isInitialized = true;
92
93         if(!EmModel(1)) {
94             modelSRIMnuc = new SRIMNuclearStoppingModel(); //
choose the SRIM parametrized model
95             SetEmModel(modelSRIMnuc);
96         }
97         AddEmModel(1, EmModel());
98         EmModel()->SetParticleChange(&nParticleChange);
99     }

```

The SRIM nuclear stopping model is based on the `G4IonParametrisedLossModel`. It takes tabulated stopping power data for the calculation of energy losses, in this case due to nuclear stopping. The parameter `energyLossLimit` decides up to which fraction of the particle's kinetic energy the parametrized data are applied. Because no other parametrization, e.g. a precise high energy parametrization, is available, this parameter is set to 1, ensuring that the SRIM values are used in any case.

```

48 mySRIMNuclearStoppingModel::mySRIMNuclearStoppingModel(
49     const G4ParticleDefinition*,
50     const G4String& nam)
51 : G4VEmModel(nam),
52   nmbBins(90),
53   nmbSubBins(100),
54   particleChangeLoss(0),
55   corrFactor(1.0),
56   energyLossLimit(1), //instead 0.01, so that the
    parametrization is always used, no matter which
    fraction of the kinetic energy is lost in the process
57   cutEnergies(0)
58 {

```

The nuclear stopping power tables, which are taken from SRIM and added to the code repository in the correct format, are registered via:

```

67 // Load SRIM stopping power tables by default:
68 AddDEDXTable("SRIMNuclearStopping",
69     new G4IonStoppingData("ion_stopping_data/
    srim_nuclear_stopping"));

```

To make this model accessible for α -particles, one has to again add:

```

251 for(G4int atomicNumberIon = 2; atomicNumberIon < 102;
    atomicNumberIon++) {

```

Screened Nuclear Recoil (Modified)

We developed a modification of the standard `G4ScreenedNuclearRecoil` class, which we called `G4ScreenedNuclearRecoilMod`, after seeing that the standard version does not provide meaningful results. What has been a single quantity called *RecoilCutoff*, responsible for defining the energy per nucleon, below which no new secondary recoils are created and below which each particle is stopped within the current step, is now split into two, which are called *RecoilCutoff* and *StoppingCutoff*, respectively.

```

236      G4ScreenedNuclearRecoilMod(const G4String&
      processName = "ScreenedElastic", const G4String &
      ScreeningKey="zbl", G4bool GenerateRecoils=0, G4double
      RecoilCutoff=500.0*eV, G4double StoppingCutoff=25.0*
      eV, G4double PhysicsCutoff=10.0*eV); //RecoilCutoff:
      100.0*eV (default)

```

At every position in the code, where the energy per nucleon, below which the particle is stopped, is retrieved, the *StoppingCutoff* is now inserted.

```

433      if (energy < lowEnergyLimit || energy < stoppingCutoff*
      eV*a1) {

```

```

497      if(incidentEnergy < GetStoppingCutoff()*eV*a1) {

```

```

762      if(incidentEnergy-eRecoil < master->GetStoppingCutoff()
      *eV*a1) {

```

Only at the position, where the creation of secondary tracks due to nuclear recoils is handled, the *RecoilCutoff* is still the measure. In the code snippet below, a further phenomenological adaptation is shown, which makes this cutoff linearly dependent on the energy and the mass of the incident particle.

```

772      if(master->GetEnableRecoils() && eRecoil >
773          (master->GetRecoilCutoff() +
774           incidentEnergy*a1*5.2e-5) * kin.a2 ) {

```

Appendix C.

Brief Analysis of Coherent Photon Scattering in CaWO_4

The topic of this chapter is not strictly related to the work of the thesis. However, it deals with a possible solution to an issue that came up during the time that I worked on it. The respective issue are some events detected in the CRESST experiment, which are found at very low energies, i.e. mainly below 100 eV but reaching up to $\mathcal{O}(\text{keV})$, in the phonon detector. These so called excess events have a physical pulse shape, so that they are not ruled out by the several cuts applied to the data. However, their origin is unclear, therefore worsening the exclusion limits that can be extracted for corresponding low-mass dark matter. The distribution of the excess events seems to be flat down to ~ 100 eV (low statistics) and then rises exponentially to lower energies.

As a possible source for the observed low-energetic recoils, coherent photon scattering was considered due to the publication referenced in [48]. The therefore expected background is said to follow the same distribution as described above, rising exponentially towards low energies. However, the anticipated energies, at which this background becomes relevant, is stated to lie even lower than the excess events observed at CRESST, namely at eV and sub-eV scales. Still, a simulation of this process for our CaWO_4 crystals is of interest in order to test the claims of the reference paper, where calculations were done for targets of Ge, Si and He.

Three mechanisms contribute to the coherent scattering of photons. These are Rayleigh, nuclear Thomson and Delbrück scattering. Rayleigh scattering is the dominating one of these processes, mainly leading to the low-energetic component of coherent scattering. Nuclear Thomson and Delbrück scattering, on the other hand, lead to a non-vanishing cross section for backscattering of the initial photon, which therefore adds to the high energetic portion of the coherent scattering spectrum. Specifically, the recoil energy E_r of an atom with mass M hit by a photon can be written as [48],

$$E_r = \frac{q}{2M} = \frac{(2p_\gamma \sin \frac{1}{2}\theta)^2}{2M} \quad , \quad (\text{C.1})$$

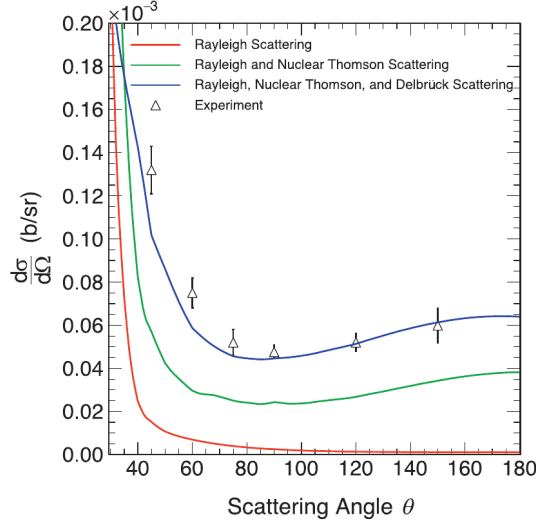


Figure C.1.: Differential cross section of γ -particles with an energy of 2.754 MeV elastically scattered off a U target. The focus is set on the contribution of Delbrück and nuclear Thomson scattering to the total cross section, especially at high scattering angles. Figure taken from Ref. [49].

where q denotes the small transferred momentum, which is proportional to the sine of the scattering angle $0 \leq \theta \leq \pi$. Fig. C.1 shows the differential cross section of elastically scattered photons using a uranium target. A distinction between the values expected solely due to Rayleigh scattering (red line), due to adding nuclear Thomson scattering (green line) and due to the full model, also taking into account Delbrück scattering (blue line), is depicted in the plot. This comparison shows the increased cross section for higher scattering angles introduced through the addition of the two latter processes.

When trying to simulate the coherent scattering of photons with Geant4, however, we face some problems. Only one of the contributing processes is implemented in the simulation code, namely Rayleigh scattering. In addition, atomic recoils are neglected, meaning that the small energy depositions due to coherent photon scattering are not taken into account. In the search for a solution to the first issue, we came across a paper dealing with the implementation of Delbrück and nuclear Thomson scattering in Geant4 [49]. However, their code had not yet been implemented in the Geant4 distribution and direct contact to the authors could not be established. Fig. C.1 is taken from their publication, showing the good agreement of their model to experimental data, especially at high scattering angles. However, as we could not get access to their code, we decided on doing a small exemplary simulation without the implementation of the Delbrück and nuclear Thomson scattering. The second issue could rather easily be resolved by implementing the energy depo-

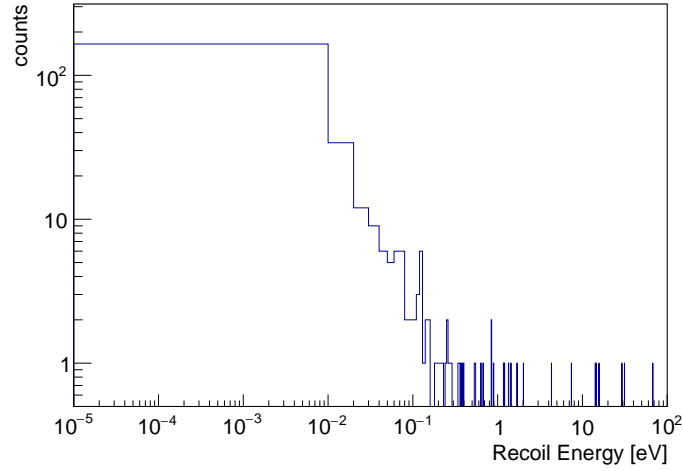


Figure C.2.: Histogram of events, in which solely elastic scattering occurs, simulating 90,000 initial photons with an energy of 1.46 MeV that were shot towards a CaWO_4 crystal.

Recoil Energy Range [eV]	Elastic Scattering Events
< 0.01	165
0.01 - 0.1	82
0.1 - 1	38
1 - 10	8
> 10	6

Table C.1.: Coherent photon scattering events obtained from a simulation of 90,000 initial photons with an energy of 1.46 MeV shot towards a CaWO_4 crystal (cf. Fig. C.2).

sition due to Rayleigh scattering in the existing class `G4LivermoreRayleighModel` due to Eq. (C.1).

In our simulation, we started photons with an energy of 1.46 MeV, i.e. the energy of the γ -line of ^{40}K used for the analysis in Ref. [48]. We simulated 90,000 events and applied a cut, which let us extract those, in which only coherent scattering occurred. This way, we only extract data of events, which in the real experiment might only be seen via a small signal in the phonon detector. The resulting distribution of recoil energies is depicted in Fig. C.2. Only 299 events were scattered solely elastically and are therefore featured in the histogram. The numbers of events in specific energy regions are listed in Tab. C.1, resembling the one given in Ref. [48]. The portion of events in the respective regions is very similar to those listed in the reference

table. Looking at our data, we can conclusively see that recoil events above 100 eV are very unlikely. The maximum recoil energies anyway possible due to an initial photon of 1.46 MeV are calculated via Eq. (C.1) to 17.1 eV for W, 78.4 eV for Ca and 195.9 eV for O. The inclusion of Delbrück and nuclear Thomson scattering would therefore, apart from their low cross section, not be able to significantly change our results in any case. As mentioned above, in the CRESST experiment excess events with energies of $\mathcal{O}(\text{keV})$ are obtained. For these events, a photon of at least 7.5 MeV which is backscattered on an O atom would be necessary. Besides the fact that such a high energetic background is not exceedingly existent and that the cross section for high recoil angles is very low in general, a further issue diminishes the possibility of detecting such energies due to coherent photon scattering. The cross section scales with the mass A and atomic number Z of the target as Z^4/A in the nuclear Thomson scattering regime [48]. Therefore scattering off O is much less prominent than scattering off Ca and especially off W. It may hence be concluded that the excess events, at least above a certain energy, can not be caused by the coherent scattering of photons in the detector.

Bibliography

- [1] F. Zwicky. *On the Masses of Nebulae and of Clusters of Nebulae*. The Astrophysical Journal **86**, 217 (1937).
- [2] V. C. Rubin and J. W. K. Ford. *Rotation of the Andromeda Nebula from a Spectroscopic Survey of Emission Regions*. The Astrophysical Journal **159**, 379 (1970).
- [3] R. Massey et al. *Dark Matter Maps Reveal Cosmic Scaffolding*. Nature **445**, 286 (2007).
- [4] D. Clowe et al. *A Direct Empirical Proof of the Existence of Dark Matter*. The Astrophysical Journal Letters **648**, 109 (2006).
- [5] E. Komatsu et al. *Five-Year Wilkinson Microwave Anisotropy Probe Observations: Cosmological Interpretation*. The Astrophysical Journal Supplement **180**, 330 (2009).
- [6] Planck Collaboration. *Planck 2015 results. XIII. Cosmological parameters*. arXiv:1502.01589 (2015).
- [7] V. Springel et al. *Simulations of the Formation, Evolution and Clustering of Galaxies and Quasars*. Nature **435**, 629 (2005).
- [8] R. Tisserand et al. *Limits on the Macho content of the Galactic Halo from the EROS-2 Survey of the Magellanic Clouds*. Astronomy and Astrophysics **469**, 387 (2007).
- [9] L. Wyrzykowski et al. *The OGLE View of Microlensing towards the Magellanic Clouds. IV. OGLE-III SMC Data and Final Conclusions on MACHOs*. Monthly Notices of the Royal Astronomical Society **416**, 2949 (2011).
- [10] M. Milgrom. *A modification of the Newtonian dynamics as a possible alternative to the hidden mass hypothesis*. The Astrophysical Journal **270**, 365 (1983).
- [11] A. H. G. Peter. *Dark Matter: A Brief Review*. arXiv:1201.3942 [astro-ph.CO] (2012).

- [12] K. Garrett and G. Duda. *Dark Matter: A Primer*. Advances in Astronomy **2011** (2011).
- [13] G. Bertone, D. Hopper and J. Silk. *Particle dark matter: evidence, candidates and constraints*. Physics Reports **405**, 279 (2005).
- [14] G. Bertone. *The moment of truth for WIMP dark matter*. Nature **468**, 7322 (2010).
- [15] L. F. Abbott and P. Sikivie. *A Cosmological Bound on the Invisible Axion*. Physics Letters **120B**, 133 (1983).
- [16] J. Preskill, M. B. Wise and F. Wilczek. *Cosmology of the Invisible Axion*. Physics Letters **120B**, 127 (1983).
- [17] M. Dine and W. Fischler. *The Not So Harmless Axion*. Physics Letters **120B**, 137 (1983).
- [18] S. Scholl. *Neutron Background Simulation for the CRESST – II Experiment*. Ph.D. thesis, Eberhard Karls Universität Tübingen (2011).
- [19] G. Angloher et al. (CRESST Collaboration). *Results on light Dark Matter Particles with a low-threshold CRESST-II detector*. The European Physical Journal C **76**, 25 (2016).
- [20] G. Angloher et al. (CRESST Collaboration). *Results on low mass WIMPs using an upgraded CRESST-II detector*. The European Physical Journal C **74**, 3184 (2014).
- [21] G. Angloher et al. (CRESST Collaboration). *Results from 730 kg days of the CRESST-II Dark Matter Search*. The European Physical Journal C **72**, 1971 (2012).
- [22] K. Schaeffner. *Study of Backgrounds in the CRESST Dark Matter Search*. Ph.D. thesis, Technische Universität München (2013).
- [23] S. Roth. *The Potential of Neganov-Luke Amplified Cryogenic Light Detectors and the Scintillation-Light Quenching Mechanism in CaWO₄ Single Crystals in the Context of the Dark Matter Search Experiment CRESST-II*. Ph.D. thesis, Technische Universität München (2013).
- [24] S. Roth et al. *Microscopic Model for the Scintillation-Light Generation and Light-Quenching in CaWO₄ single crystals*. arXiv:1501.04617 [astro-ph.IM] (2015).

- [25] R. F. Lang et al. *Scintillator Non-Proportionality and Gamma Quenching in CaWO_4* . arXiv:0910.4414 [nucl-ex] (2009).
- [26] R. Strauss et al. *Energy-dependent light quenching in CaWO_4 crystals at mK temperatures*. The European Physical Journal C **74**, 2957 (2014).
- [27] R. Strauss. *Energy-Dependent Quenching Factor Measurements of CaWO_4 Crystals at mK Temperatures and Detector Prototypes for Direct Dark Matter Search with CRESST*. Ph.D. thesis, Technische Universität München (2013).
- [28] R. Strauss et al. *A detector module with highly efficient surface-alpha event rejection operated in CRESST-II Phase 2*. The European Physical Journal C **75**, 352 (2015).
- [29] J. B. Birks. *Scintillations from Organic Crystals: Specific Fluorescence and Relative Response to Different Radiations*. Proceedings of the Physical Society A **64**, 874 (1951).
- [30] J. B. Birks. *The Theory and Practice of Scintillation Counting*. Pergamon (1964).
- [31] C. Patrignani et al. (Particle Data Group). *Passage of Particles through Matter*. Chinese Physics C **40**, 100001 (2016).
- [32] M. J. Berger and S. M. Seltzer. *Stopping Powers and Ranges of Electrons and Positrons*. National Bureau of Standards **82-2550** (1983).
- [33] M. J. Berger and S. M. Seltzer. *Bremsstrahlung Energy Spectra from Electrons with Kinetic Energy 1 keV-10 GeV Incident on Screened Nuclei and Orbital Electrons of Neutral Atoms with $Z = 1-100$* . Atomic Data and Nuclear Data Tables **35**, 345 (1982).
- [34] J. F. Ziegler. *Stopping of Energetic Light Ions in Elemental Matter*. Journal of Applied Physics **85**, 1249 (1999).
- [35] J. Lindhard, M. Scharff and H. E. Schiott. *Range Concepts and Heavy Ion Ranges*. Matematisk-Fysiske Meddelelser Kongelige Danske Videnskabernes Selskab **33**, 14 (1963).
- [36] A. Hössinger. *Simulation of Ion Implantation for ULSI Technology*. Ph.D. thesis, Technische Universität Wien (2000).
- [37] J. F. Ziegler, M. D. Ziegler and J. P. Biersack. *SRIM – The stopping and range of ions in matter*. Nuclear Instruments and Methods in Physics Research Section B **268**, 1818 (2010).

- [38] M. v. Sivers. *Scintillating CaWO_4 Crystals for the Direct Dark Matter Search Experiments CRESST and EURECA*. Ph.D. thesis, Technische Universität München (2014).
- [39] M. v. Sivers et al. *Low-temperature scintillation properties of CaWO_4 crystals for rare-event searches*. Journal of Applied Physics **118**, 164505 (2015).
- [40] M. J. Berger et al. *Stopping-Power and Range Tables for Electrons, Protons, and Helium Ions*, <https://physics.nist.gov/PhysRefData/Star/Text/ESTAR.html>. (2005).
- [41] M. J. Berger et al. *Stopping of Ions heavier than Helium*. Journal of the International Commission on Radiation Units and Measurements **5**, 1 (2005).
- [42] SRIM Web pages for Aquisition of Stopping Power Tables. <http://www.sr-niel.org/index.php/electronic-stopping-power-and-ionizing-dose-calculators-for-protons-ions>, <http://www.sr-niel.org/index.php/protons-ions-nuclear-stopping-power-calculator>. (accessed: 2017-04-27).
- [43] M. H. Mendenhall and R. A. Weller. *An algorithm for computing screened Coulomb scattering in Geant4*. Nuclear Instruments and Methods in Physics Research Section B **227**, 420 (2005).
- [44] S. Agostellini et al. (Geant4 Collaboration). *Geant4 — a simulation toolkit*. Nuclear Instruments and Methods in Physics Research A **506**, 250 (2003).
- [45] J. Agostellini et al. (Geant4 Collaboration). *Geant4 Developments and Applications*. IEEE Transactions on Nuclear Science **53**, 270 (2006).
- [46] R. Brun and F. Rademakers. *ROOT - An object oriented data analysis framework*. Nuclear Instruments and Methods in Physics Research A **389**, 81 (1997).
- [47] I. Antcheva et al. *ROOT - A C++ Framework for Petabyte Data Storage, Statistical Analysis and Visualization*. Computer Physics Communications **180**, 2499 (2009).
- [48] A. E. Robinson. *Coherent photon scattering background in sub-GeV/ c^2 direct dark matter searches*. Physical Review D **95**, 021301 (2017).
- [49] M. Omer and R. Hajima. *Including Delbrück scattering in GEANT4*. Nuclear Instruments and Methods in Physics Research B **405**, 43-49 (2017).